POLITECNICO
MILANO 1863

SCUOLA DI INGEGNERIA INDUSTRIALE
E DELL'INFORMAZIONE

Torque Ripple Minimization in Switched Reluctance Motors for Electric Vehicles: Analysis and MATLAB simulation

TESI DI LAUREA MAGISTRALE IN
ELECTRICAL ENGINEERING
INGEGNERIA ELETTRICA

Author: **Stefano Ciardiello**

Student ID: 10635714
Advisor: Giovanni Maria Foglia
Academic Year: 2024-25

Abstract

The automotive sector is experiencing a revolution towards electrification to reduce dependence on fossil fuels. In this context, the switched reluctance motor (SRM) emerges as a promising alternative to permanent magnet synchronous motors (PMSMs) due to its robustness, construction simplicity and absence of rare earth elements. However, the widespread adoption of SRMs in electric traction is limited by their high torque ripple, intrinsically caused by double structure saliency and phase switching.

This thesis aims to analyse and minimize torque ripple in a 6/4 SRM designed for EV applications. The study presents a comprehensive MATLAB/Simulink simulation comparing a baseline model, utilizing an Asymmetric Half-Bridge (ASHB) converter, with a proposed model featuring advanced control strategies. The proposed solution implements a Flying Capacitor Multilevel Inverter (FCMI) combined with a 5-level hysteresis control logic and a specific current profile modulation including phase superposition.

Simulation results demonstrate a substantial reduction in torque ripple, decreasing from 124.8% in the baseline model to 30.26% in the proposed model, while maintaining thermal stability. The work confirms the effectiveness of the proposed architecture in enhancing SRM performance for electric mobility.

Keywords: Electric Vehicles, Switched Reluctance Motor (SRM), Torque Ripple Minimization, Flying Capacitor Inverter, MATLAB Simulink.

Abstract in italiano

Il settore automobilistico sta vivendo una rivoluzione verso l'elettrificazione per ridurre la dipendenza dai combustibili fossili. In questo contesto, il motore a riluttanza commutata (SRM) emerge come una promettente alternativa ai motori sincroni a magneti permanenti (PMSM) grazie alla sua robustezza, semplicità costruttiva e assenza di terre rare. Tuttavia, l'adozione diffusa degli SRM nella trazione elettrica è limitata dal loro elevato ripple di coppia, causato intrinsecamente dalla doppia salienza della struttura e dalla commutazione di fase.

Questa tesi si propone di analizzare e mitigare il problema del ripple di coppia in un SRM 6/4 destinato ad applicazioni per veicoli elettrici (EV). Il lavoro presenta una simulazione in ambiente MATLAB/Simulink, confrontando un modello base, equipaggiato con un convertitore a ponte asimmetrico (ASHB), con un modello proposto che introduce strategie di controllo avanzate. La soluzione proposta impiega un inverter multilivello a condensatori volanti (Flying Capacitor Multilevel Inverter - FCMI) abbinato a un controllo a isteresi a 5 livelli e a una specifica modulazione del profilo di corrente con sovrapposizione delle fasi.

I risultati della simulazione dimostrano una significativa riduzione del ripple di coppia, che scende dal 124,8% del modello base al 30,26% nel modello proposto, mantenendo al contempo una gestione termica adeguata. Lo studio conferma l'efficacia dell'architettura proposta nel migliorare le prestazioni dell'SRM per l'uso in veicoli elettrici.

Parole chiave: Veicoli Elettrici, Motore a Riluttanza Commutata (SRM), Minimizzazione Ripple di Coppia, Inverter a Condensatori Volanti, MATLAB Simulink.

Contents

1 INTRODUCTION

The transition towards sustainable transportation has placed electric motors at the center of automotive research [1]. As government plans accelerate the phase-out of internal combustion engine (ICE) vehicles, the demand for efficient, cost-effective, and reliable electric propulsion systems is growing rapidly. While Permanent Magnet Synchronous Motors (PMSMs) currently dominate the market, their reliance on rare-earth materials poses economic and geopolitical challenges due to supply chain risks and fluctuating costs.

In this landscape, the Switched Reluctance Motor (SRM) offers a robust solution to these issues. Constructed from simple ferromagnetic materials without permanent magnets, SRMs are inexpensive to manufacture, mechanically rugged, and capable of operating in difficult environments. Despite these significant advantages, SRMs historically suffer from high torque ripple and acoustic noise, which are critical drawbacks for passenger vehicle comfort and drivetrain durability. These problems arise from the doubly salient structure of the motor and the discrete nature of torque production during phase switching.

The primary objective of this thesis is to address the torque ripple limitation in SRMs to make them more suitable for Electric Vehicle (EV) applications. The research focuses on the analysis and simulation of a 6/4 SRM drive system. By moving beyond conventional control methods, this work proposes and validates a novel drive topology using a Flying Capacitor Multilevel Inverter (FCMI) combined with a proper current profiling technique and a five-level hysteresis control logic simulated in MATLAB Simulink.

The thesis is organized to provide a comprehensive analysis of the technology and the proposed solution. It begins with an overview of the current automotive landscape and the shift towards electrification, followed by a categorization of the different types of Electric Vehicles, including BEVs, HEVs, PHEVs, and FCVs. The discussion then moves to a detailed analysis of the Switched Reluctance Motor, examining its mathematical model, structural characteristics, and the specific challenges related to torque generation. Subsequently, the work reviews power converter topologies suitable for SRM drives, introducing the Flying Capacitor Multilevel Inverter as the chosen solution for this study. The core of the thesis presents the MATLAB simulation results, offering a direct comparison between the performance of a standard SRM drive

and the proposed model, highlighting the improvements achieved in torque ripple reduction. Finally, the study concludes with a summary of the findings and suggestions for future developments in the field.

2 ELECTRIC VEHICLES

In a word that takes care of the environment has arisen more sustainable alternative regarding means of transport. Electric Vehicles are receiving significant attention also due to their zero or low emissions.

Those vehicles use electricity instead of fossil fuel, like diesel and petrol, or instead of gas. In the EV electric motor plays a significant role to convert electrical energy into mechanical energy to move the vehicle. In this chapter are presented four different types of EV, the battery electric vehicle (BEV), the plug-in hybrid electric vehicle (PHEV), the hybrid electric vehicle (HEV) and the fuel cell electric vehicle (FCEV), as shown in the Figure 1.

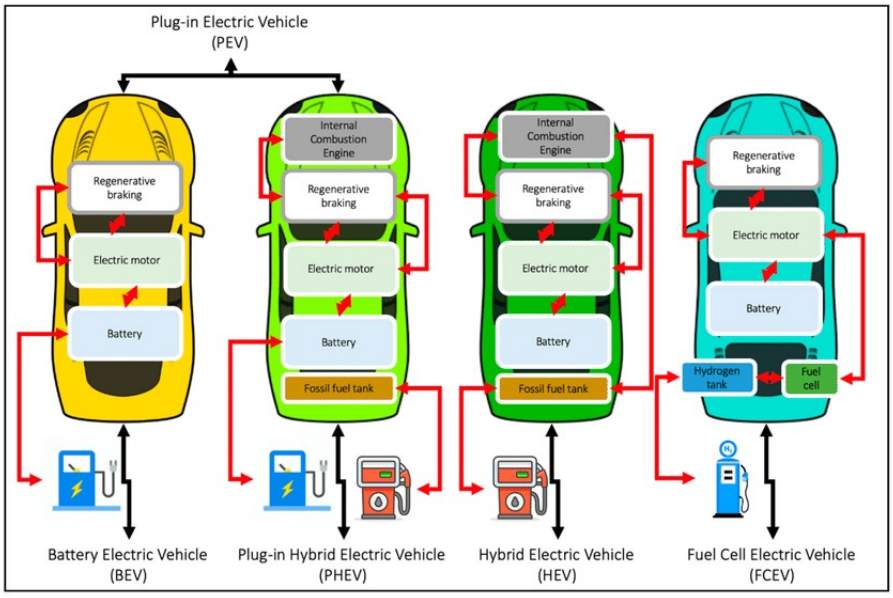

Figure 1 - Types of Electric Vehicles [2]

2.1. Battery Electric Vehicles (BEVs)

Battery electric vehicles (BEVs) are zero-emission vehicles because they do not have an internal combustion engine or fuel tank, so all the electricity they need to move is stored in a battery pack that is integrated into the vehicle [3]. These vehicles depend on an external source of power, after which they convert the chemical energy in their battery packs to electrical energy that is used to drive vehicle functions. The motor can be directly connected to the wheels, or it can be connected via a transmission system that is useful for varying the torque and speed of the vehicle. The battery pack has many cells arranged in a variety of series and parallel configurations to help it achieve the required voltage and capacity.

In addition, the battery pack includes a battery management system whose purpose is to track the temperature, charge, and health of cells so that the charging and discharging processes are optimal. The vehicles are charged by plugging them into external power outlets, with the time and cost of charging depending on the price of electricity, output of the charger, and battery size.

2.2. Hybrid Electric Vehicles (HEVs)

Hybrid vehicles that can recharge their batteries by connecting to the electric grid offer significant environmental and economic benefits. They help reduce the reliance on imported petroleum and decrease greenhouse gas emissions associated with transportation, even when the electricity used for charging is produced from fossil fuels such as coal.

Hybrid electric vehicles (HEVs) combine an internal combustion engine with an electric motor and a battery pack. The interaction between these power sources depends on the specific hybrid configuration, which generally are divided in two main categories, first is parallel and second, the series hybrids.

In a parallel hybrid, both the internal combustion engine and the electric motor can independently or jointly drive the vehicle. The gasoline engine receives fuel from a conventional tank, while the electric motor is powered by energy stored in the batteries. During normal operation, the vehicle's kinetic energy is recovered through regenerative braking, which recharges the batteries. Although certain customized parallel hybrids can be charged externally through the grid, this study assumes that the batteries of all parallel hybrids are recharged exclusively during driving.

On the other hand, series hybrids operate differently. In this configuration, the gasoline engine does not directly power the wheels; instead, it functions as a generator that produces electricity to recharge the battery. The electric motor alone drives the transmission and propels the vehicle. When the battery charge drops below a certain level, the internal combustion engine automatically activates to maintain sufficient energy for operation. However, the primary charging source for series hybrids is the electric grid, which provides a more cost-effective energy supply compared to gasoline.

This dual-power architecture allows hybrid vehicles to combine the efficiency and lower emissions of electric propulsion with the flexibility and extended range provided by conventional fuel.

Series hybrid propulsion system

A typical series hybrid propulsion system configuration is shown Figure 2. Essentially, a series hybrid vehicle can be viewed as an electric vehicle equipped with an onboard power source that recharges its batteries. Typically, an internal combustion engine is mechanically coupled to a generator, which supplies the electrical power required for battery charging. The system can also be designed so that the generator contributes directly to propulsion by acting as a load-leveling device, thereby supporting the traction motor during high-power demand. In such a configuration, the overall battery capacity can be reduced, although this necessitates an increase in the size and power rating of both the engine and the generator.

The power electronic components of a conventional series hybrid system generally include:

1- A converter that rectifies the generator's alternating current (AC) output into direct current (DC) for battery charging.
2- An inverter that converts DC from the batteries back into AC to drive the propulsion motor.

Additionally, a DC–DC converter is used to maintain the charge of the vehicle's low-voltage (12 V) auxiliary battery. Other subsystems, like the electric air-conditioning unit, require dedicated inverters and corresponding control electronics to ensure efficient operation.

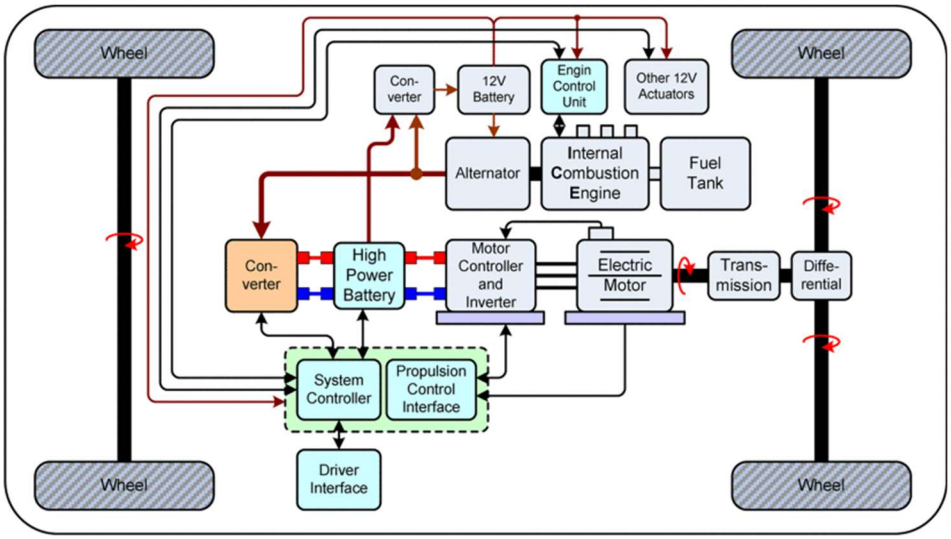

Figure 2 - Series hybrid propulsion configuration [4]

Parallel hybrid propulsion system

Parallel hybrid electric vehicles (HEVs) represent a cost-efficient approach to vehicle electrification, as they enable the continued use of existing manufacturing infrastructure for internal combustion engines, batteries, and electric motors. This compatibility with established production technologies contributes to their economic viability and facilitates large-scale adoption. Nevertheless, the integration of dual power sources necessitates a complex control architecture to effectively manage power flow, torque distribution, and energy recovery during various driving conditions.

Several design configurations of parallel hybrid systems have been developed, each characterized by the specific functions and interactions between the internal combustion engine and the electric motor/generator. In these systems, propulsion can be achieved through either the electric motor or the engine operating independently, or through their combined operation to maximize performance and efficiency.

Commercial implementations of parallel hybrid technology include well-known models such as the Toyota Prius and the Honda Insight [5], which have demonstrated the effectiveness of this configuration in enhancing fuel economy and reducing emissions. A representative schematic of a parallel hybrid propulsion system is presented in Figure 3, illustrating the fundamental arrangement of its primary components and energy flow paths.

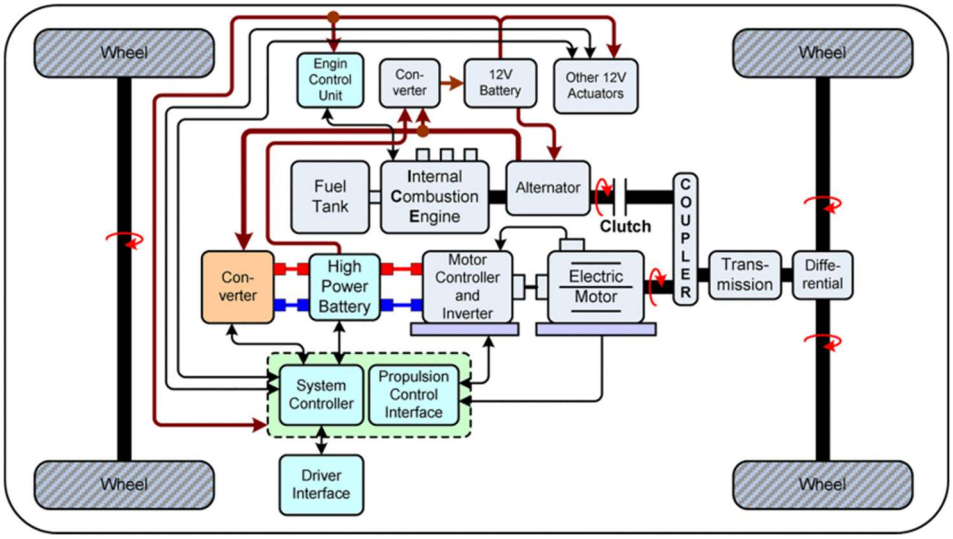

Figure 3 - Parallel hybrid propulsion configuration [4]

2.3. Plug-In Hybrid Electric Vehicles (PHEVs)

Plug-in Hybrid Electric Vehicles (PHEVs) constitute a significant advancement in the progression of hybrid architectures toward full vehicle electrification. Unlike standard hybrid electric vehicles (HEVs), PHEVs feature batteries that can be externally recharged through connection to the electrical grid, enabling a substantially extended all-electric driving range. However, this technological advancement introduces infrastructural challenges, as recharging requires changes in consumer habits and modifications to the existing power distribution network. A key factor to support the costumers acceptance is provide an adequate public charging infrastructure, in commercial location or better in the own garage, supported by the overnight recharge, that has an important impact in both, economical and grid aspects, due to the fact that in the night the cost energy is lower, and also the grid has minor load.

From both an industrial and academic perspective, PHEVs are widely recognized as a significant milestone in the pursuit of energy-efficient and low-emission transportation. Numerous governmental and regulatory agencies have also promoted PHEV development due to their potential to reduce fuel consumption and greenhouse gas emissions. These vehicles employ high–energy-density battery systems that can be externally charged, allowing them to operate exclusively in electric mode for distances greater than those achievable by conventional HEVs.

A schematic representation of a plug-in parallel hybrid propulsion system is presented in Figure 4. Several automotive manufacturers are currently pursuing HEV-to-PHEV conversion strategies as a transitional approach to improve energy efficiency and extend the electric driving range. This conversion may involve either integrating an additional high-energy battery pack or replacing the existing HEV battery system with one of greater capacity. In both configurations, the battery must be capable of storing energy obtained from external charging sources as well as regenerative braking, while also supplying sufficient power to the traction motor under varying load conditions.

To facilitate AC grid charging, a dedicated battery charging system is required, typically consisting of an AC–DC converter with power factor correction (PFC) and a programmable digital controller to manage voltage–current profiles during the charging process. Additionally, a bidirectional DC–DC converter is employed to enable efficient bidirectional energy flow between the traction motor and the high-energy battery pack during both charging and discharging operations.

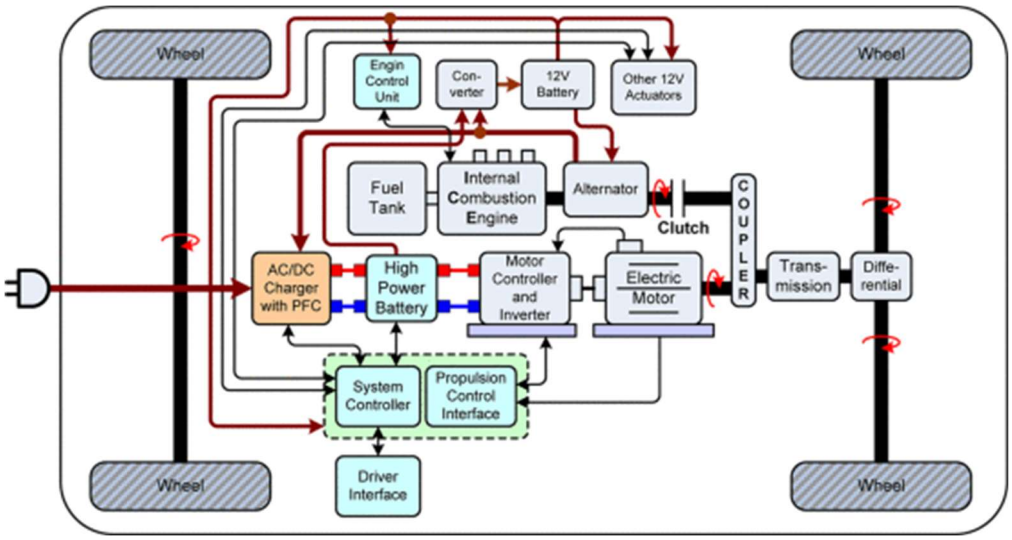

Figure 4 - Plug-in hybrid electric vehicle propulsion (parallel configuration) [4]

2.4. Fuel Cell Vehicles (FCVs)

With the continuous advancement of fuel cell technology, there has been growing interest in their use for vehicle propulsion, onboard power generation, and stationary energy systems. Compared to traditional internal combustion engine (ICE) vehicles, fuel cell vehicles (FCVs) offer several advantages.

First, they convert fuel directly into electricity without combustion, resulting in higher efficiency. They also have no moving mechanical parts, operate quietly, and can use different types of fuels. Moreover, fuel cell systems consume less energy, generate minimal air pollutants. Another notable benefit is that their efficiency remains stable across different system sizes and operating loads. In addition, FCVs can reduce CO_2 emissions by up to 75% and significantly decrease the release of other harmful substances.

To be suitable for automotive applications, a fuel cell propulsion system must meet design and performance standards comparable to current ICE-powered vehicles. These include similar levels of weight, volume, power density, and transient response. Furthermore, the system must provide high short-term performance, rapid acceleration, and good fuel economy, while maintaining easy access and safety in terms of fuel handling, ensuring cost-effectiveness and system longevity.

A typical configuration of a fuel cell vehicle is illustrated in Figure 5. In this system, the fuel cell stack generates a DC output voltage that must be adapted to match the battery voltage through a power conditioner, typically implemented as a DC–DC converter (step-up or step-down, depending on the voltage difference). The conditioned voltage is then supplied to an inverter, which converts it into AC with variable voltage and frequency to drive the propulsion motor. A battery or ultracapacitor is also integrated into the system to supply additional power during acceleration and to assist during startup operations.

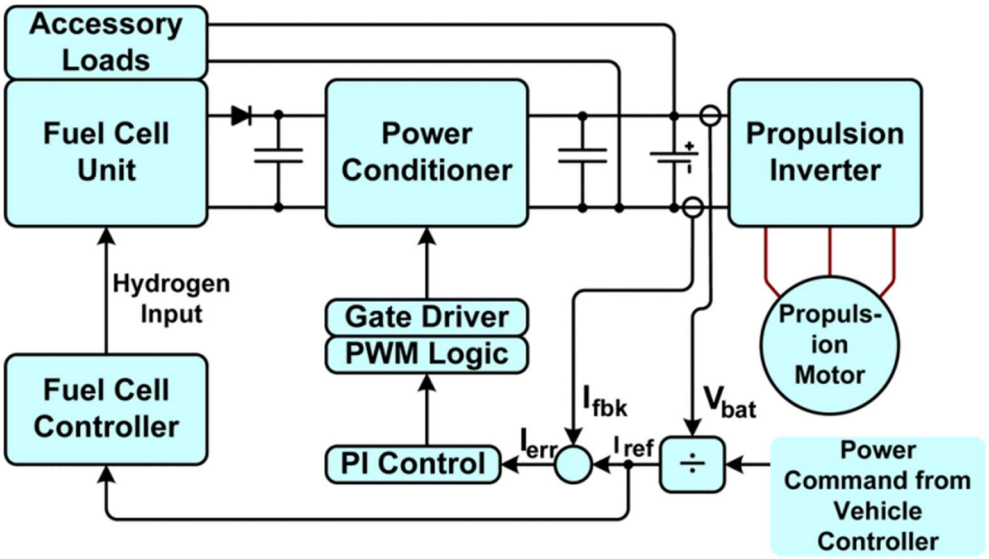

Figure 5 - Typical fuel-cell vehicle system [4]

3 SWITCHED RELUCTANCE MOTOR

It emerges from the analysis of the key performance parameters that switched reluctance motors represent one of the most attractive solutions for electric vehicle applications. A comparative evaluation of different motor technologies, as reported in Table 1, highlights how each solution presents specific advantages and limitations. Induction motors have historically been widely adopted in electric vehicles due to their robustness, reliability, and relatively low maintenance requirements. However, induction motor drives suffer from inherent drawbacks such as increased losses, reduced efficiency and power factor, and a lower inverter utilization factor, which limit their overall performance in traction applications [6].

Permanent magnet synchronous motors (PMSMs) have emerged as strong competitors to induction motors in electric vehicle propulsion systems. Their main advantages include higher efficiency, reduced thermal losses, and superior power density. Despite these benefits, PMSMs face significant challenges related to the use of permanent magnets. These machines are vulnerable to demagnetization effects caused by armature reaction and high operating temperatures, which are common in automotive environments. In addition, the reliance on rare earth materials leads to high costs, long term aging issues, and reduced stability. The limited availability of rare earth elements, combined with the environmental impact associated with their extraction and processing, further constrains the large-scale adoption of PMSMs in electric vehicles. Since the production of rare earth metals is highly concentrated geographically, with China being the dominant supplier, their price and availability are subject to geopolitical and supply chain risks.

In this context, switched reluctance motors (SRMs) offer a promising alternative for future electric and hybrid electric vehicle applications. SRMs are based on simple and widely available materials such as copper and steel, eliminating the dependency on permanent magnets and ensuring a more secure and sustainable supply chain. Their simple construction, inherent robustness, and high fault tolerance make them particularly suitable for safety critical and high reliability applications. Furthermore, SRMs exhibit an excellent torque speed characteristic, enabling constant power operation over a wide speed range, which is a desirable feature for traction drives. Their high torque per ampere capability and fast dynamic response, combined with simple and robust power electronic converters, make them well suited for high speed and temperature sensitive operating conditions.

Despite these advantages, the doubly salient structure of the switched reluctance motor introduces significant challenges that currently limit its widespread adoption in electric vehicles. The electromagnetic torque produced by an SRM depends on both the phase current and the relative angular position between the stator and rotor poles. As a result, phase commutation leads to a pulsating torque profile due to the overlapping contribution of incoming and outgoing phases. Torque ripple is therefore a major concern in SRM drives, particularly in traction applications where smooth torque production is essential. Excessive torque ripple can excite mechanical resonances in the drivetrain, inducing vibrations in the

shaft and gearbox. These vibrations contribute to increased acoustic noise, gear chatter, reduced component lifetime, and overall degradation of system efficiency.

Several approaches have been proposed to mitigate torque ripple and radial force variations through machine design optimization. These include modifications of pole geometry, adjustment of reference current profiles, optimization of turn-on and turn-off angles, air gap design, winding arrangement, and core geometry. While such techniques can reduce torque ripple and vibration, they often lead to an increase in the effective air gap, resulting in a reduction of peak torque and a limitation of the operating range. Moreover, these design-based solutions typically require highly accurate rotor position estimation to achieve satisfactory performance.

For these reasons, the development of advanced control strategies plays a crucial role in enhancing the performance of switched reluctance motors for electric vehicle applications. By adopting suitable control techniques aimed at minimizing torque ripple, it is possible to increase the effective torque per ampere and improve dynamic response. Control methods such as average torque control, direct torque control, current profiling, torque sharing functions, current chopping control, and emerging machine learning based approaches represent active areas of research and offer significant potential for extending the applicability of SRMs in modern electric vehicle propulsion systems.

Table 1 - Comparison of motors for EV application [7]

Parameters	**Brushed DC motor**	**Induction motor**	**PMBLC motor**	**PMSM**	**SRM**
Commutation	Brushed	Not applicable	Electronic	Electronic	Electronic
Torque speed characteristics	Moderately flat	Non-linear	Flat	Flat	Most desirable for EV
Output power to torque ratio	Low	Medium	High	High	High
Efficiency	Low	Medium	Medium	High	Very High
Speed range	Low	Medium	Medium	High	High
Control	Simple and low cost	Simple and low cost	Complex and expensive	Complex and expensive	Simple and low cost
Overall cost	Low	Low	High	High	Low
Maintenance	High	Occasionally required	Low	Low	Low
Noise	High	Medium	Low	Low	High
Overall cost	Low	Low	High	High	Low

Maintenance	High	Occasionally required	Low	Low	Low
Noise	High	Medium	Low	Low	High
Torque ripple	Low	Low	Low	Low	High
Dynamic response	Low	Medium	Medium	High	High
Life	Low	High	Moderate	High	Very High
Fault tolerance ability	Low	Medium	Low	High	Very High

3.1. Math analysis

Consider the machine shown schematically in Figure 6.

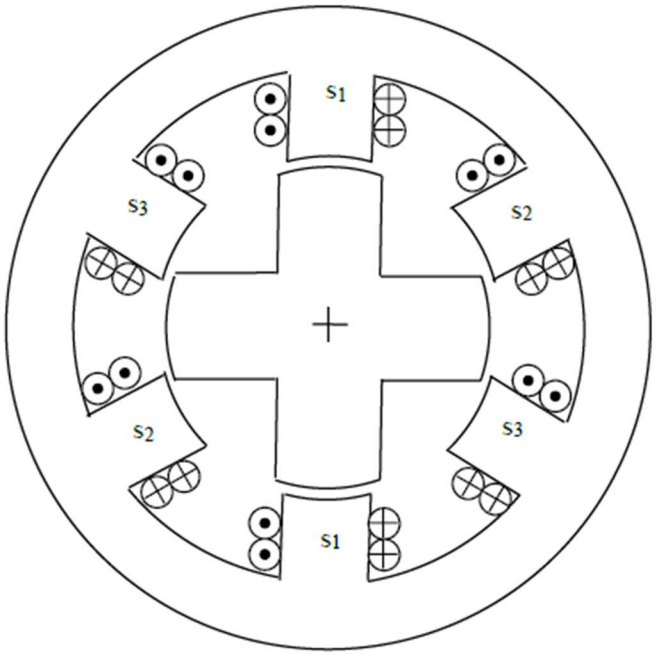

Figure 6 - Schematic representation of an SRM 6-4 [8]

It is a machine with 6 stator poles and 4 rotor ones. In Figure 7 some typical quantities are shown:

- β_s stator pole angle
- β_r rotor pole angle
- θ_m mechanical angle
- r_m average radius at the air gap

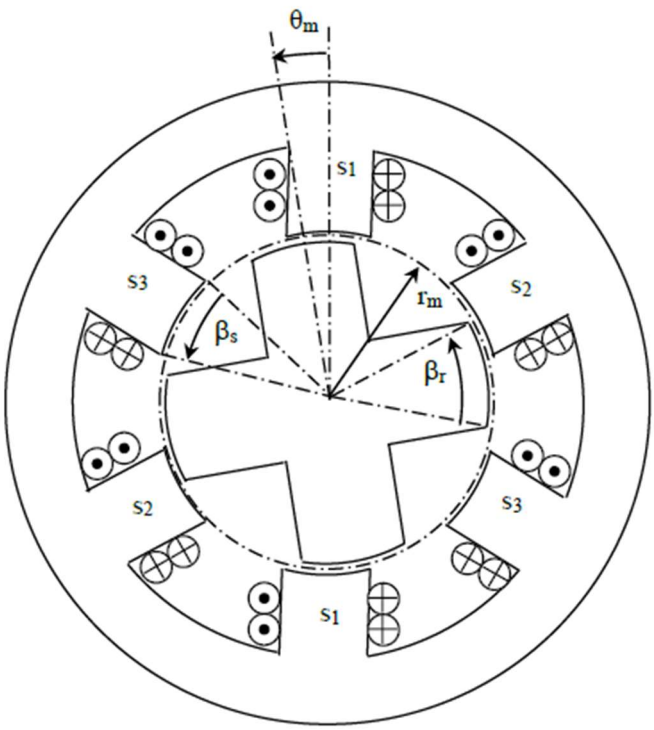

Figure 7 - SRM's typical quantities [8]

Suppose to linearize the machine and consider that all distances are obtained from the product of the angle corresponding to the average radius (and thus all the distances may be represented as angles except for a scaling factor equal to r_m) the Figure 8is obtained.

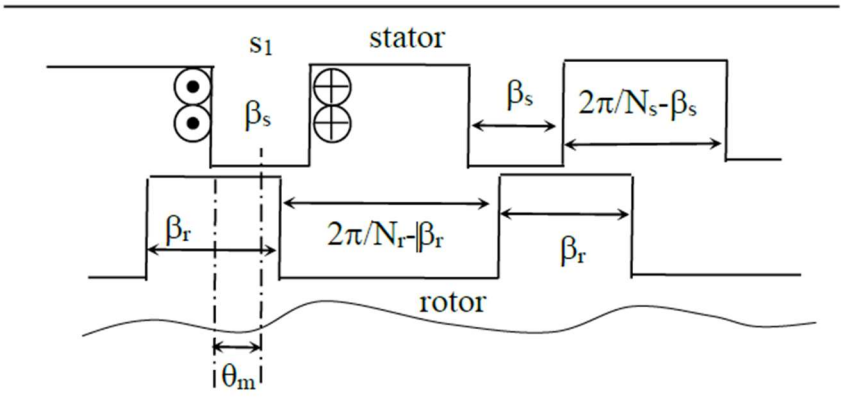

Figure 8 - Linear extension of the machine air gap [8]

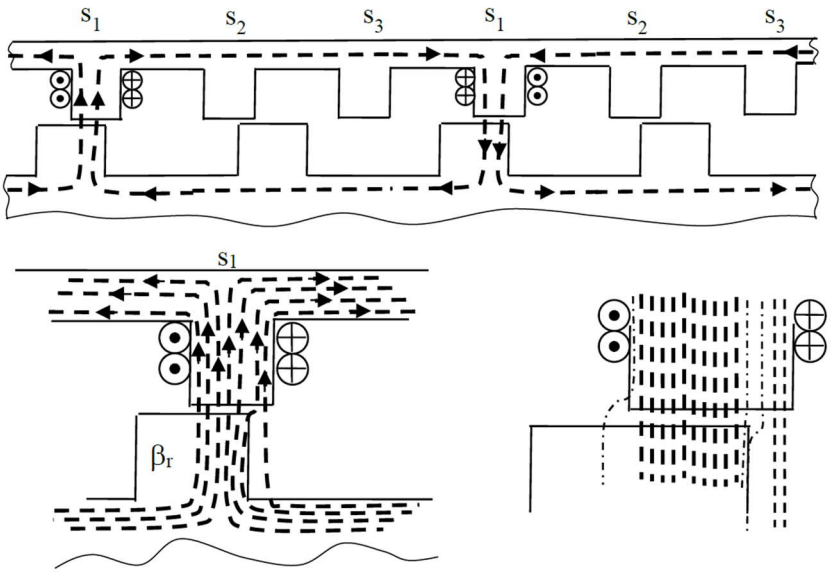

Figure 9 - Field lines trajectories [8]

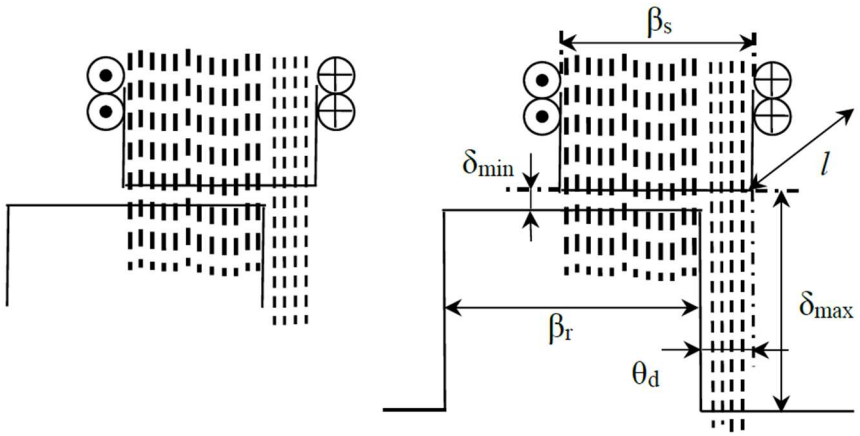

Figure 10 - Field lines trajectories, neglecting fringe effects [8]

The qualitative trajectories of the flux lines are shown in Figure 9. Suppose to neglect the fringe effects: the flux density associated to the lines that pass through the low air gap (δ_{min}) has high value (B_{max}), vice versa for the lines through a large air gap (δ_{max} and B_{min}) (Figure 10). It is possible to consider that the total magnetic flux has two contributes. This is true also for the self-inductance, which is given by the product of the total permeance by the number of turns squared. The total permeance is the sum of two different permeances (they are in parallel): Λ_{max}(for δ_{min}) and Λ_{min}(forδ_{max}) (l is the length of the poles).

$$\Lambda_{max} = \mu_0 \frac{A_{min}}{\delta_{min}} = \mu_0 \frac{(\beta_s - \theta_d) \cdot l}{\delta_{min}}$$

$$\Lambda_{min} = \mu_0 \frac{A_{max}}{\delta_{max}} = \mu_0 \frac{\theta_d \cdot l}{\delta_{max}}$$

$$\Lambda_{tot} = \Lambda_{max} + \Lambda_{min} = \mu_0 \frac{(\beta_s - \theta_d) \cdot l}{\delta_{min}} + \mu_0 \frac{\theta_d \cdot l}{\delta_{max}} = \mu_0 \cdot l \cdot \left[\frac{\beta_s}{\delta_{min}} - \theta_d \cdot \left(\frac{1}{\delta_{min}} - \frac{1}{\delta_{max}}\right)\right]$$

$$L_s = N_s^2 \Lambda_{tot}$$

$$L_{s\,max} = N_s^2 \left(\mu_0 \frac{\beta_s \cdot l}{\delta_{min}}\right) \quad \text{when } \theta_d = 0$$

$$L_{s\,min} = N_s^2 \left(\mu_0 \frac{\beta_s \cdot l}{\delta_{max}}\right) \quad \text{when } \theta_d = \beta_s$$

(3.1. 1)

The displacement angle θ_d is linearly dependent on θ_m; therefore, the self-inductance L_s is a linear function of the mechanical angle θ_m, starting from L_s max to $L_{s\,min}$.

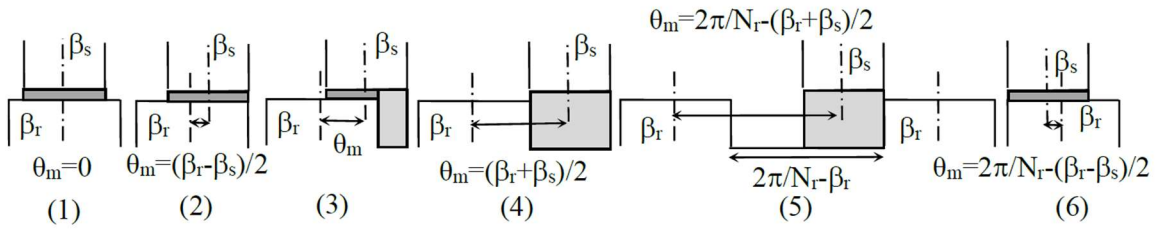

Figure 11 - Variation of the cross-section of the magnetic flux (in the case of $\beta_s < \beta_r$

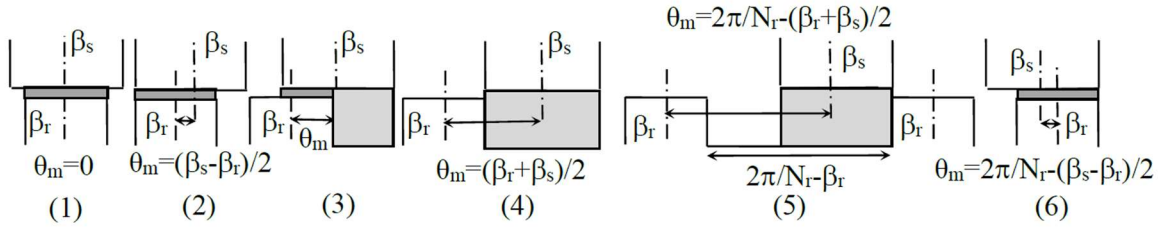

Figure 12 - Variation of the cross-section of the magnetic flux (in the case of $\beta_s > \beta_r$) [8]

Consider the case of $\beta_s < \beta_r$ (usually, more common due to $N_s > N_r$).

Having neglected the fringe effects, the cross-section of the flux between the position (1) and the position (2) remains constant. This means that the magnetic flux supported by the current i_{s1} remains constant. Also, the flux linked with the winding s1 will be constant. The self-inductance, defined as the ratio between the flux linked with the winding and the current in it, will therefore be constant and equal to$L_{s\,max}$. This period will be then (valid for both $\beta_s < \beta_r$ and $\beta_r < \beta_s$): $|\beta_s - \beta_r|/2$.

For angles greater than $|\beta_s - \beta_r|/2$ the cross-section of the magnetic flux through the low air gap decreases linearly with the angle itself while the cross-section of the magnetic flux, that passes through the high air gap, grows linearly (3). This linear variation affects both the magnetic flux, the flux linkage and the self-inductance. This behavior lasts till configuration (4) where the stator pole abandons the rotor pole. The distance is β_s in the first case ($\beta_s < \beta_r$), while in the second case is toβ_r: in general, we can say that the length is the minimum of β_s and β_r [min (β_s,β_r)].

From the configuration (4) and as long as the stator pole is inside the space between two rotor poles ($2\pi/N_r - \beta_r$) (5), the magnetic flux must pass through a high air gap, but the cross-section remains constant. During this period $(2\pi/N_r - \beta_r) - \beta_s = 2\pi/N_r - \beta_r - \beta_s$), the inductance is constant and equal to its minimum value $L_{s\,min}$.

Between the configuration (5) and (6) there is partial overlap between the stator pole and the rotor one (in a specular way to what occurred between the configuration (2) and (4)), so the inductance increases linearly; the distance is still$\min(\beta_s, \beta_r)$.

From the configuration (6) and till the end of the period $2\pi/N_r$ (which corresponds to the configuration (1)), the inductance is constant and equal to its maximum value; the distance is $|\beta_s - \beta_r|/2$.

The winding inductance profile is a function of the mechanical angle as shown in Figure 13.

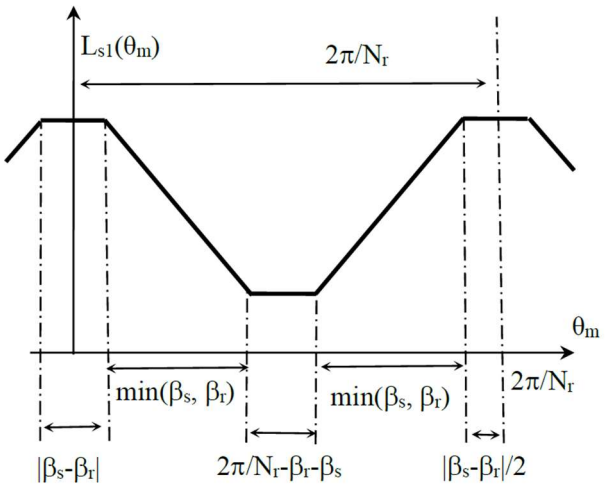

Figure 13 – Self-inductance profile as a function of the mechanical angle [8]

As regards the other windings, the corresponding self-inductance will have a similar trend but phase-shifted by an angle equal to the period of the self-inductance ($2\pi/N_r$) divided by the number of windings (or phases q). The displacement angle is, therefore, $\varepsilon = 2\pi/(N_r \cdot q)$. In this case, q is equal to 3 and $N_r = 4$, then the period ($2\pi/(N_r)$) corresponds to 90° while the phase shift ε is 30°.

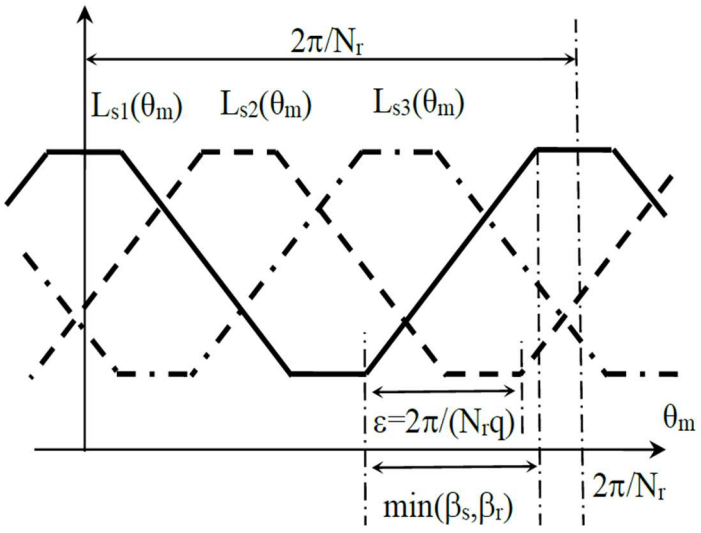

Figure 14 - Self-inductances profiles as a function of the mechanical angle [8]

Consider to supply only one winding at once. Relative to phase s1, the relationship voltage/current and flux/current will be:

$$v_{s1} = R_s i_{s1} + \frac{d\psi_{s1}}{dt}$$
$$\psi_{s1} = L_{s1}(\theta_m) i_{s1}$$

(3.1. 2)

The energy balance gives:

$$v_{s1} i_{s1} = R_s i_{s1}^2 + i_{s1} \frac{d\psi_{s1}}{dt} = R_s i_{s1}^2 + i_{s1} L_{s1}(\theta_m) \frac{di_{s1}}{dt} + i_{s1}^2 \frac{dL_{s1}(\theta_m)}{dt} =$$
$$\dots = R_s i_{s1}^2 + i_{s1} L_{s1}(\theta_m) \frac{di_{s1}}{dt} + i_{s1}^2 \frac{dL_{s1}(\theta_m)}{d\theta_m} \frac{d\theta_m}{dt}$$

(3.1. 3)

To understand how the input power is divided into the different contributions (Joule losses, derivative of the internal magnetic energy of the system and mechanical power) it is better to consider the derivative of the energy stored in an inductor (where the inductance is a function of the mechanical angle):

$$U = \frac{1}{2} L_{s1}(\theta_m) i_{s1}^2$$
$$\frac{dU}{dt} = \frac{1}{2} L_{s1}(\theta_m) 2 i_{s1} \frac{di_{s1}}{dt} + \frac{1}{2} i_{s1}^2 \frac{dL_{s1}(\theta_m)}{dt} = L_{s1}(\theta_m) i_{s1} \frac{di_{s1}}{dt} + \frac{1}{2} i_{s1}^2 \frac{dL_{s1}(\theta_m)}{d\theta_m} \frac{d\theta_m}{dt}$$

(3.1. 4)

This means that in the energy balance equation, the first term ($R_s i_{s1}^2$) is related to the Joule losses, while the second one and a half of the third one represents the change of internal magnetic energy. One half of the third term, then, represents the mechanical power.

$$P = \frac{1}{2} i_{s1}^2 \frac{dL_{s1}(\theta_m)}{d\theta_m} \frac{d\theta_m}{dt}$$

(3.1. 5)

Called n_p the number of pole pairs for each phase, the mechanical speed in the mechanical world is:

$$\Omega_m = \frac{1}{n_p} \frac{d\theta_m}{dt}$$

(3.1. 6)

So, the torque value is:

$$T_e = \frac{P_m}{\Omega_m} = \frac{n_p}{2} i_{s1}^2 \frac{dL_{s1}(\theta_m)}{d\theta_m}$$

(3.1. 7)

It is clear that the torque is zero if there is no variation of the self-inductance and that the sign of the torque does not depend on the sign of the current but on the sign of the derivative of the self-inductance. This means that in the sector in which the inductance decreases, the machine is working as a generator and as a motor when it increases. If during the period ($\min(\beta_s, \beta_r)$), in which the derivative of the inductance is constant (this derivative is then indicated by k_c), the phase current is maintained constant (with a value equal to I_c) through appropriate power converter, the torque T_e remains constant and equal to:

$$T_e = \frac{n_p}{2} I_c^2 k_c$$

(3.1. 8)

In order to maintain constant the torque, throughout the period ($2\pi/N_r$), it is necessary that, before the end of the constant slope period of the phase inductance, a new phase in which the inductance begins to have a constant slope has to be ready. Since the phase shift between two phases is equal to ($\varepsilon = 2\pi/(N\_r \cdot q)$, for a constant torque it must be $\varepsilon \leq \min(\beta_s, \beta_r)$.

3.2. Applied structural analysis

The Switched Reluctance Motor (SRM) is a type of doubly salient electric machine that generates motion through reluctance torque rather than conventional electromagnetic torque, as its name suggests. The term "switched" refers to the fact that the operation of this motor depends on the sequential activation of power switching devices, such as transistors [1].

One of the main advantages of the SRM lies in its structural simplicity. All the windings (and, if required, any permanent magnets) are mounted exclusively on the stator, while the rotor is composed solely of laminated ferromagnetic material without windings or magnets. The stator windings are typically distributed, and from a manufacturing standpoint, the SRM is relatively simple and cost-effective to produce. The coils can be easily inserted into the stator slots, and the laminated core can be obtained through standard stamping processes. Additionally, since the windings, one of the main sources of heat during operation, are located on the stator, cooling is more efficient and straightforward.

Despite these advantages, SRMs also present several drawbacks, the most notable being high torque ripple and acoustic noise, both inherent consequences of the machine's geometric configuration. These issues have become major research topics in the field of electric drives.

As illustrated in Figure 15, traditional SRMs can have various stator-to-rotor pole ratios depending on the design. The motor's electromagnetic torque arises from the tendency of magnetic flux to follow the path of least reluctance. When a rotor pole becomes aligned with a stator pole, the inductance of the energized phase reaches its maximum value, producing the mechanical torque that drives rotation.

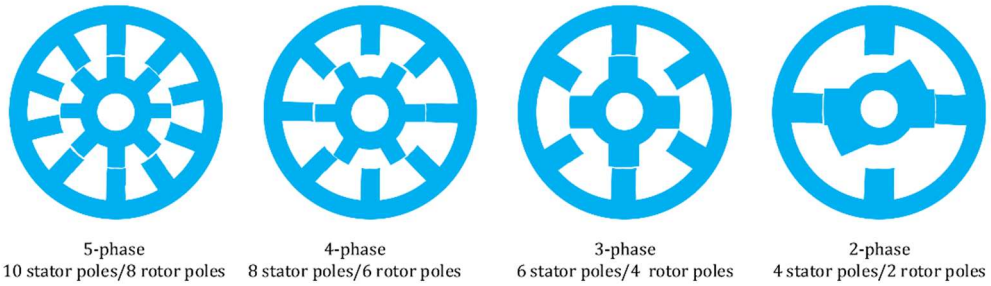

Figure 15 - Conventional SRMs with different numbers of stator and rotor poles [9]

The instantaneous voltage between the terminals of a single phase can be expressed as:

$$U = Ri + \frac{d\emptyset}{dt} \tag{3.2. 1}$$

where U is the instantaneous voltage on each phase, i is the phase current, R is the resistance of a phase, ∅ is the flux linkage, and t is the time. The flux linkage changes with the rotor position and phase current value:

$$U = Ri + \frac{\partial\emptyset}{\partial I} * \frac{di}{dt} + \frac{\partial\emptyset}{\partial\theta} * \frac{d\emptyset}{dt} = Ri + L(\theta, i) * \frac{di}{dt} + E(\theta, i) * \frac{d\theta}{dt} \tag{3.2. 2}$$

where θ is the rotor position, E(θ,i) is the back electromotive force (EMF), and L(θ,i) is the instantaneous inductance. The mechanical equation of the SRM is deduced as Equation (3.2. 3):

$$J * \frac{d\omega}{dt} = T_e - T_L - T_0, \qquad \omega = \frac{d\theta}{dt} \tag{3.2. 3}$$

where J is the rotational inertia, ω is the rotational angular speed, T_e is the electromagnetic torque, T_L is the load torque, T_0 is the additional torque including friction torque, air resistance torque, etc.

In [10] the authors designed and optimized a 12/8 SRM for EVs and hybrid EVs (HEV). Owing to their optimization method, the torque ripple is reduced by 10.2% and the average torque is increased by 2.4% compared to a typical benchmark design. They have concluded that the most effective way to increase the initial torque is by increasing the rotor diameter.

In general, research can be defined as a systematic and detailed investigation carried out to identify solutions or answers to specific problems or questions that motivate the study [1]. In the case of the Switched Reluctance Motor (SRM), most of the existing literature has focused on performance enhancement, either through design optimization or advanced control strategies. Beyond these areas, several additional motivations further emphasize the importance of SRM development, as outlined below.

In recent years, there has been a growing interest in high-speed electric machines, with their operational limits continually expanding. Notably, the record speed of one million revolutions per minute (rpm), represents a significant milestone in the field. Since power is the product of torque and angular speed, and torque is proportional to both the rotor diameter and stack length, several key conclusions can be drawn:

1. For the same output torque and volume, high-speed motors can deliver greater power output, thereby achieving higher power density.

2. For the same power output, high-speed motors can be designed to be smaller and lighter, which is particularly advantageous in automotive and transportation applications, where compactness and reduced weight are highly desirable.
3. For the same power level, the smaller dimensions and optimized winding configurations of high-speed machines can lead to improved efficiency.

High-speed motors are typically implemented in direct-drive systems, which provide several advantages, including higher overall efficiency, due to the elimination of mechanical transmission components such as gears or belts, and increased reliability. Typical applications benefiting from these features include micromachinery, industrial spindles for grinding or drilling, dental surgery tools, air compressors, and vehicle turbochargers or superchargers.

The SRM is particularly suitable for high-speed operation owing to its simple and robust rotor structure, which contains no windings or permanent magnets. As a result, the rotor exhibits very low inertia compared to other motor types, enabling rapid acceleration and stable performance at elevated speeds.

Designing an optimal SRM requires considering several trade-offs among competing design objectives. Various design parameters can be adjusted to meet the desired performance specifications. For instance, within a fixed motor volume, increasing the output torque by enlarging the rotor's outer diameter may lead to a thinner stator yoke, which in turn increases the risk of magnetic saturation. Therefore, a balance must be achieved between torque production and structural magnetic integrity.

The electromagnetic torque T_e generated by an SRM can be expressed as:

$$T_e = \frac{1}{2} i^2 \frac{dL(\theta, i)}{d\theta} \tag{3.2. 4}$$

where i is phase current, θ is rotor position, and $L(\theta, i)$ can be calculated as,

$$L(\theta, i) = \frac{\lambda}{i} \tag{3.2. 5}$$

Here, λ denotes the flux linkage of the phase.
From these equations, it can be observed that the output torque can be influenced by any design modification that affects the flux linkage variation across the air gap.

To achieve higher torque output, various rotor geometries with variable air gaps have been investigated, as illustrated in Figure 16. These rotor designs aim to extend the positive torque region, thereby increasing the average torque. However, such

configurations typically allow rotation in only one direction. Furthermore, saturated rotor and internal air-gap structures exhibit reduced mechanical robustness due to the presence of internal voids or holes. Conversely, stepped rotors provide improved structural integrity but tend to generate higher torque ripple, resulting from the abrupt variations in the air gap.

Similarly, introducing variable air-gap structures on the stator can induce asymmetry in the magnetic field, which may increase the radial forces on the stator teeth, potentially leading to higher vibration and acoustic noise.

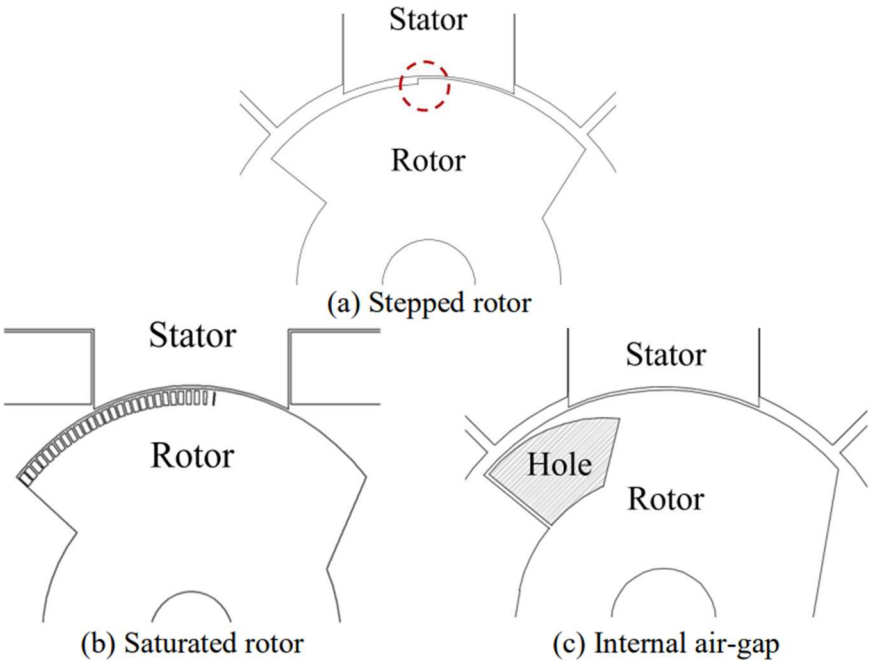

Figure 16 - Variable air-gap rotor structures [1]

Conventional or basic Switched Reluctance Motors (SRMs) employ a long magnetic flux path, in which the flux travels along the entire circumference of the stator back iron. This configuration results in a phenomenon known as flux reversal, where the magnetic flux generated by one excited phase interferes with that of another, as illustrated in Figure 17. The occurrence of flux reversal increases the required magnetomotive force (MMF) and contributes to higher core losses, ultimately leading to reduced electrical utilization and lower efficiency of the motor.

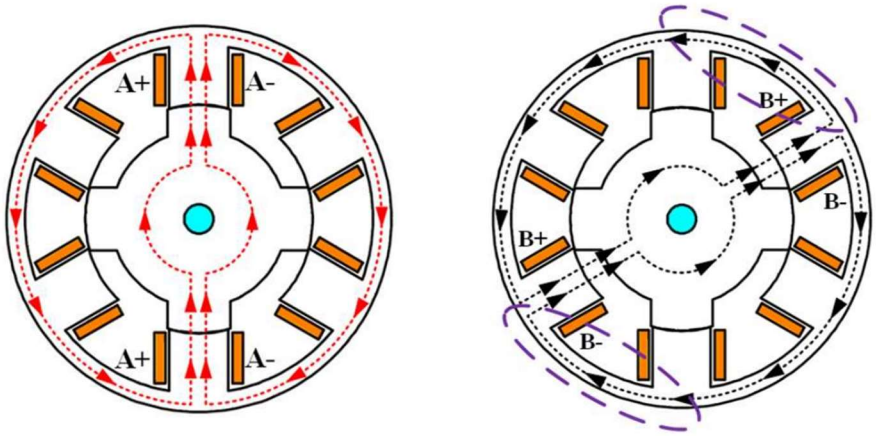

Figure 17 - Flux reversal phenomena [1]

To address these issues, short flux path designs have been proposed as a means of improving performance. These configurations aim to minimize the magnetic path length and, consequently, reduce losses and improve torque production. A class of such designs is known as segmental SRMs, which can be categorized into two main types: stator-segmented (SS) and rotor-segmented (RS) machines.

In stator-segmented SRMs (SS-SRMs), the stator core is divided into discrete segments, typically shaped like the letters C or E, depending on the number of poles. This segmentation shortens the magnetic path and reduces flux reversal. Conversely, rotor-segmented SRMs (RS-SRMs) achieve a short flux path by combining magnetic isolators and ferromagnetic materials in the rotor structure, effectively redirecting the magnetic flux to minimize interference between phases, as shown in Figure 18 for a 6/5 SRM configuration.

When designing stator-segmented SRMs, special attention must be given to the radial forces acting on the rotor, as asymmetries in these forces can lead to rotor imbalance. In extreme cases, this imbalance may cause physical contact between the rotor and stator during operation. On the other hand, rotor-segmented SRMs require careful manufacturing precision, since their construction involves two different materials. These materials must remain securely bonded during operation, particularly under high-speed conditions, where mechanical stresses are significant.

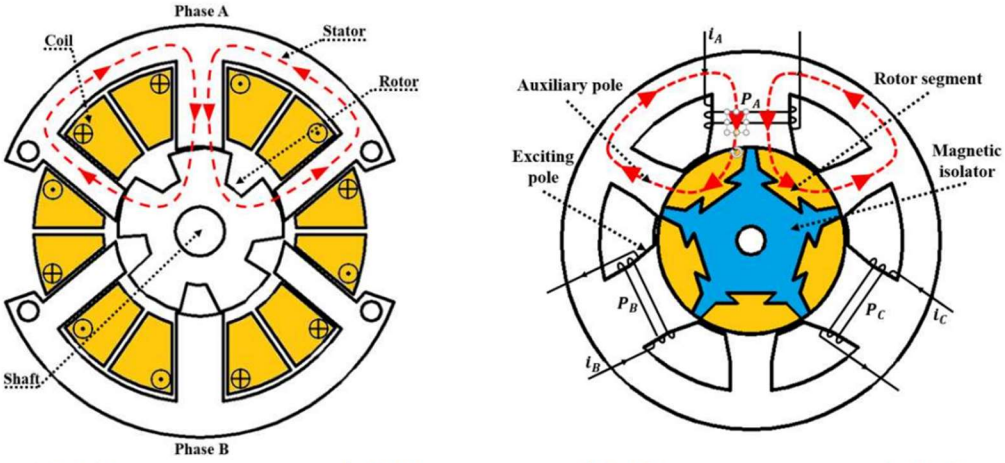

(a) 6/5 stator segmental (SS) (b) 6/5 rotor segmental (RS)

Figure 18 - Segmental SRMs [1]

A comparative study between the segmental Switched Reluctance Motor (segSRM) and the conventional SRM (CSRM) was presented in [11]. The results demonstrated that the segSRM delivers approximately 9% higher rated torque across the entire speed range while also exhibiting lower core and copper losses compared to the CSRM.

An advanced four-phase belt-driven starter generator 16/10 segmented SRM (DSSRM) has been proposed to increase the fault tolerance capability and reduce the torque ripple. A digital control system has been designed and presented for the machine. A DSSRM with the segmental rotor and E-core stators has been proposed for high-torque applications. The proposed DSSRM has shown higher torque than the single-stator SRM at the same current.

3.3. Multi-Stack and Multi-Layer Structure Conventional SRM

In order to have a high-power machine, multi-layer SRMs can be used properly, and different configurations have been introduced for this type of motor so far. Due to similar performance of different layers in the multi-layer SRM, all electromagnetic models introduced for the one-layer SRM can be used basically for the multi-layer SRM. In order to predict the static characteristic of flux linkage with a phase, a mathematical model is developed for the SRM [12].

The structure of the conventional 4-layer 8/6 SRM is depicted in Figure 19.

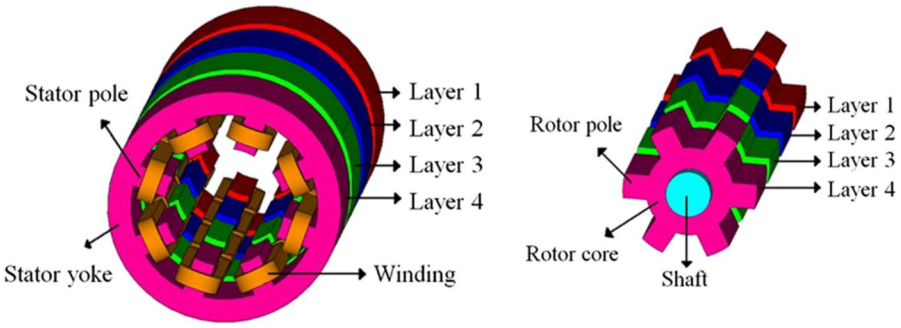

Figure 19 - Structure of the conventional 4 - layer SRM: (left) stator, (right) [12]

A simple and fast analytical model based on the Magnetic Equivalent Circuit (MEC) method was proposed for multi-layer Switched Reluctance Motors (SRMs). This model allows accurate prediction of the phase flux linkage at two critical rotor positions: the unaligned and aligned positions. To validate the approach, the model was applied to a 4-layer 8/6 SRM, and the simulation results were compared with those obtained from an existing fast MEC model, 3D finite element (FEM) analyses, and experimental measurements. The comparison demonstrated that the proposed MEC model achieves high computational efficiency while maintaining good accuracy.

Furthermore, an effective geometric optimization method was introduced to reduce torque ripple in different configurations of multi-layer SRMs. FEM simulations showed that introducing a rotor displacement between adjacent layers (α) can significantly decrease torque ripple while maintaining a constant average torque. The results also indicated that the percentage reduction in torque ripple increases with the number of layers in the SRM. Since the average torque also increases with additional layers, this design approach is particularly suitable for developing high-power SRMs with minimal torque ripple, provided there are no constraints on the motor's axial length.

As result of what said before, here summary Table 2 of how the torque ripple and average torque improve their value depending on the number of the layer and the displacement angle α, shows in the Figure 20.

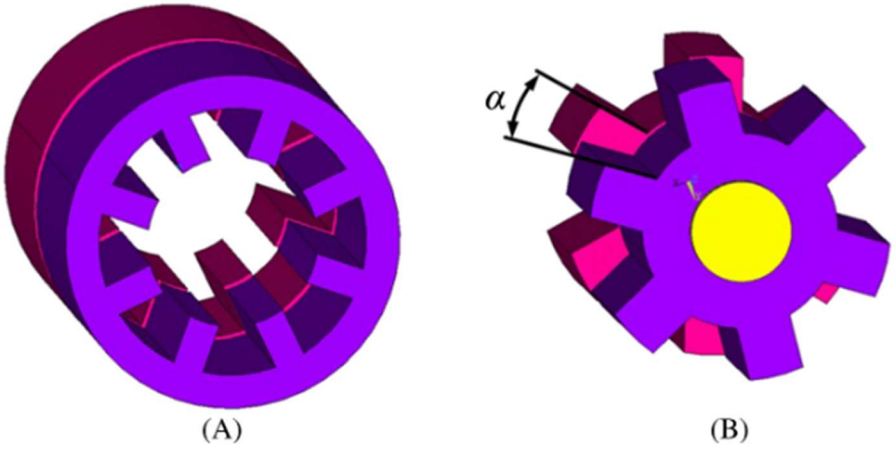

Figure 20 - The structure suggested for the multi-layer SRM: (a) stator, (b) rotor [12]

Table 2 - Average torque and torque ripple of the discussed multi - layer 8/6 SRM for different number of layers [12]

	Torque ripple [%]	**Average torque [Nm]**
Conventional 2 - layer structure	94.9	2.1
Conventional 3 - layer structure	94.9	3.2
Conventional 4 - layer structure	94.9	4.3
Conventional 5 - layer structure	94.9	5.4
Suggested 2 - layer structure, $\alpha = 7.5^{\circ}$	20.6	2.1
Suggested 3 - layer structure, $\alpha = 5^{\circ}$	10.3	3.2
Suggested 4 - layer structure, $\alpha = 3.75^{\circ}$	8.7	4.3
Suggested 5 - layer structure, $\alpha = 3^{\circ}$	4.4	5.4

The design process of electric machines, particularly high-speed motors, involves not only electromagnetic considerations but also mechanical constraints. At higher rotational speeds, mechanical losses increase significantly, especially those caused by bearings. An inappropriate choice of bearing type can severely limit the maximum operating speed of the motor. Conventional bearings such as roller and ball bearings are often unsuitable for high-speed operation due to excessive friction and wear. As a result, non-contact bearing systems, including air foil bearings and magnetic bearings, are commonly employed in such applications.

Motors equipped with magnetic bearings fall under the category of maglev (magnetically levitated) machines, along with bearing-less motors. The bearing-less

switched reluctance motor (BLSRM) operates based on the same principles as magnetic bearings. In this type of machine, two distinct sets of windings are used: torque windings and suspension windings. The torque windings are responsible for producing rotational torque, similar to those in a conventional SRM, while the suspension windings generate the magnetic forces required to levitate and stabilize the rotor and shaft within the air gap, maintaining their balance during operation.

Figure 21 illustrates phase A of a 12/8 BLSRM showing the generation of suspension forces, while Figure 22 presents the corresponding inductance, torque, and force profiles. The rotor positions θ_1 and θ_3 represent the unaligned and aligned positions, respectively. The phase excitation is deactivated before reaching the aligned position ($\theta_2 < \theta_3$), meaning that torque generation only occurs within the angular interval θ_1 to θ_2. Consequently, a torque dead zone exists between θ_2 and θ_3, during which the next phase is excited to continue rotation. Meanwhile, the suspension force gradually increases, reaching its maximum at the aligned position (θ_3), and then decreases smoothly thereafter.

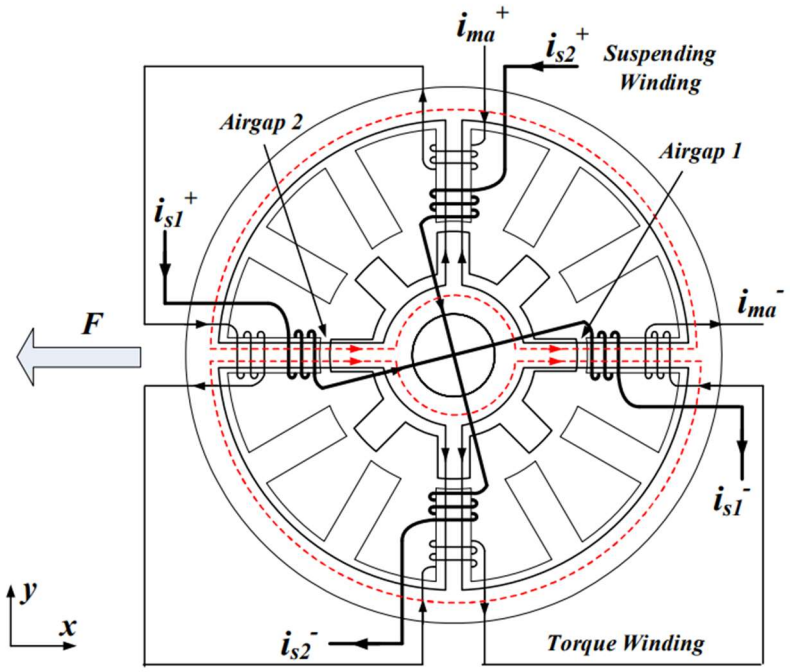

Figure 21 - Typical conventional BLSRM structure [1]

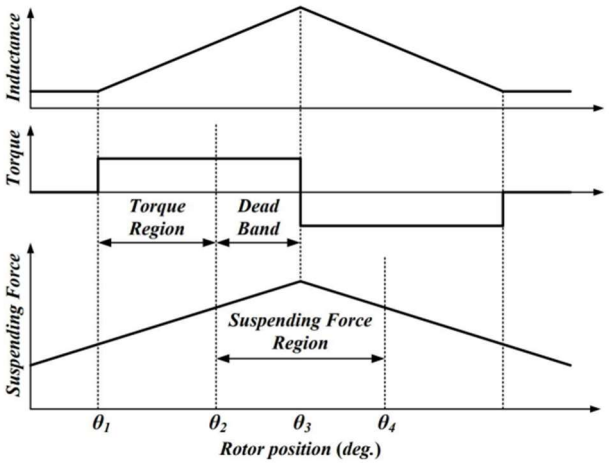

Figure 22 - Ideal inductance, torque and suspending force profiles [1]

3.4. Hybrid SRM

The Switched Reluctance Motor (SRM) is typically known as a permanent-magnet-less machine, which is one of its most appealing features, as previously discussed. However, in certain applications, the inclusion of permanent magnets (PMs) becomes necessary, particularly in single-phase SRMs, where the rotor must be positioned in a definite starting location to ensure self-starting capability.

A single-phase SRM uses the fewest number of switches, making it cost-effective in terms of the converter design. Nevertheless, its conventional configuration suffers from a large torque dead zone, occupying approximately half of the electrical cycle. This results in high torque ripple, and if the rotor stops within this dead zone, the motor is unable to self-start.

To overcome this limitation, permanent magnets are often incorporated into single-phase SRMs. Their main function is to generate a positive cogging torque, effectively pulling the rotor to maintain rotation even when the phase excitation is absent. In other words, the magnets provide a "virtual" excitation effect.

Figure 23 illustrates several 4/4 hybrid SRM configurations. In the V-shaped motor, the magnets are inserted in the middle of the stator in a concentrated arrangement. This design is simple and easy to manufacture, but it weakens the stator mechanically because the core is divided into segments instead of remaining continuous. Conversely, the π-shaped motor maintains the stator's structural integrity while still concentrating the magnetic flux. However, its design and manufacturing process are more complex.

Another configuration, known as the Cyrano motor, also places the magnets within the stator core but does so in a simpler and more robust manner compared to the previous two designs. Nonetheless, this motor introduces a rotor nose feature, which complicates manufacturing and can increase production costs.

An important consideration when designing hybrid SRMs, beyond the placement of the permanent magnets, is the starting torque. Due to the presence of the magnets, these machines typically exhibit a high cogging torque. Therefore, the electromagnetic torque generated by phase excitation must be sufficiently large to overcome the cogging torque and ensure smooth startup and operation.

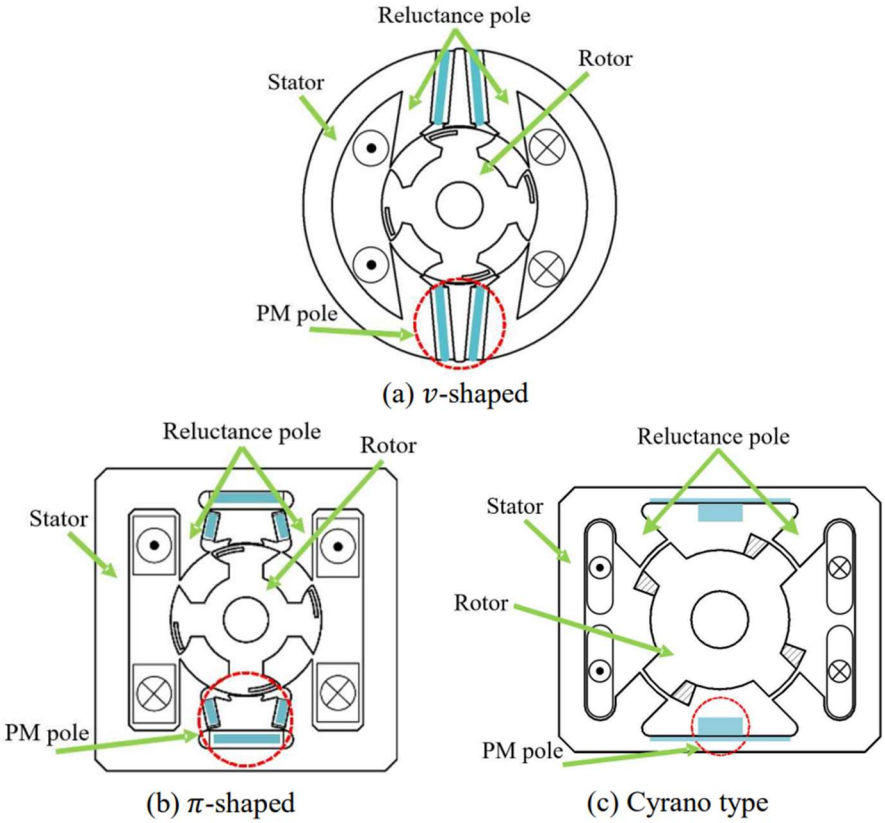

Figure 23 - Hybrid SRM structure variation [1]

3.5. Control

The operation of a Switched Reluctance Motor (SRM) is governed by reluctance torque, unlike synchronous motors that generate a continuous torque. This fundamental characteristic results in a high torque ripple and a strongly nonlinear magnetization behaviour. Torque generation in SRMs depends on the switching sequence synchronized with the rotor position, therefore one of the most common control approaches is switching angle control, where the turn-on and turn-off angles are carefully selected by the designer. In addition, current control strategies, such as soft chopping, hard chopping, and hysteresis control, are widely employed, as summarized in Table 3. Typically, current control is used in low-speed regions, where the current can reach its maximum value and be regulated to achieve the desired performance. Conversely, angle control is more suitable for high-speed operation, where the current does not have sufficient time to rise; in this case, controlling the on/off angles allows a greater current flow. In this section, however, rather than focusing on conventional methods, three advanced SRM control strategies are introduced and briefly discussed.

Table 3 - Common SRM Control Methods

	Current control (low speed)	Angle control (high speed)
Concept	Back EMF < supply voltage Slow inductance increases rate Large current increase rate Chopping → Loss due to switching action	Back EMF > supply voltage Fast inductance increases rate Low current increase rate Excitation angle is moved forward to allow more current
Explanation	Conduction angle decrease → Higher torque ripple and acoustic noise In high-performance machine (low torque ripple), current overlap method is preferred	Conduction angle decrease → Higher torque ripple, reduced average torque Constant conduction angle → reduced torque ripple and lower acoustic noise

Direct torque control

It is well established that Direct Torque Control (DTC) is an advanced control technique originally developed for induction motors, and it is fundamentally based on the principles of vector control. DTC is mainly applied to AC machines that exhibit linear magnetization characteristics; therefore, conventional DTC cannot be directly implemented in Switched Reluctance Motors (SRMs), where each phase operates independently. The core concept of DTC is to select appropriate stator voltage vectors according to the rate of change of torque and flux, as illustrated in Figure 24. In this approach, the amplitude of the stator flux vector is maintained constant, while torque control is achieved by modulating the stator flux—either increasing or decreasing it as required. For SRMs, the DTC structure is adapted to include both torque and stator flux hysteresis controllers, enabling accurate and dynamic regulation of motor performance.

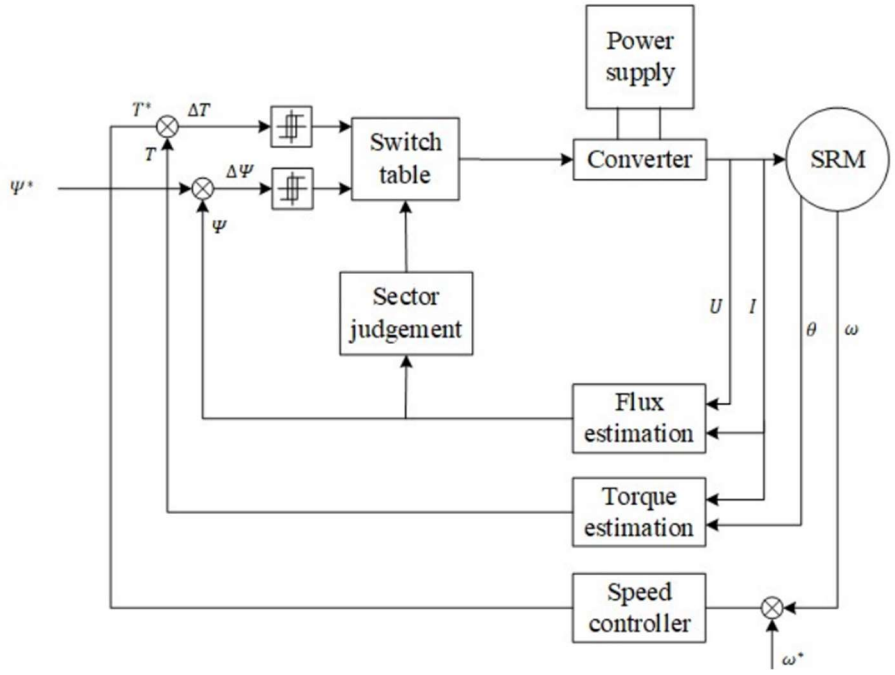

Figure 24 - Block diagram of conventional DTC [1]

For a three-phase SRM with asymmetric half bridge converter, there are six voltage vectors available to be selected as illustrated in Figure 25 - Voltage vector selection for a 3-phase SRM. The selection of voltage vectors complies with the rules in the Table 4 below where T and k indicates the phase torque and active phase.

Table 4 - Voltage Vector Selection

T↑ λ↑	T↑ λ↓	T↓ λ↑	T↓ λ↓
V_{k+1}	V_{k+2}	V_{k-1}	V_{k-2}

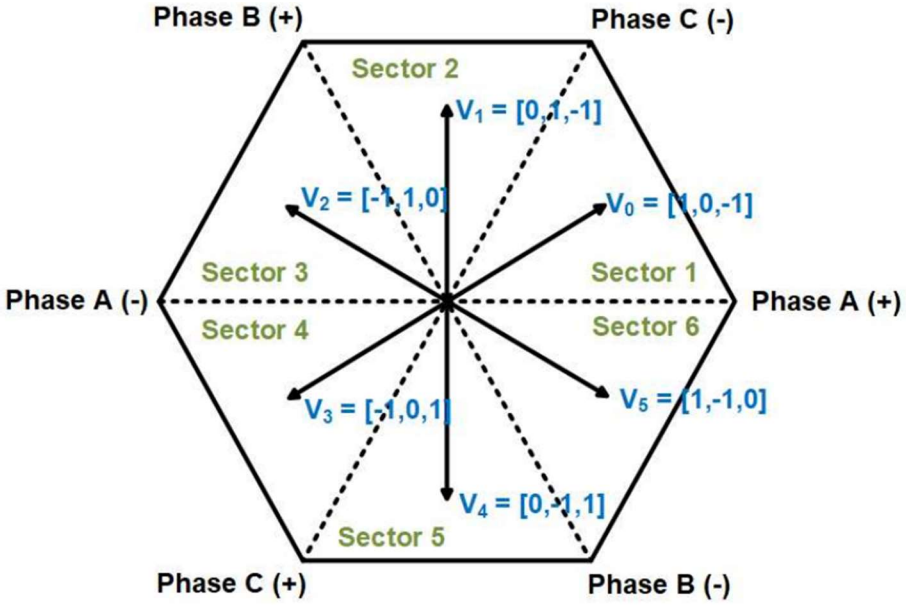

Figure 25 - Voltage vector selection for a 3-phase SRM [1]

The Direct Torque Control (DTC) technique applied to Switched Reluctance Motors (SRMs) offers several notable advantages.

- It provides high-precision torque feedback compared to conventional control methods such as chopping current control, enabling the development of high-performance speed and position controllers.
- Torque is directly regulated, making implementation straightforward through the use of hysteresis controllers without the need for predetermined current profiles. This represents a significant simplification compared to other instantaneous torque control techniques, such as current control-based torque sharing functions or current profiling methods, which require a torque–current transformation.
- Furthermore, no commutation strategy is required, and the same control principle can be applied at any rotor position.

However, DTC in SRMs also presents some drawbacks.

- Since an SRM is generally singly excited, the simultaneous excitation of additional phases may produce negative phase torque, thereby reducing the total output torque. Consequently, maintaining a constant amplitude of the flux vector, as done in induction motors, is not necessary for SRMs.
- Additionally, a high phase current is needed to sustain a constant flux, which leads to increased copper losses and a reduction in efficiency. This condition results from the longer conduction time of each phase. Moreover, the absence

of a current controller may allow the current to exceed the maximum permissible limit, potentially affecting the system's reliability.

Sensor less control

Switched Reluctance Motors (SRMs) rely strongly on accurate rotor position information to ensure proper phase excitation and torque production. Traditionally, mechanical position sensors such as rotary encoders, optical encoders, or Hall-effect sensors are employed to provide this feedback. However, these components increase the overall cost and size of the drive system, while also reducing reliability when operating in harsh or high-vibration environments. To address these limitations, sensorless control techniques have been developed as an alternative. The core principle of sensorless control is to estimate the rotor position by analyzing electrical quantities such as phase current, back-electromotive force (back-EMF), or inductance variation, eliminating the need for physical sensors. Several approaches have been proposed in literature. The instantaneous flux linkage is calculated from real-time measurements of current and voltage and then processed using intelligent algorithms, such as artificial neural networks (ANNs) or adaptive neuro-fuzzy inference systems (ANFIS), to predict the rotor position with high accuracy.

In general, four major categories of sensorless control methods can be identified:

1. Open-loop control,
2. Passive waveform detection,
3. Active probing,
4. State observer-based methods.

In conventional open-loop control, the motor operates based on a predefined dwell angle, synchronized with the commutation frequency rather than direct rotor position feedback. This approach makes SRM behaviour comparable to that of a stepper motor, where the rotor advances by discrete step angles without feedback. To enhance stability in such systems, additional circuits may be employed to monitor the DC-link current, since a sudden increase in this current often indicates a higher load demand. Although open-loop control is cost-effective, it lacks adaptability to dynamic load variations and is typically unsuitable for applications with rapidly changing torque demands. The passive waveform detection method estimates the rotor position by observing variations in the phase current waveform, which are influenced by the back-EMF as the rotor moves between the aligned and unaligned positions. This approach, originally developed for closed-loop operation of stepper motors, infers position based on the relationship between EMF modulation and current behaviour. Another technique, known as active probing, involves applying a small high-frequency voltage

signal (typically rectangular) to an unenergized phase, as illustrated in Figure 26. The resulting current pulses vary depending on the instantaneous inductance of the phase, increasing when the rotor is at an unaligned position (low inductance) and decreasing when approaching alignment (high inductance). By comparing these current responses to a defined threshold, the rotor position can be detected, allowing the control system to precisely trigger phase excitation through rapid switching of the power transistors.

The maximum value of the current pulse is given by equation (4.7. 1):

$$i_{peak} = \frac{VT}{L(\theta)} \tag{4.7. 1}$$

where T is the period of voltage pulse, V is excitation voltage, and $L(\theta)$ is inductance according to rotor position.

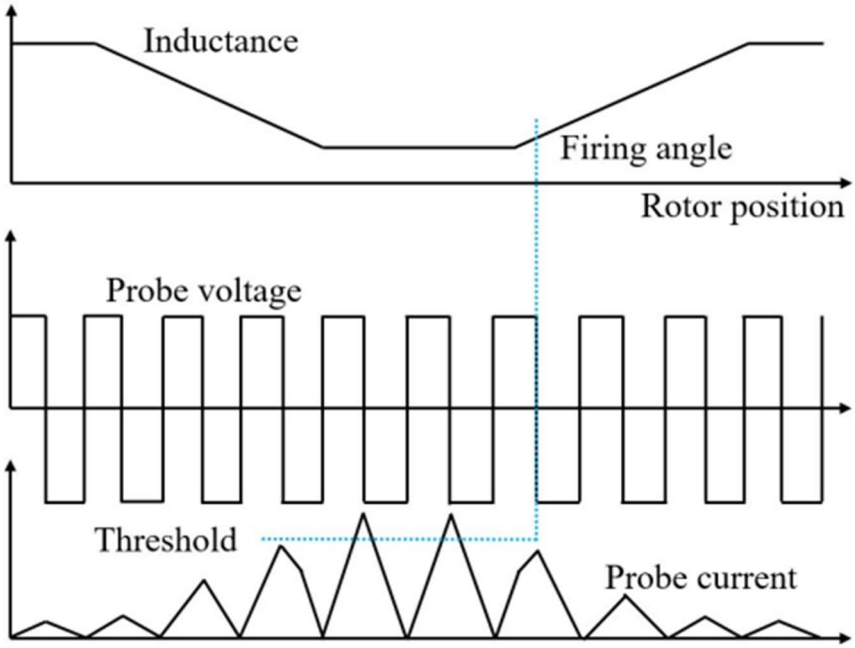

Figure 26 - Active probing method [1]

The method is based on a mathematical model of a motor running in parallel with the actual drive. The measured voltage of the actual drive is connected to the model which calculates state variables such as rotor position and speed. The method gave accurate rotor position with a resolution of 1/15,000 revolution.

3.6. Electric vehicle example

Electric vehicle (EV) has been gaining more interest due to the increasing problems of environmental pollution and energy crisis for the past few years. NEDO projects in Japan have started the development of rare-earthfree motors that have to be competitive in size, power density, and efficiency to the ones with magnets. Literature reported of such development by designing an 18/12 SRM that matches the performance of permanent magnet synchronous machine (PMSM) of the same size. The proposed SRM is targeted for Toyota Prius which is a type of hybrid electric vehicle (HEV) that uses both ICE and electric motor.

The prototype of the motor is shown in Figure 27.

Figure 27 - Prototype SRM for traction [1]

Another example of SRM utilization in EV is electric supercharger which function is to provide a boost of air into ICE for sudden acceleration. Valeo reportedly used a 6/4 SRM with the maximum speed of 70,000 rpm and maximum power of 7 kW for a supercharger in Audi SQ7. The cut-off drawing of the system is shown in Figure 28 as seen in official Audi website.

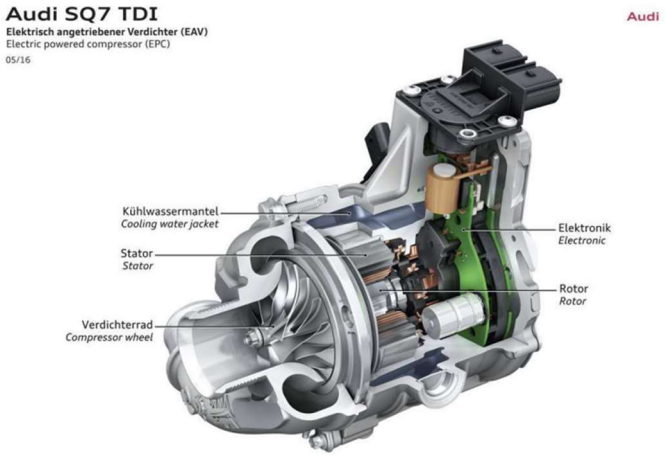

Figure 28 - Electric supercharger system [1]

3.7. Synchronous Reluctance Motor

Figure 29 shows a synchronous reluctance machine with two poles (in Figure 30 a four poles machines is presented). It has a typical anisotropic structure of the rotor.

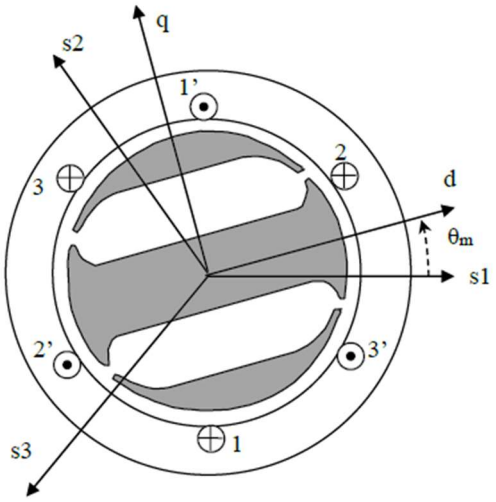

Figure 29 - Synchronous reluctance machine (two poles) $L_d \gg L_q$

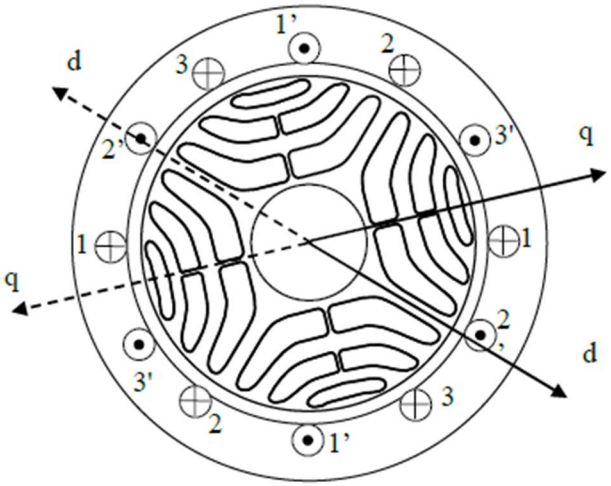

Figure 30 - Example of a synchronous reluctance machine (four poles)

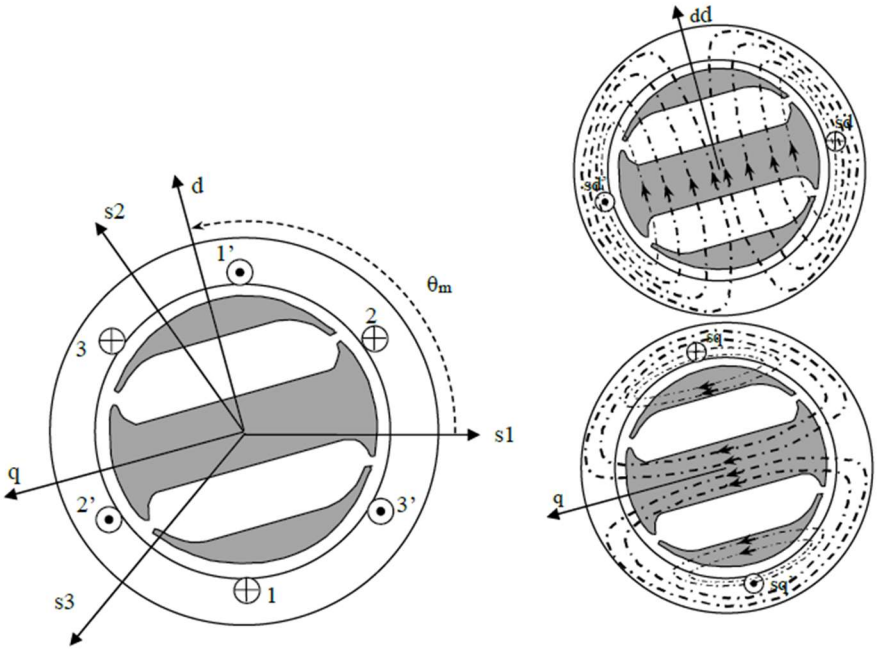

Figure 31 - Synchronous reluctance machine (two poles) with a different choice of the axes

Figure 31 show the situation when L_q>>L_d ,so the flux lines due to the current i_{sd} has to pass through large air gaps.

The stator is equal to the AC brushless stator but the rotor has no permanent magnets and it is designed in order to have a very high difference between the two inductances L_d and L_q ; the higher depends on the choice of the reference frame: in Figure 29 L_d>>$L_q$while in Figure 31 L_q>>L_d. Henceforth the reference as in Figure 29 will be adopted.

The torque is only given by its reluctance term:

$$T_e = n_p|(L_d - L_q)i_{sd}i_{sq}|$$

(3.7. 1)

So, it is necessary to feed the machine with both thei_{sd} and i_{sq} currents.

The electrical equations become:

$$v_{sd} = R_s i_{sd} + L_d p i_{sd} - \dot{\theta}_m L_q i_{sq}$$

$$v_{sq} = R_s i_{sq} + L_q p i_{sq} + \dot{\theta}_m L_d i_{sd}$$

(3.7. 2)

There are different control strategies. One among the other comes from the fact that the time constant of the electric circuit on the "d" axis is higher than on the "q" axis (L_d>>$L_q$implies τ_d>>τ_q).

So, a constant value of i_{sd} (equal to the rated value i_{sdn}) is performed, while $i_{sq}$is used to control the torque. Above the base speed (due to the power converter), it is necessary to decrease i_{sd}.

The control scheme is very similar to the scheme of an AC brushless, shown in Figure 6-19.

Another strategy is the so-called MTPA (Maximum Torque Per Ampere). The idea is related to the choice of i_{sd} and i_{sq}so to have the maximum ratio between the torque and the amplitude of the stator current is ($i_s = \sqrt{i_{sd}^2 - i_{sq}^2}$).

4 CONVERTERS

The heart of an EV is an electric machine; therefore, it should be selected wisely to meet the listed criteria [13]:

- High power and torque density (/kg and /A);
- High torque to inertia ratio;
- High efficiency;
- Compact size and low weight;
- Low cost;
- Robust (electrically and mechanically) and fault tolerant;
- Wide constant torque/speed range;
- Wide temperature operating range;
- Low vibration and acoustic noise.

The SRM cannot be directly connected to any AC or DC power source, but it requires a suitable power converter for its controlled operation. Its main function is to energise and de-energise each phase winding correctly to ensure continuous rotation. Numerous converter types have been proposed for SRM drives, and the chosen type significantly impacts on drive cost, size, and performance. The converter must meet several requirements to enhance SRM drive performance:

1. Fast magnetisation and demagnetisation of SRM phases:

   The converter should facilitate fast magnetisation to quickly reach the reference current in the phase winding, thereby increasing the SRM base speed. It should also minimise demagnetisation time by rapidly extinguishing phase current to eliminate the current tail, preventing the SRM from entering the negative torque production region. These conditions can be enhanced by boosting the DC supply voltage during magnetisation and demagnetisation periods.

2. Phase overlap:

   The converter must be able to simultaneously energise the incoming phase and de-energise the outgoing phase.

3. High efficiency:

To improve SRM drive efficiency, the converter should efficiently return demagnetisation energy to the supply or store it for use in energising another phase rather than dissipating it as heat in winding resistance.

4. Minimum cost:

   An economical converter provides excellent performance with a minimal number of switching devices. Fewer switches reduce switching losses, the number of gate drive circuits, and overall converter cost.

5. Fault tolerance:

   For critical applications, a high-reliability converter is necessary to ensure continuous SRM rotation even after a phase failure.

6. Low complexity:

   Simple design and control algorithms are preferred for the SRM converter.

4.1. Proposed converters for SRM drives

For high-performance EV applications, the following requirements are considered as mandatory requirements to be offered by the SRM converter [14] [15].

1) The converter must offer both magnetization and regenerative demagnetization modes.
2) The SRM converter must offer independent control for each phase to allow current overlapping between the machine phases.

Accordingly, SRM converters that do not offer any of these requirements are not considered. In addition, the following SRM converters are excluded.

1) The converters that achieve commutation through a dissipative medium. This commutation mechanism is dependent on the resistance value; this makes the commutation process uncontrolled with varying speed and torque. In addition, it results in high losses. Therefore, it is impractical for high-performance applications, such as EVs.
2) Soft Switching Converters: These converters can sig significantly reduce the switching losses by utilizing resonant circuits to achieve zero-voltage or zero-current switching However, compared to hard switching converters, the device's voltage stresses should be increased multiple times; this, in turn, results in a significant increase in the VA rating of the converter. Therefore, the energy saving acquired through the adoption of soft switching converters in EVs is small to justify this adoption.

During commutation, the stored energy of the outgoing phase is transferred into an intermediate storage element to be used for energizing another phase. According to the handling way this energy, the SRM converters are classified as follows.

- Converters with magnetic commutation
- Converters With Capacitive Commutation

Figure 32 shows a flowchart of this classification.

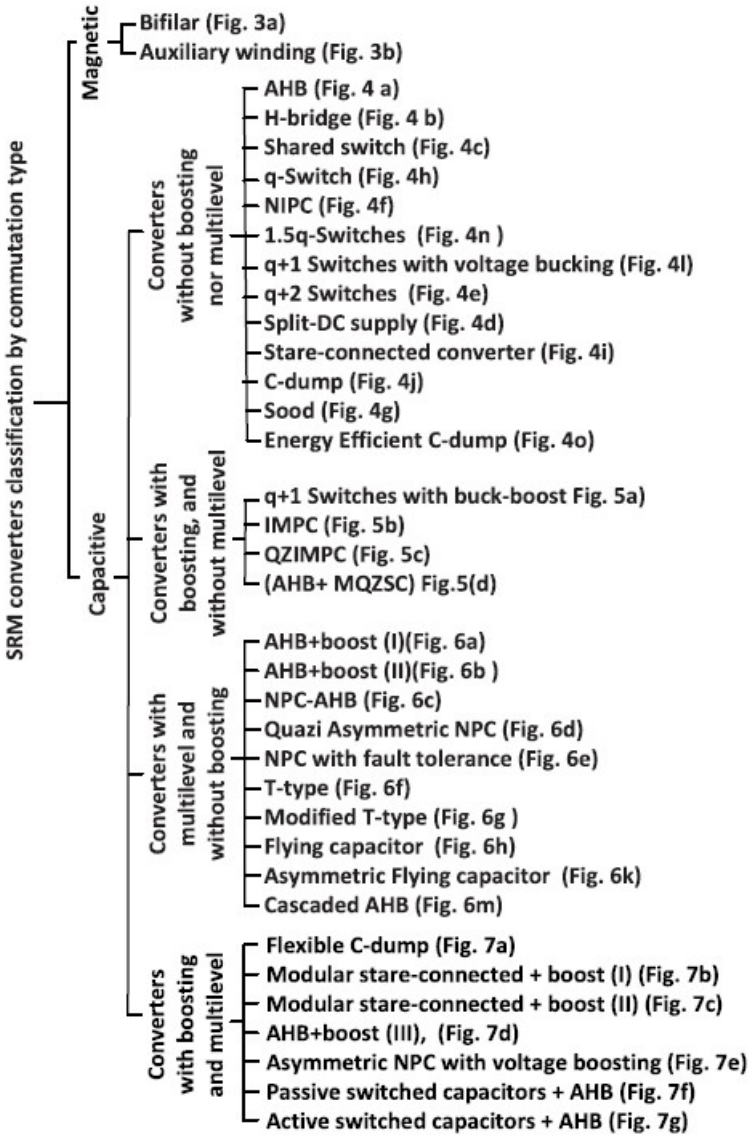

Figure 32 - Classification of SRM converters [15]

Generally, SRM converters are classified based on two criteria. The first criterion is the number of switching devices, while the second criterion depends on the commutation method. However, classifying converters based solely on the number of switching devices does not fully capture the strengths and weaknesses of each converter type.

Therefore, the converters can be classified including four subgroups: bridge, dissipative, magnetic, and capacitive (hard-switching category).

4.1.1. Bridge Converters

The bridge converter is the most common type of converter used in SRM drives [16]. It includes variants like asymmetric half bridge (ASHB), common phase, and common switch converters, as follows.

Asymmetric Half Bridge

The ASHB is the most prevalent SRM converter and its operation is detailed in this subsection. This converter utilises two switches and two diodes for each phase, as depicted in Figure 33 for a 4ϕ SRM.

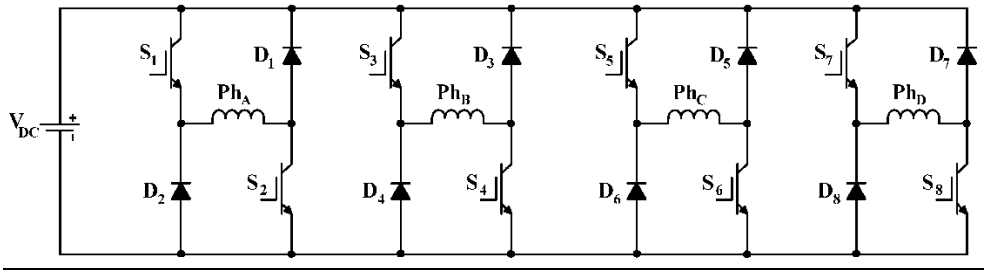

Figure 33 - Asymmetric half bridge converter for a 4ϕ SRM [13].

The ASHB converter operates in three states: magnetisation, free-wheeling, and demagnetisation. These states are illustrated in Figure 34, and the following description is for a specific phase, Ph_A.

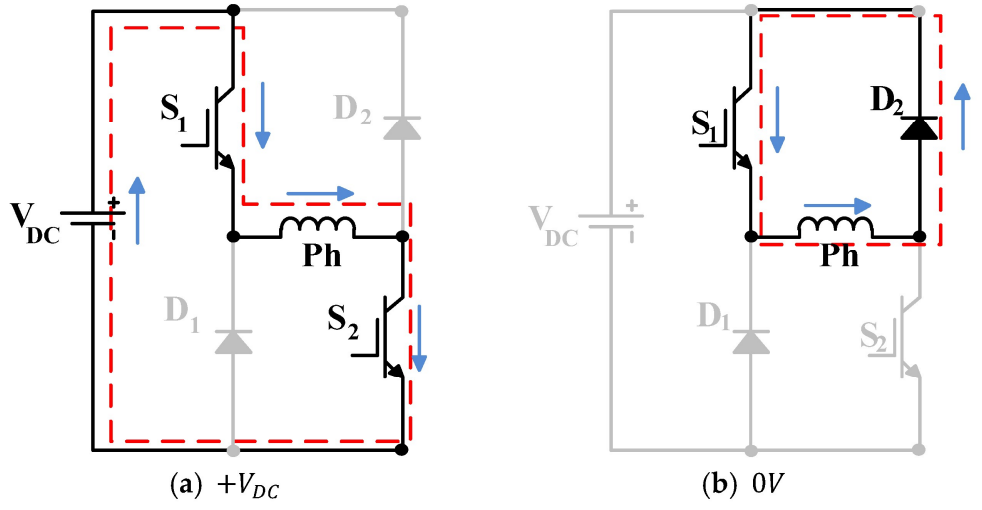

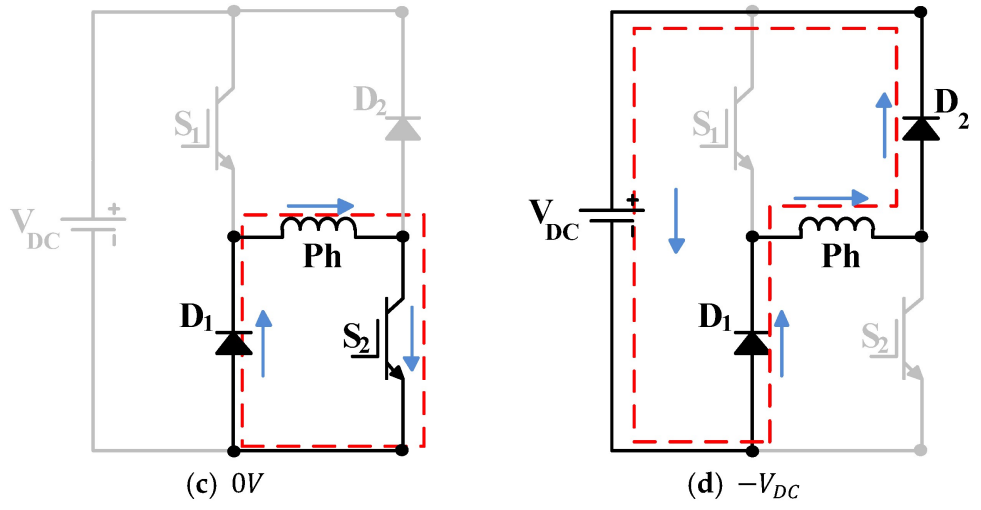

Figure 34 - ASHB converter states: (a) Magnetisation, (b,c) free-wheeling, and (d) demagnetisation [13].

Magnetisation ($+V_{DC}$): In this state, switches $S1$ and $S2$ of the phase to be energised are turned on, as shown in Figure 34a. This action applies the full DC link voltage to the phase, forcing the current to build up.

Freewheeling ($0V$): There are two possible switch patterns for this voltage level. The first pattern is with $S1$ on and $S2$ off, while the second pattern is with $S2$ on and $S1$ off. These patterns are illustrated in Figure 34 parts b and c, respectively, where zero voltage is applied across the phase winding. These two ($0V$) states can be alternated to balance bridge losses and heating.

Demagnetisation ($-V_{DC}$): In this state, switches $S1$ and $S2$ are both off, as shown in Figure 34d. The demagnetisation current (energy) from the motor winding is then pumped back to the DC link, with the winding current reducing to zero before the phase enters the region of negative torque production.

Table 5 shows a summary of the three available converter voltage levels, while Figure 35 depicts typical voltage and current waveforms for the three states.

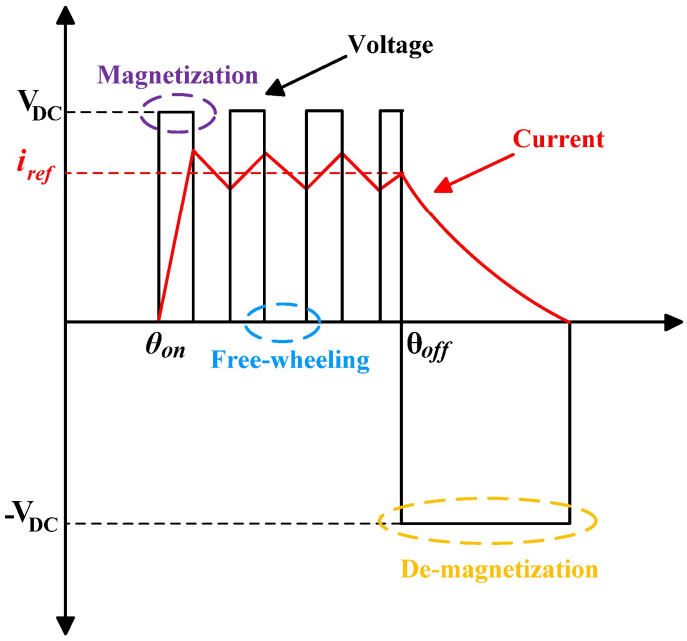

Figure 35 - Typical phase voltage and current waveforms with an ASHB [13].

Table 5 - ASHB converter states [13].

Level	Figure 3 State	State/KVL
$+V_{DC}$	Figure 3a	V_{DC}, S_1, S_2
$0V$	Figure 3b	D_2, S_1
	Figure 3c	D_1, S_2
$-V_{DC}$	Figure 3d	V_{DC}, D_1, D_2

Advantages:

- Independent control of each phase without overlap.
- Three available voltage levels, namely $+V_{DC}$, $0V$, $-V_{DC}$.
- Low complexity.
- High fault tolerance, with no link switch 'shoot through' path.
- High efficiency as stored magnetic energy in phase winding is fed back to the DClink during demagnetisation.

Drawbacks:

- Increase in semiconductor device number, as each phase requires two switches and two diodes.

- More conduction losses since two semiconductors are connected in series with the conducting phase winding.
- The relatively low magnetisation and demagnetisation voltage limits motor base speed.

Common-Phase Converters

The common-phase converter represents an advancement over the ASHB converter, offering the same benefits but with fewer switches (1.5 switches per phase). Shown in Figure 36, this converter is applicable to the 4ϕ SRM and employs a two-bridge topology. Phases A and C (mechanically at quadrature) are placed in one bridge, sharing a common leg with switch SAC, while phases B and D (mechanically quadrature phases) are in a second bridge with switch SBD, common to both phases B and D. This arrangement utilises the fact that phases sharing a switch in the same bridge are 180° (electrical) out of phase, preventing phase current conduction overlap.

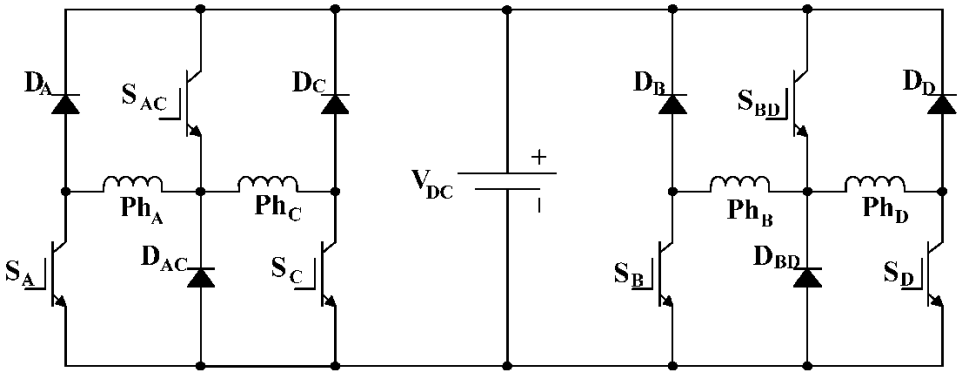

Figure 36 - Common-phase converter using two bridges [13].

This switch sharing topological approach is effective for SRMs with an even number of phases. Because of switch-sharing, its fault tolerance is reduced, since a fault in the common switch in either of the two bridges results in the loss of the phases incorporated in that bridge.

Common Switch Converter

To minimise the semiconductor device number in the ASHB converter, thus decreasing its cost and size, the common switch converter in Figure 37 was introduced.

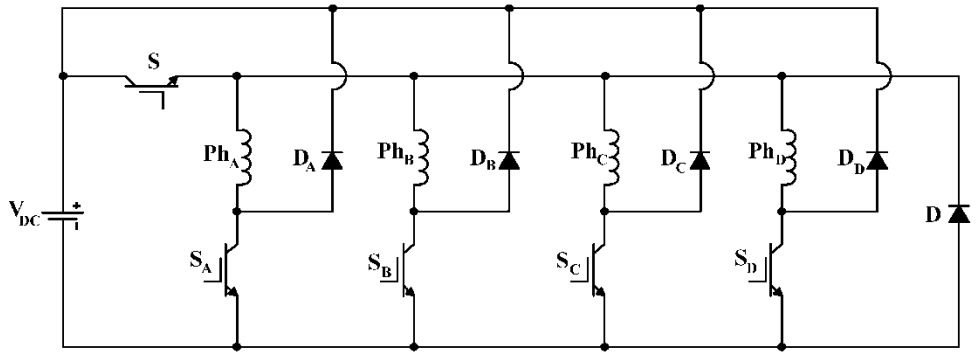

Figure 37 - Common switch converter [13].

In this configuration, every phase is equipped with its own switch. A main switch, denoted as *S*, is common to all phases, effectively lowering the total switch count to *n*+1 (where *n* is the number of phases). Despite its lower cost compared to the ASHB converter, this design sacrifices fault tolerance. It performs well at low speeds; at higher speeds, the off-going phase cannot be rapidly demagnetised (due to the common switch S being activated), leading to a prolonged current tail (only states *+V* and *0V* exist). This, in turn, generates negative phase torque, ultimately reducing the overall developed torque.

4.1.2. Dissipative Converters

The dissipative converter is often seen as the most basic SRM converter, using the fewest number of switches, with just one switch per phase. In this setup, the energy stored in the phase winding is not returned to the power supply but is instead dissipated in a dump resistor. Consequently, this converter is not energy efficient, thus unsuitable for EV application. There are two versions: R-dump

and modified R-dump.

R-Dump Converter

Figure 38 depicts the R-dump converter, in which the energy stored that is released in the phase winding is dissipated in the dump resistor, *Rd*. No *0V* state (loop) exists. This configuration exhibits low efficiency and necessitates specific cooling for the dump resistor. Therefore, it is best suited for low-power, cost-sensitive applications.

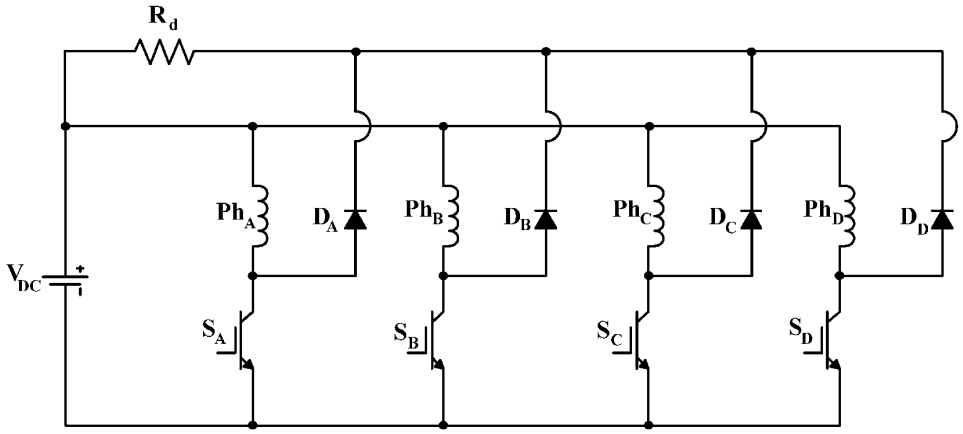

Figure 38 - R-dump converter [13].

Modified R-Dump Converter

A variant of the R-dump converter is shown in Figure 39, featuring an additional switch, S, connected in parallel with the dump resistor. The time constant for current decay is given by $L/(R + (1 - \alpha)R_d)$ (where, R and L are the phase winding resistance and inductance, respectively). By reducing the duty cycle, α, the effective dump resistance increases (as the $0V$ periods decease). Conversely, increasing the duty cycle reduces the effective dump resistance, enhancing efficiency during current chopping periods.

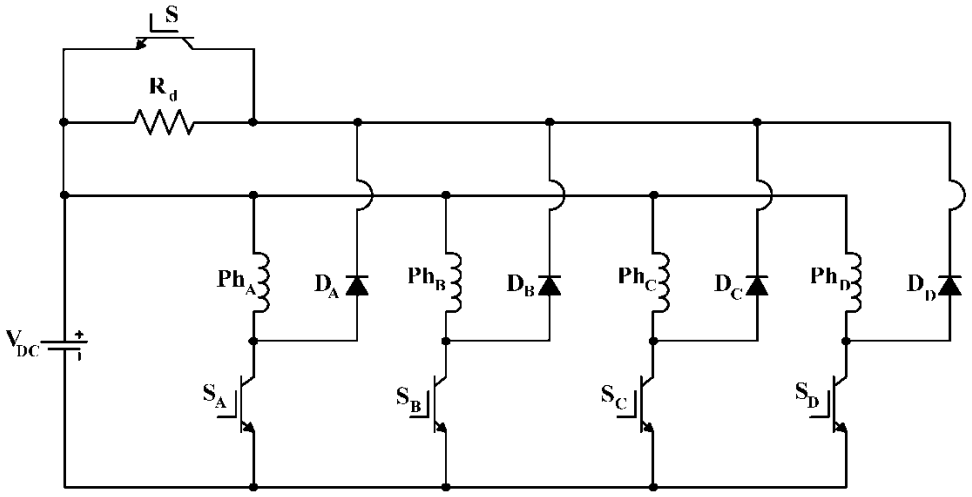

Figure 39 - Modified R-dump converter [13].

4.1.3. Magnetic Converters

The concept behind magnetic converters is to transfer the magnetic energy stored in the SRM phase to a coupled (bifilar) winding. This transferred energy can then be either returned to the power supply or used to energise the next incoming phase. Figure 40 depicts the configuration of a bifilar converter, which employs a single switch per phase, being the primary advantage. This configuration only supports two modes: magnetisation and demagnetisation. The free-wheeling mode is not feasible with this setup.

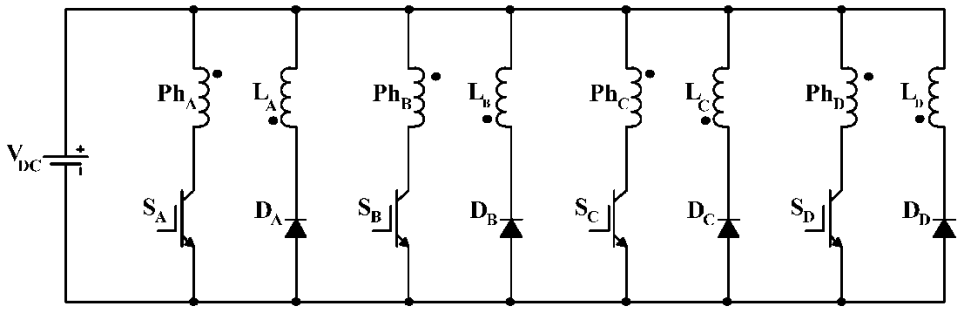

Figure 40 - Bifilar converter [13].

LA, *LB*, *LC*, and *LD* are the bifilar windings' effective inductances.

This converter does not waste the demagnetisation energy; instead, it is recycled. The primary drawback of this topology is that each SRM phase needs to be connected to another winding, which adds complexity to the SRM manufacturing and decreases the available copper area for the stator winding. Inadequate coupling between the SRM's bifilar windings (leakage inductance) leads to voltage spikes when a phase is turned off, necessitating the use of snubber circuits. With 1:1 coupled windings, the required semiconductor voltage ratings (diode and switch) are (at least) 2 V_{DC}.

4.1.4. Capacitive Converters

The capacitive converter employs a dump capacitor to store the demagnetisation energy, which is then either returned to the power supply or utilised to energise the next incoming SRM phase winding. Variants of capacitive converters include C-dump, modified C-dump, split DC link, and passive boost, and these are discussed in the following subsections.

C-Dump Converter

Figure 41 illustrates a C-dump converter, which is classified as belonging to the $n + 1$ family (meaning that the number of semiconductor switches equals the number of SRM phases, plus one).

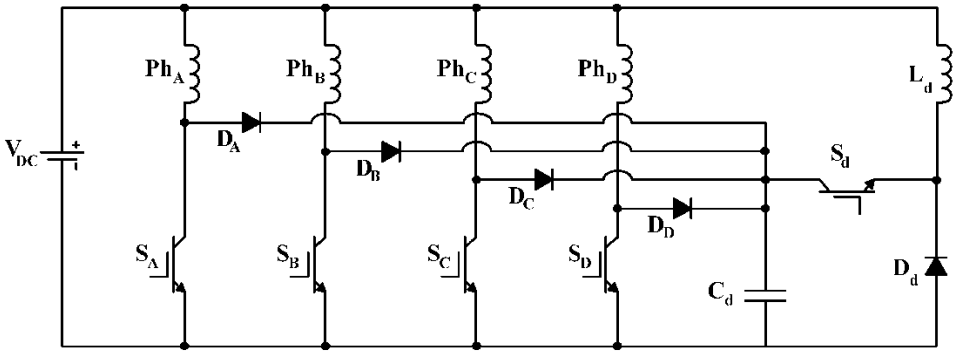

Figure 41 - C-dump converter [13].

The energy stored in the SRM phase winding is transferred to a capacitor, Cd. The voltage across the capacitor is maintained at twice the supply voltage, $2VDC$, to apply $-VDC$ to the outgoing phase for quick current extinction. The transferred energy is then returned to the DC link using a buck circuit consisting of Sd,Dd,and Ld.

However, this topology has drawbacks. No $0V$ state exists. It requires a large capacitor Cd and a buck converter (which includes a sizable inductor). The semiconductor devices need to be rated at double the DC link voltage. Additionally, to keep the voltage across the dump capacitor at $2VDC$, the switching frequency of Sd needs to be high, leading to increased switching losses.

Modified C-Dump Converter

C-dump converter performance is enhanced in Figure 42, where the inductor in the buck circuit is eliminated. The energy stored in the dump capacitor is utilised to directly power the next incoming phase instead of being fed back to the DC link.

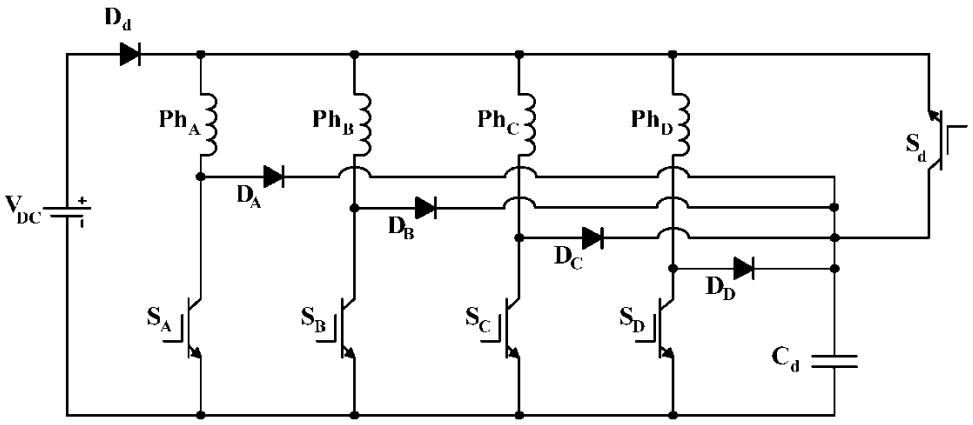

Figure 42 - Modified C-dump converter [13].

Despite the elimination of the inductor and the reduction in the switching frequency of Sd, the switches are rated at $2VDC$, similar to the C-dump converter. The circuit control is complex, leading to suboptimal performance at high speeds.

Split DC Link Converter

The split DC link converter in Figure 43 features a single switch per phase, thereby lowering the overall switch count. However, it necessitates an SRM with an even number of phases. It utilises only half of the DC link voltage for the magnetisation and demagnetisation of incoming and outgoing phases, respectively. This approach prevents rapid current buildup and decay, thereby limiting the SRM base speed. This converter cannot withstand any phase failure or phase imbalance.

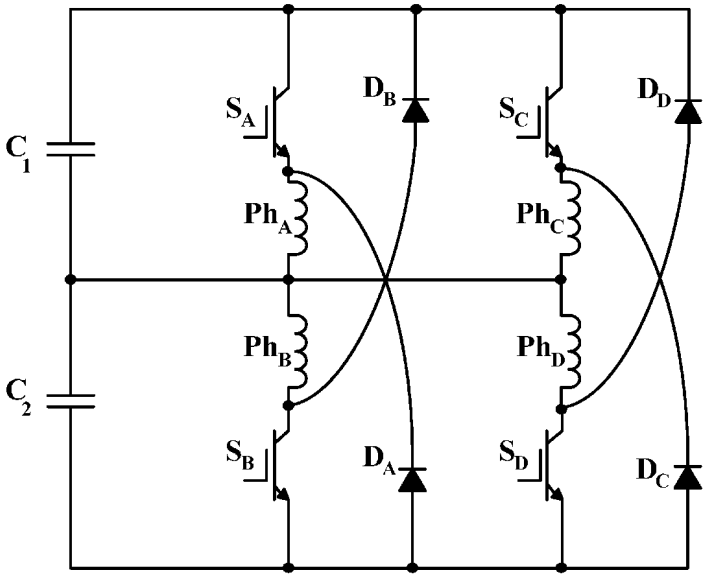

Figure 43 - Split DC link converter [13].

Passive Boost Converter

Improving SRM performance at high speeds a boost capacitor with a blocking diode is introduced into the DC link. The demagnetisation energy from the outgoing phase is stored in the boost capacitor, reducing the current decay time and effectively extending the range of positive torque production before entering the negative torque region.

The stored energy, which raises the DC link voltage, is then transferred to the next incoming phase, enabling faster current buildup and increasing the motor base speed. Figure 44 illustrates a typical common-phase converter with boost capacitors.

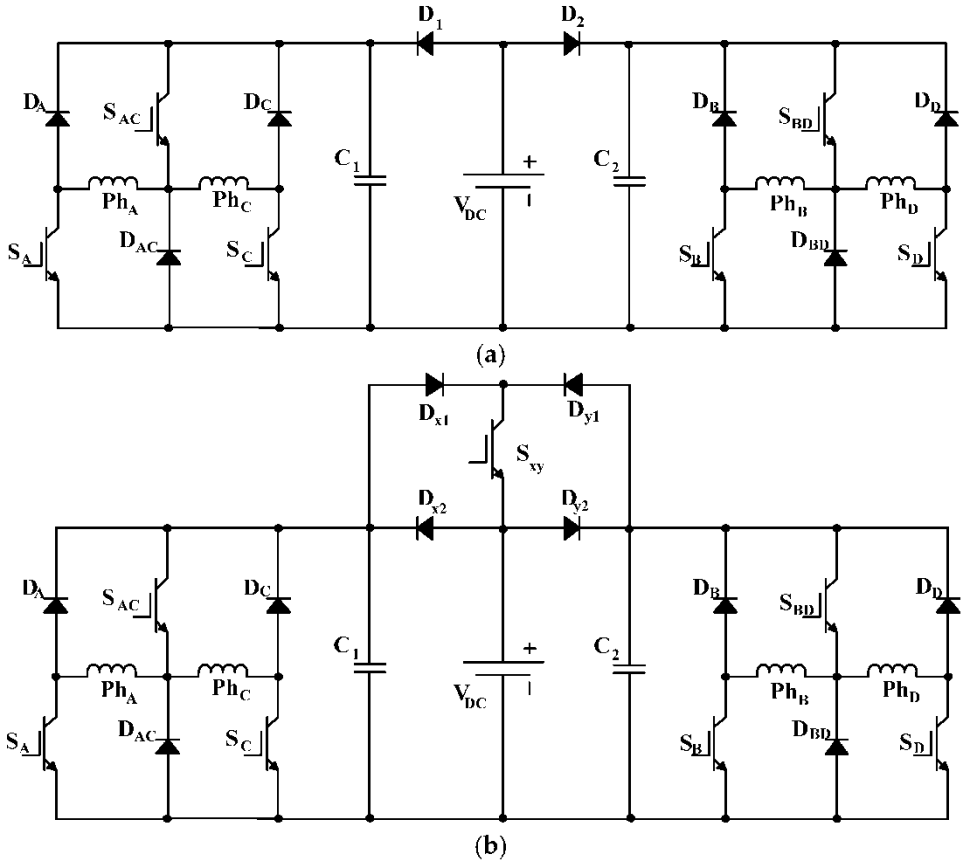

Figure 44 - Common-phase converter with passive boost capacitors: (a) Without regenerative braking and (b) with regenerative braking circuitry [13].

The converter employs a double bridge topology, with phases A and C grouped in one bridge, sharing a common leg that includes switch *SAC*. The remaining two phases, B and D, form an independent bridge with a common switch *SBD*. By utilising the DC-link-blocking diodes and capacitors, the converter can boost the DC link voltage by

directing the recovered current to charge the capacitors to levels exceeding the DC source voltage, VDC.

This two-independent bridge configuration allows for more effective voltage boosting (as there is no phase overlap within each bridge) while using a minimal number of switches, as illustrated in Figure 44a. However, a drawback of this topology is that it requires semiconductor devices rated above the DC link voltage (with ratings dependent on the boost voltage). Additionally, due to the presence of DC-link-blocking diodes, circuit modifications are necessary for regenerative braking, if required.

Figure 44b shows the modified voltage-boosting common-phase converter with the regenerative braking circuitry. During braking, the stored energy in the phase winding is not dissipated but returned back to the DC link. However, this energy cannot be pumped to the DC link capacitors, as the capacitors' voltages will excessively increase. Therefore, the DC link switch Sxy and diodes D_{x1} and D_{y1} are needed to direct the phase winding energy to the DC link rather than to the capacitors.

4.2. Flying capacitor multilevel inverter

The implementation of conventional two-level converters in Switched Reluctance Motor (SRM) drives presents substantial operational challenges, necessitating the investigation of multi-level converter topologies [17]. Despite their widespread adoption, two-level architectures exhibit inherent limitations in managing critical performance parameters. Specifically, they are associated with elevated current ripple, excessive power dissipation during high-frequency switching, and significant electromagnetic interference (EMI). These factors collectively constrain the potential for optimal efficiency and reliability within SRM systems.

Conversely, multi-level converters provide a robust solution to these deficits. Through superior voltage modulation capabilities and the generation of smoother output waveforms, these advanced topologies effectively attenuate current ripple, mitigate switching losses, and suppress EMI. Consequently, the enhanced operational characteristics and superior efficiency offered by multi-level converters position them as the optimal solution for overcoming the intrinsic limitations of standard SRM drive systems.

The multi-level inverters are able to reduce the voltage stress on the semiconductors. Therefore, the inductor size can be decreased. As compared to the two-level inverter the semiconductor cost is higher, but the output filter is smaller and less expensive. Let's imagine that the advantages of two and three level topologies can be combined into a single inverter. The flying capacitor inverter combines low semiconductor costs and gives a multi-level output with high output frequency and low dynamic losses.

In the flying capacitor topology, the additional voltage levels are synthetized by high frequency capacitors, so-called flying capacitors. Here, the flying capacitors provides offset for the output, so the output voltage is the sum or the difference of the voltage levels. The schematic of the three-level flying capacitor inverter can be seen in Figure 45.

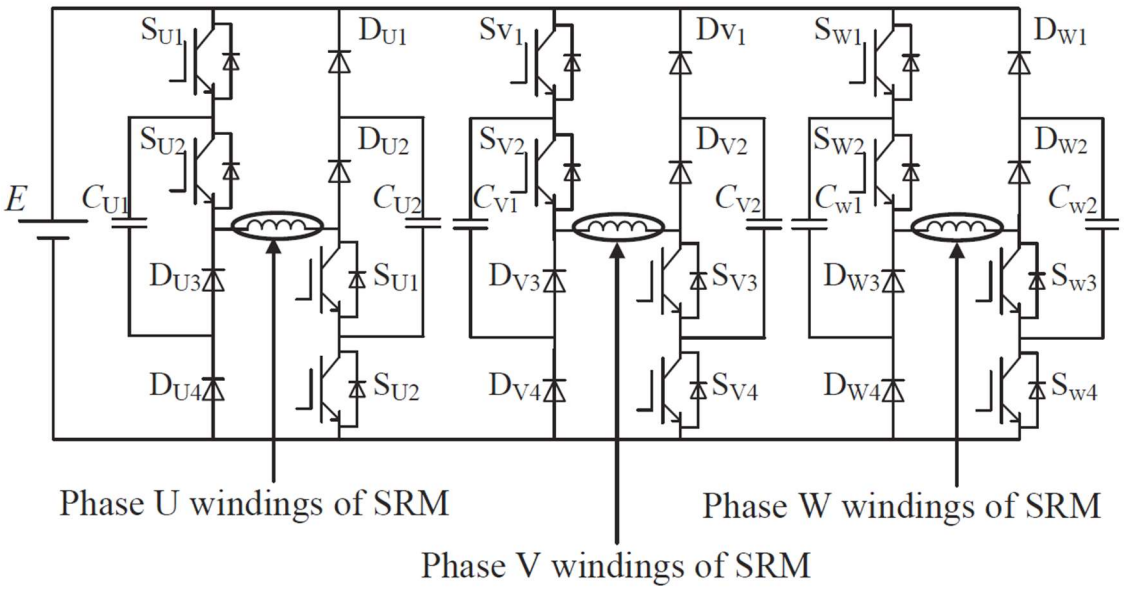

Figure 45 - Three level flying capacitor inverter [18]

In the three-level case the average voltage of the flying capacitor is half of the DC-link voltage (V_{DC}/2).

In flying capacitor inverter topologies, the commutation loops include capacitors. A capacitor from the commutation point of view can be considered zero impedance [19]. Its main role in the commutation loop is to offset the two outer semiconductors from each other. With this offset, the three level flying capacitor topology can be considered as two standalone half-bridges, where the outer one's commutation loop includes the DC-link capacitor, the outer diodes, the flying capacitor and the outer switches. The inner commutation loop includes the flying capacitor, the inner diodes and the inner switches. As the commutation loops are half-bridges, the loss calculation and the driving method are also similar for it (only the losses of the capacitors have to be added). The main constraint is also the same, all the two switches in each half-bridge must not be switched on at the same time. If all the two inner switches are switched on, the flying capacitor would be shorted. If all the outer switches are turned on the DC-link and the flying capacitor would be shorted, which can damage the inverter. The two commutation loops can be seen in Figure 46.

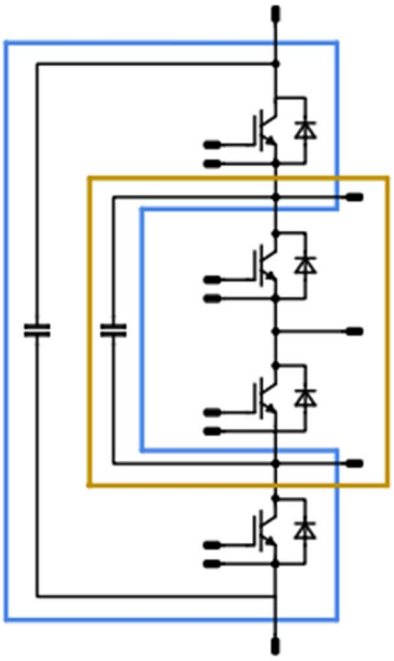

Figure 46 - The commutation loops of the three-level flying capacitor Inverter

In general, the number of voltage levels are theoretically endless, but in practice three, four and five levels are used. The additional levels in n level solution can be realized by adding extra outer commutation loops to the three-level converter. Every added half-bridge's commutation loop will be similar to the blue loop in Figure 2. The number of voltage levels can be calculated as following:

$$n_{level} = p + 1$$

(4.3. 1)

Where p is number of the commutation loops (half-bridges). The voltage of the capacitor can be calculated:

$$V_{FC,i} = V_{DC} \cdot (1 - \frac{i - 1}{p})$$

(4.3. 2)

Where i is number of the given commutation cell. The first loop refers always to the most outer loop. $V_{FC,1}$ refers to the DC-link capacitor.

This application note covers the operation of the flying capacitor inverter. For easier understanding the three-level version will be explained but the principles can be applied for any number of voltage levels.

To better understand the working mechanism, now considering an n level flying capacitors multi-level inverter FCMI [20], (n−1)(n−2)/2 flying capacitors are used across each phase leg and the voltage across each capacitor is (Vdc)/(n−1). As the flying capacitors are charged to their respective voltage levels, they provide the additional voltage levels by performing the correct switching strategy. Hence, as the number of levels increases, the number of capacitors will also significantly increase which could make the device bulky. It is important to also consider the size of flying capacitors to have lower voltage ripple for the flying capacitors as well. For a three level FCMI, the additional zero level is achieved by making use of flying capacitors. The circuit diagram for the FCMI for a single phase leg has been shown in Figure 47. This topology has two different switching states to produce the zero-voltage level. Hence it is necessary that both these switching states are equally used to ensure that the corresponding switches are evenly stressed.

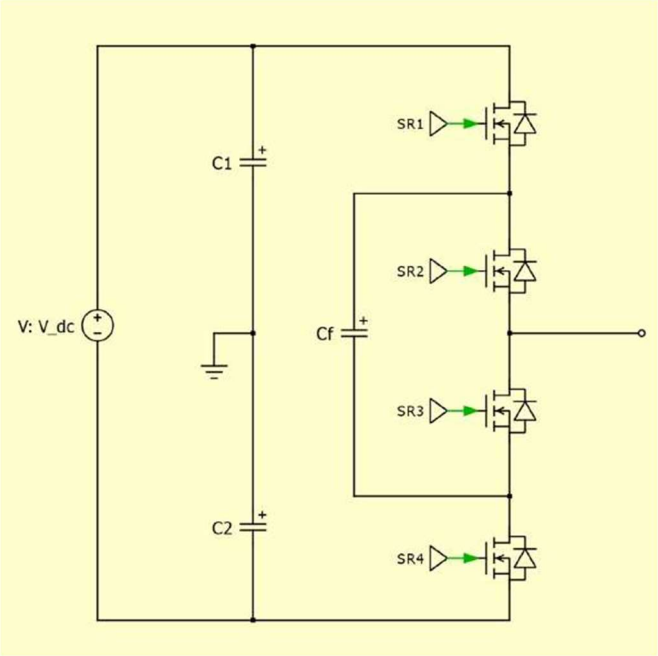

Figure 47 - Single phase leg of the FCMI [20]

For a positive current output, all the switching states for the FCMI can be seen in Figure 48and in Table 6. The similarity regarding to the operation of the NCMI topology can be seen here for for producing the positive and negative voltages. The DC voltage is split into two by the DC link capacitors, which is Vdc/2. The flying capacitors shall also have a voltage of Vdc/2. In case 1, switches SR1 and SR2 are on to produce the positive voltage. Cases 2 and 3 show the two zero level switching states. For the FCMI, these two switching states need to happen alternatively. This automatically provides voltage balancing for the flying capacitors present in each phase leg. In case 2, the voltage

produced due to C1 is opposed by Cf and the capacitor goes into a charging state. In case 3, the voltage produced due to C2 is opposed by Cf and the capacitor goes into a dis-charging state. In case 4, switches SR3 and SR4 are on to produce the negative voltage. The voltage across all switches shall now be only Vdc/2.

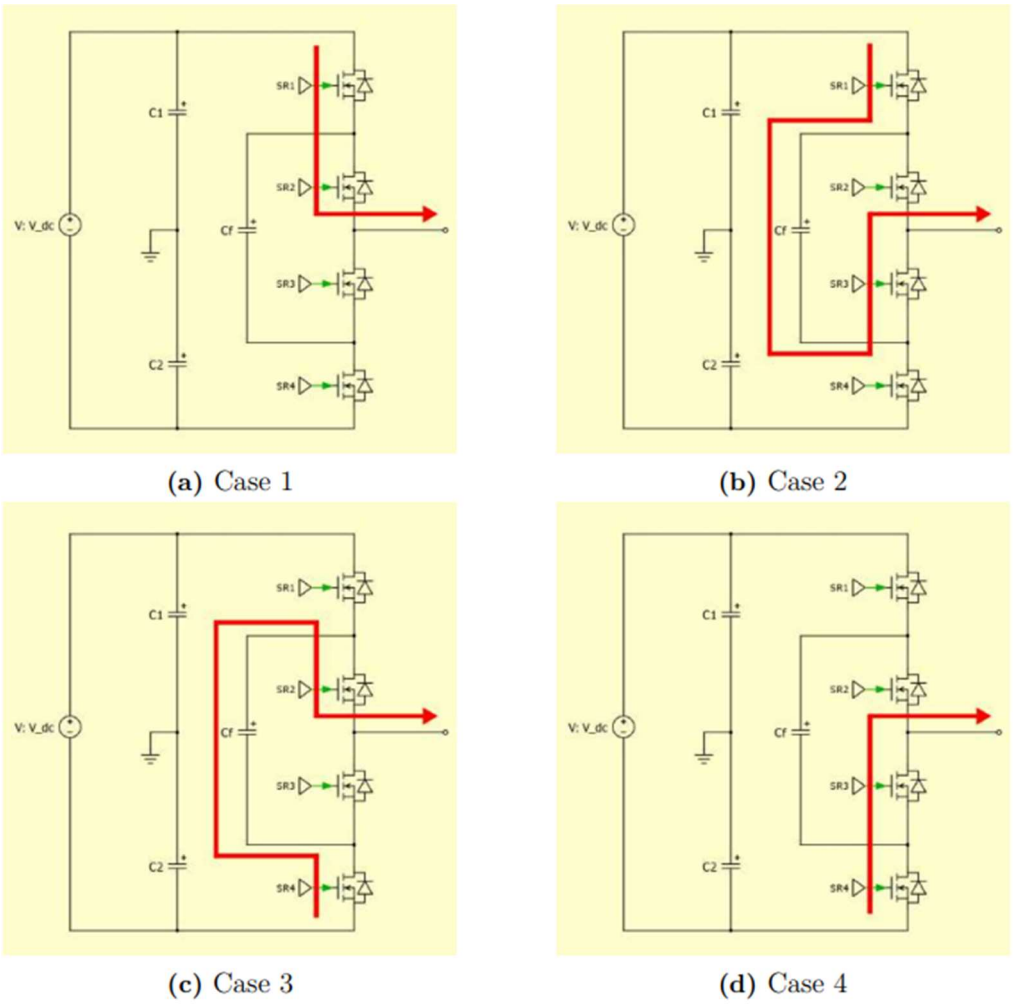

(a) Case 1 (b) Case 2

(c) Case 3 (d) Case 4

Figure 48 - Switching states for three phase level FCMI [20]

Table 6 - FCMI - Switching states [20]

Switching State	Phase Voltage	***S1***	***S2***	***S3***	***S4***
Case 1	$\frac{V_{DC}}{2}$	On	On	Off	Off
Case 2	0	On	Off	On	Off
Case 3	0	Off	On	Off	On

Case 4	$-\frac{V_{DC}}{2}$	Off	Off	On	On

Balancing the flying capacitor voltage is an important aspect of this topology. For the appropriate operation of the inverter the flying capacitor voltage has to be half of the input voltage. For the voltage regulation the voltage of the flying capacitor, the input voltage and the output current direction need to be considered. Those have to be measured in the inverter. As it was presented previously, the flying capacitor voltage during the neutral states can be charged or discharged (Table 7). There are two ways to approach. The various modes can be considered as states which changing in a determined sequence. In normal operation the sequence is the following in the first half-period:

…Case1→ Case 2→ Case 1→ Case 3→ Case 1…

In the second half-period it is:

… Case 4→ Case 2→ Case 4→ Case 3→ Case 4…

If the duration of one of the neutral states (Mode two or Mode three) changes, the flying capacitor voltage will change accordingly. As the output duty cycle should not change, the increase of one neutral state should be compensated by decreasing the other. It is also possible to use only one neutral state instead of two. As a result, the change of the flying capacitor voltage will be faster.

… Case 1→ Case 2→ Case 1→ Case 2→ Case 1…

or

… Case 1→ Case 3→ Case 1→ Case 3→ Case 1… in the first half-period.

Table 7 - Output and FC voltage states [19] [20]

Switching State	**Phase Voltage**	**Transistor**				**FC voltage**	
		S1	**S2**	**S3**	**S4**	Positive current	Negative current
Case 1	$\frac{V_{DC}}{2}$	On	On	Off	Off	No effect	
Case 2	0	On	Off	On	Off	Increasing	Decreasing
Case 3	0	Off	On	Off	On	Decreasing	Increasing

Case 4	$-\frac{V_{DC}}{2}$	Off	Off	On	On	No effect

The state diagram can be seen in Figure 49.

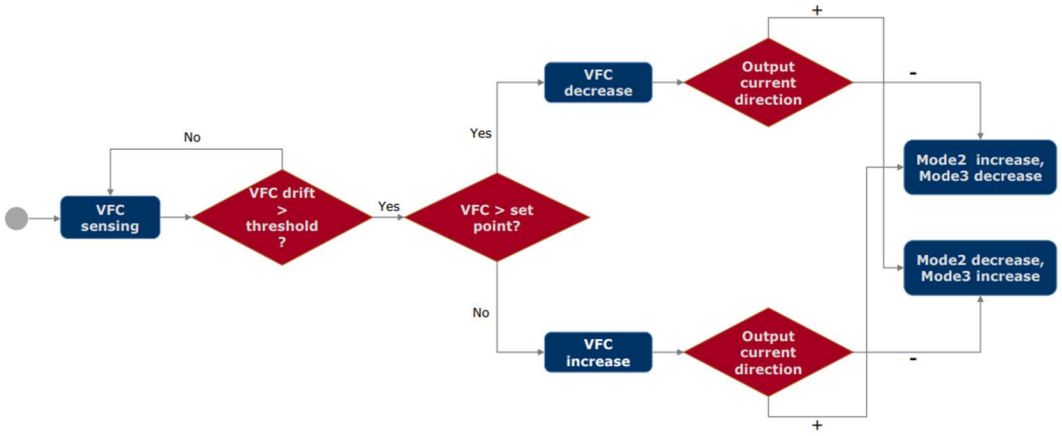

Figure 49 - Voltage balancing state diagram

The control of the flying capacitor voltage can also be achieved by modifying the PWM signals. Here also the duration of the neutral states have to be modified. As a result the flying capacitor voltage changes. To change the duration an offset has to be added to one of the modulation signals. Then, one of the neutral states will be longer. To keep the same duty cycle on the output the inverse of the offset has to be added to the other modulation signal to shorten the other neutral state. In this way the output average voltage remains the same and the flying capacitor voltage will change.

In both ways the action has to be chosen based on the capacitor voltage and the output current. So, if the current direction is changed, the action also have to be inverted (changing state or inverting the offsets) for the correct direction of the flying capacitor voltage changing.

In [18] is shown another conventional circuit Figure 45, and Table 8 shows the operation modes and the switching states for this conventional circuit. Where, S_{x1} corresponds to S_{U1}, S_{V1} and S_{W1}; S_{x2} corresponds to S_{U2}, S_{V2} and S_{W2}; S_{x3} corresponds to S_{U3}, S_{V3} and S_{W3}; V_{xL} represents the winding voltage in phase x (x=U, V ,W). Also,

operation modes that the circuit can apply positive half voltage ($\frac{E}{2}$) and negative half voltage (- $\frac{E}{2}$). In Table 8 is reported also the logic which the system maintains balanced the capacitors in all the situation, where the motor work as a generator or works in all the freewheel condition, discharging or charging the correct capacitors to maintain the correct voltage level.

Table 8 – Switching state and applied voltage to the winding in each phase

Mode	S_{x1}	S_{x2}	S_{x3}	S_{x4}	V_{xL}	Notes
0	OFF	OFF	OFF	OFF	-E	Motor as generator
1	ON	OFF	OFF	OFF	-E/2	Motor as generator, charge C_{sx}
2	OFF	ON	OFF	OFF	-E/2	Motor as generator, discharge C_{sx}
3	ON	ON	OFF	OFF	0	Freewheel
4	OFF	OFF	ON	OFF	-E/2	Motor as generator, discharge C_{dx}
5	ON	OFF	ON	OFF	0	Freewheel, charge C_{sx}, discharge C_{dx}
6	OFF	ON	ON	OFF	0	Freewheel, discharge C_{sx}, charge C_{dx}
7	ON	ON	ON	OFF	E/2	Motor, discharge C_{dx}
8	OFF	OFF	OFF	ON	-E/2	Motor as generator, charge C_{dx}
9	ON	OFF	OFF	ON	0	Freewheel, charge C_{sx}, charge C_{dx}
10	OFF	ON	OFF	ON	0	Freewheel, discharge C_{sx}, charge C_{dx}
11	ON	ON	OFF	ON	E/2	Motor, charge C_{dx}

12	OFF	OFF	ON	ON	0	Freewheel
13	ON	OFF	ON	ON	E/2	Motor, charge C_{sx}
14	OFF	ON	ON	ON	E/2	Motor, discharge C_{sx}
15	ON	ON	ON	ON	E	Motor, max power

The flying capacitor inverter is a highly efficient low cost solution for inverter applications. As the input is only two level in three phase application there is no need for enormous DC-link capacitors. However, the output is three level, and the output frequency is a multiple of the switching frequency. The main advantages are the low capacitance needed on the input, the frequency multiplication, what is resulting in lower switching losses, smaller inductor or current ripple on the output and the lower EMI emission. The lower switched voltage enables higher system voltage with the same components, or the components voltage rating can be reduced, also leading to lower switching losses. The challenges of startup and the flying capacitor voltage balancing can be addressed easily. The above mentioned facts reduce the inverter costs and increase the lifetime of the inverter as compared to traditional topologies and the flying capacitor inverter became a strong alternative to them.

4.2.1. Design of flying capacitor

The voltage supplied by the flying capacitor has a key role in this topology. To keep the voltage ripple of the capacitor low a suitable capacitor size is needed. To determine the minimum needed capacitance the switching frequency, the output current and the maximum allowed voltage ripple need to be considered. The size of the capacitance can be calculated as:

$$C_{FCmin} = \frac{I_{peak}}{\Delta V_{FC} * p * f_{SW}} \tag{4.3. 3}$$

Where ΔV_{FC} is the maximum allowed voltage ripple, $Ipeak$ is the maximum current, p is the number of the commutation cells, and f_{SW} is the switching frequency of the transistors.

Before starting the inverter, the voltage of the flying capacitor is zero. Before normal operation it must be charged to the adequate voltage level. If the inverter would be started without a charged flying capacitor, the inner half-bridge would get full DC-link voltage. The capacitor would be charged instantaneously, resulting in a short circuit current on the outer switches and on the flying capacitor, while the inner switch and the flying capacitor would get over voltage. There are two ways to address the pre-charge challenge. One is the passive one, the other is the active pre-charge one. In case of passive pre-charge, a resistive voltage divider is used on the input of the inverter, which will set the flying capacitor voltage before starting. This can be seen in Figure 8. In this case a resistor is used in parallel with the flying capacitor (R2) with the same resistance as the sum of resistors between DC+ FC+ (R1) and FC- DC- (R3). As the voltage divider will dissipate during the normal operation high resistance values have to be used. However, the startup time also depends on the resistance. So, the higher the resistance, the longer the startup. The starting time can be calculated from the value of the resistors and the capacitor.

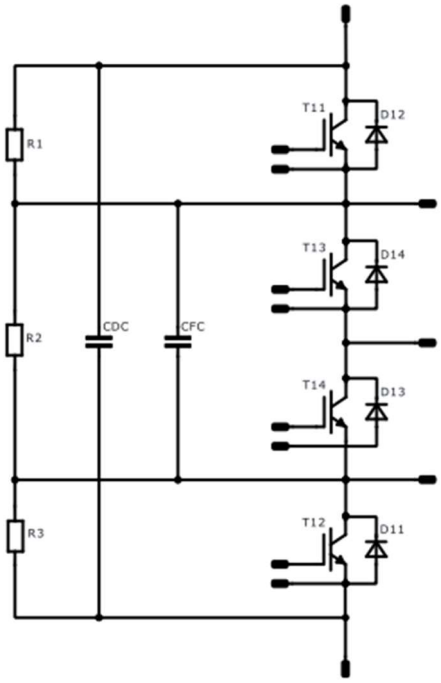

Figure 50 - The passive pre-charge

It can be calculated with Kirchhoff's Current Law:

$$\frac{V_{DC} - v_{FC}(t)}{R_1 + R_3} - \frac{v_{FC}(t)}{R_2} = C * \frac{dv_{FC}(t)}{dt} \tag{4.3. 4}$$

Given that:

$$R_1 + R_3 = R_2 = R \tag{4.3. 5}$$

Resulting in:

$$\frac{V_{DC} - 2 * v_{FC}(t)}{R} = C * \frac{dv_{FC}(t)}{dt} \tag{4.3. 6}$$

Concluding:

$$v_{FC}(t) = \frac{V_{DC}}{2} + c_1 * e^{-\frac{t}{\frac{R}{2}*C}} \tag{4.3. 7}$$

The voltage is changing by an exponential function bearing to $\frac{V_{DC}}{2}$. As the voltage won't reach $\frac{V_{DC}}{2}$ the starting time has to be calculated until it will reach the regulation range (e.g., 90% of $\frac{V_{DC}}{2}$). At t = 0s the voltage of the capacitor is zero. Given that, $c_1$can be calculated.

$$V_{FC} = 0; t = 0$$
$$0 = \frac{V_{DC}}{2} + c_1$$

(4.3. 8)

Resulting in c_1 equal to $-\frac{V_{DC}}{2}$.

Helding on:

$$v_{FC}(t) = \frac{V_{DC}}{2} - \frac{V_{DC}}{2} * e^{-\frac{t}{\frac{R}{2}*C}}$$

(4.3. 9)

By this, the time constant is:

$$\tau_1 = \frac{R}{2} * C$$

(4.3. 10)

The other way is active charging. In this case, a resistor has to be added in series with the inverter for limiting the inrush current after the outer switches are switched on simultaneously. The DC-link voltage should be connected to the inverter. With this method the integrated DC link capacitor won't be discharged. This can be seen in Figure 10. The capacitors will charge with τ_2 time constant.

Where:

$$\tau_2 = R * C$$

(4.3. 11)

If an integrated DC-link capacitor is assembled in the power module, the charging resistor cannot be placed between the capacitor and the module. In this case:

$$C = C_{FC} + C_{DC}$$

(4.3. 12)

When the flying capacitor reaches $\frac{V_{DC}}{2}$, the outer switches should be switched off immediately. So, the flying capacitor won't be overcharged. After switching off the outer switches the integrated DC-link capacitor will be charged further. The changing of the capacitor voltage can be calculated:

$$\frac{V_{DC} - v_{FC}(t)}{R} = C * \frac{dv_{FC}(t)}{dt}$$
$$v_{FC}(t) = V_{DC} + c_2 * e^{-\frac{t}{R*C}}$$

(4.3. 13)

At t = 0 s, $V_{FC} = 0V$. Resulting in:

$$v_{FC}(t) = V_{DC} - V_{DC} * e^{-\frac{t}{R*C}}$$

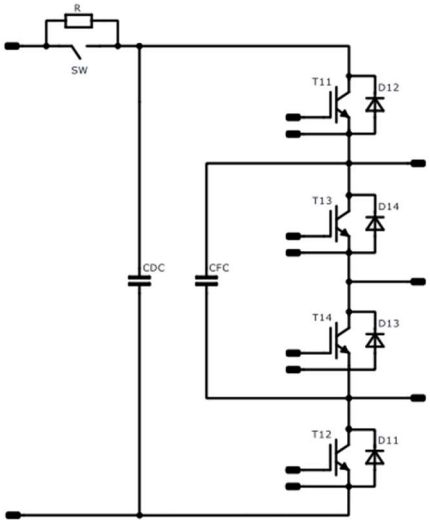

Figure 51 - The active pre-charge

To reduce losses, another switch or relay should be used to eliminate the limiting resistance when the inverter has started.

5 MATLAB SIMULATION

The Switched Reluctance Motor (SRM) has emerged as a compelling candidate for the hybrid and electric vehicle (EV) sectors, primarily due to its robustness, simple construction, and cost-effectiveness. A key advantage of the SRM is its reliance on widely available materials, which eliminates the industry's dependency on permanent magnets, while still offering desirable torque-speed characteristics. However, despite these benefits, the widespread adoption of SRMs in traction applications is currently limited by high torque ripple.

This phenomenon is an intrinsic consequence of the SRM's method of electromagnetic torque production. Phase commutation leads to a segmented torque profile caused by the overlapping contributions of incoming and outgoing phases. Coupled with the machine's high non-linearity, this discrete nature results in significant torque ripple during the transfer of production from one phase to the next. In servo and traction applications, where smooth torque is fundamental, this is a major concern, it generates acoustic noise, dominated by radial vibration around the pole alignment position, and mechanical vibration stresses. These issues can induce mechanical resonance effects and speed oscillations, which are particularly undesirable at low speeds.

To successfully implement SRMs in EVs, it is essential to minimize torque ripple across the entire speed and torque range. This necessity spans all driving conditions, from acceleration, where torque ripple is critical, to constant speed operation, where the motor must strictly counterbalance resistive forces (such as rolling resistance and aerodynamic drag), and finally to deceleration and regenerative braking. To address the perceived limitation of SRM torque ripple in EV applications, it is essential to minimise torque ripple across the entire speed and torque ranges.

That’s why, in this chapter is analysed the torque ripple reduction using MATLAB Simulink, operating on multi-phase switched reluctance machine, based on:

- Five level hysteresis analysis
- Flying capacitor inverter
- Accurate current profile
- Phase overlapping

In this simulation the chosen switched reluctance motor is the 6/4, so the one with 6 stator poles and 4 rotor poles, the choice held on this SRM because is the most compact one and the one with more torque ripple, due to the major space that persists between the stator and rotor poles, respect the motor with more poles.

The motor parameters applied in this study are related to articles which deal with SRM applied to a hybrid electric vehicle [21], [22]. These articles suggest a high power SRM for hybrid electric vehicle providing a motor with a continuous power of 20kW, up to 30kW of maximum power, accompanied by a voltage of 300 and 400 V.

5.1. Starting model

The first point of this simulation is the analysis of SRMotor throw a proper simulation dynamic, in particular the starting model on Matlab Simulink provides a non-linear model used to study the strategies to reduce the torque ripple.

This model is obtained from the Simulink libraries and provide the ideal SRMotor 6/4, as shown in Figure 52.

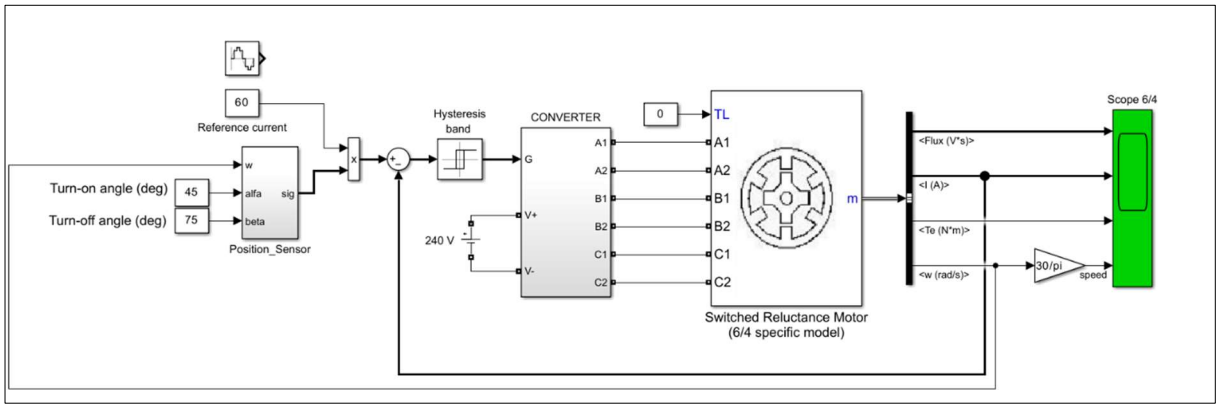

Figure 52 - Switched Reluctance Motor 6/4, base Simulink model

This model is composed by:

- Position sensor (Figure 53), that works with two angles, the one named "Turn-on angle" and the second named "Turn-off angle". These angles establish when it's time to excite the phase, this subsystem works with 90 angle loops, so one quarter of a complete round. The logic consists of excite the correct phase based on the comparison between the angle speed, w (rad/s), that is processed by the "Discrete-Time Integrator" and the two switch angles.

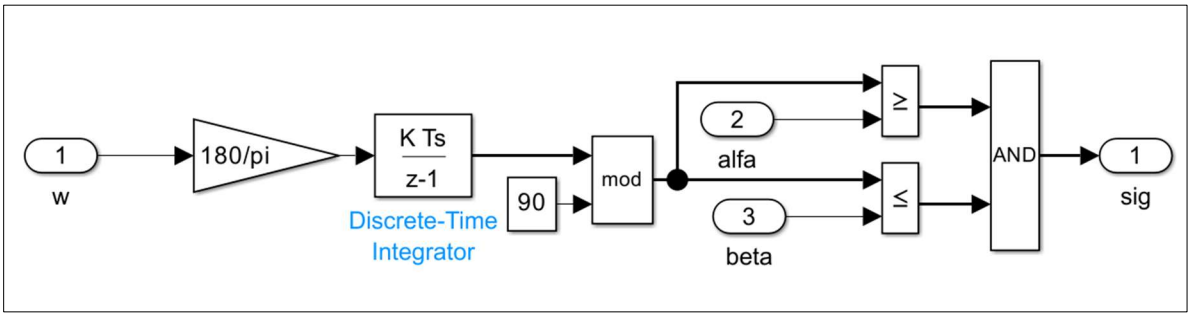

Figure 53 - Position sensor, base Simulink model

This subsystem provides a vector "G" 3x1 (3 row in 1 column), that determines the correct phase to excite, for example if the correct one is the first phase (phase A), the vector must be 1 - 0 - 0.

- Hysteresis band, this is the current control, because once the reference current is set (60 A in this study), the motor follows a current shape near the reference current value maintaining his value within two threshold values that is a mirror value that create a band of respect, in this base model the threshold band goes from 5 to -5.
- Converter (Figure 54), in this base model the converter used is the asymmetric h-bridge converter, with three branch for each phase, the branch is made of two IGBT e two diode, the input "G" provide a command input that close the contact inside the IGBT and thanks to this the current can pass and flow direct in the motor.

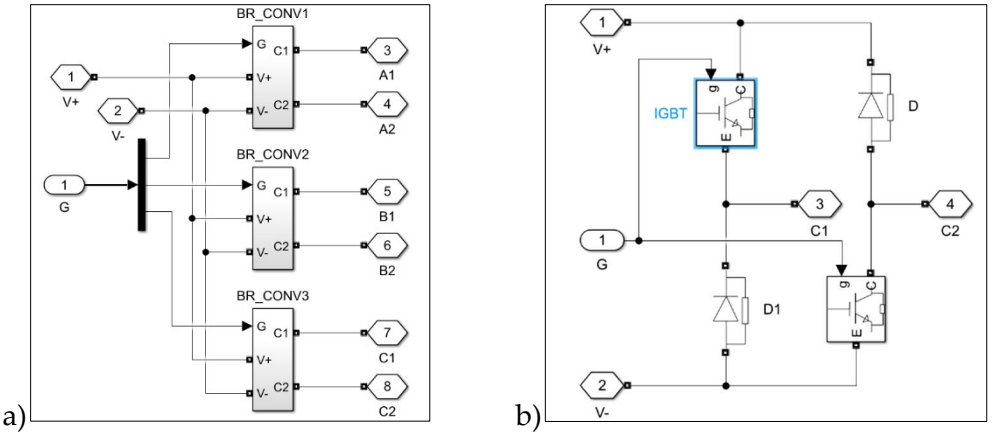

Figure 54 - a) converter; b) single branch - base Simulink model

- Switched Reluctance Motor 6/4, the motor uses two look-up tables, that are implicit and proprietary of MathWorks, to interpolate all the variables with the current position. Throw the look-up tables, flux, current and torque can be obtained. These tables summarize, in base on which table is used, in all the possible positions, depending by the current, the corresponding value thanks to the implicit inductance of the material. So, to create the table, in each position the motor was tested with several current values, to obtain the caused inductance. That's because the inductance depends on the current and on the position but also the current depends on inductance and position, and every value depends on the voltage, so for this study case the proprietary tables of MathWorks are used.

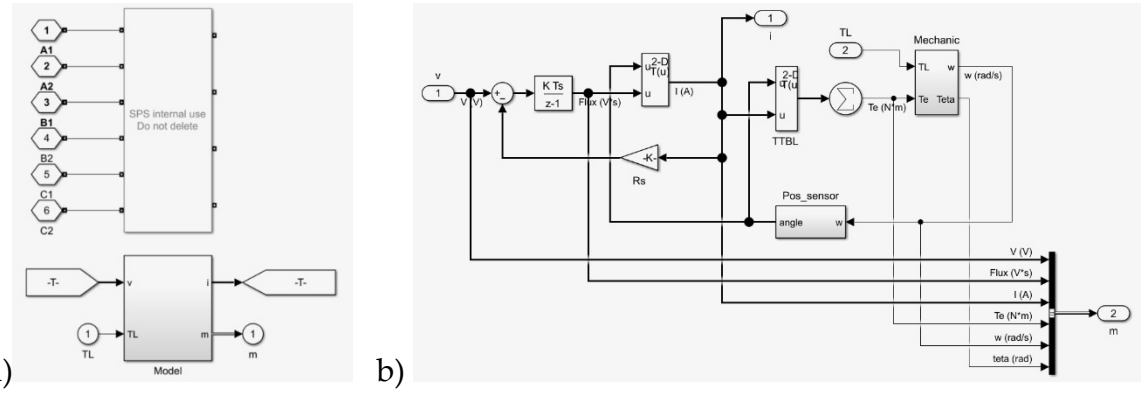

Figure 55 – a) Detail of SRM 6/4, base Simulink model, b) Detail of subsystem "model"

Therefore, the motor is tested. The input values as reported above, are 400 V and a reference current of 60 A.

The Figure 52, shows also the "scope 6/4", that is a Simulink block which is used to represent through graphs any data, showing the data drawn in the y-axis, related to time represented in x-axis. This "scope 6/4" reports in different graphs the outputs of the SRM, in detail the Flux (V*s), the current (A), the torque (N*m) and the speed (rpm).

To accurately simulate the dynamic behavior of the Switched Reluctance Motor, a non-linear model was adopted within the Simulink environment. The generic linear inductance model is insufficient for an SRM, as it fails to account for magnetic saturation and precise torque ripple generation.

Figure 56 illustrates the magnetization characteristics (flux linkage related to current) utilized by the specific SRM block in the simulation. The curves represent the magnetic behaviour of the motor at different rotor positions.

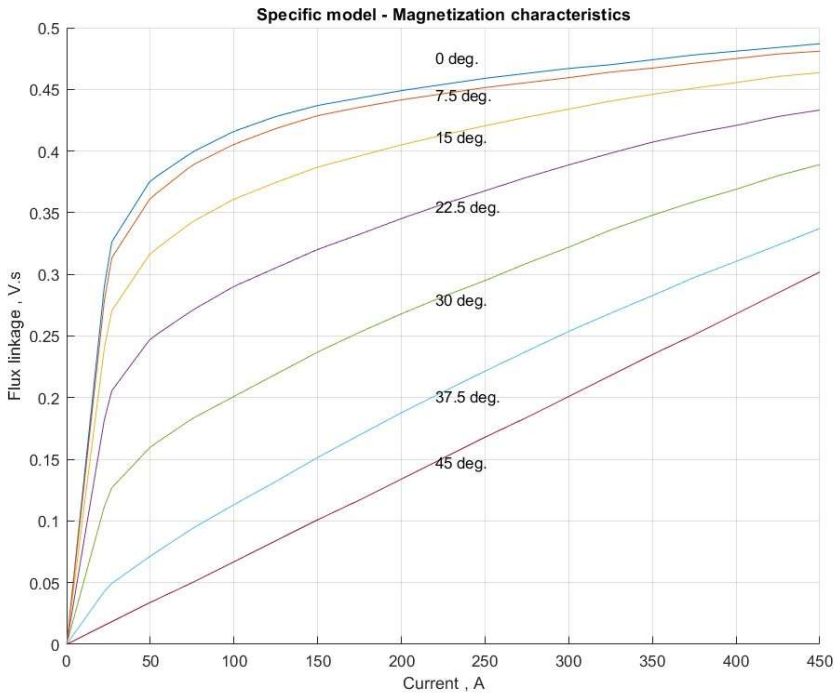

Figure 56 - Magnetization characteristics of the 6/4 SRM used in the Simulink environment.

In particular:

- Aligned position (0 deg.): The curve at 0 degrees represents the maximum inductance state, where a rotor pole is perfectly aligned with an excited stator pole. As shown in figure above, this curve exhibits a strong non-linear behaviour, flattening at higher currents due to the magnetic saturation of the stator and rotor core material.
- Unaligned position (45 deg.): For a 6/4 SRM, the maximum unaligned position occurs at 45 mechanical degrees. Here, the magnetic flux path is entirely dominated by the large air gap. Consequently, the relationship between flux linkage and current is completely linear, acting as the minimum inductance boundary.
- Intermediate positions: The transitional curves map the flux variation as the rotor moves towards alignment.

By providing these magnetization profiles, the Simulink solver computes the instantaneous co-energy, allowing for a highly realistic estimation of the electromagnetic torque generated by the motor during the switching phases

Therefore, the next figure shows all together the output of the SRM to better understand how looks all the variables in a time interval of 1 second. This time interval is enough to understand how the system starts and how is going to stabilize. This Figure 57 is followed by the detailed windows that represent the variable path in a smaller interval to better understand the values.

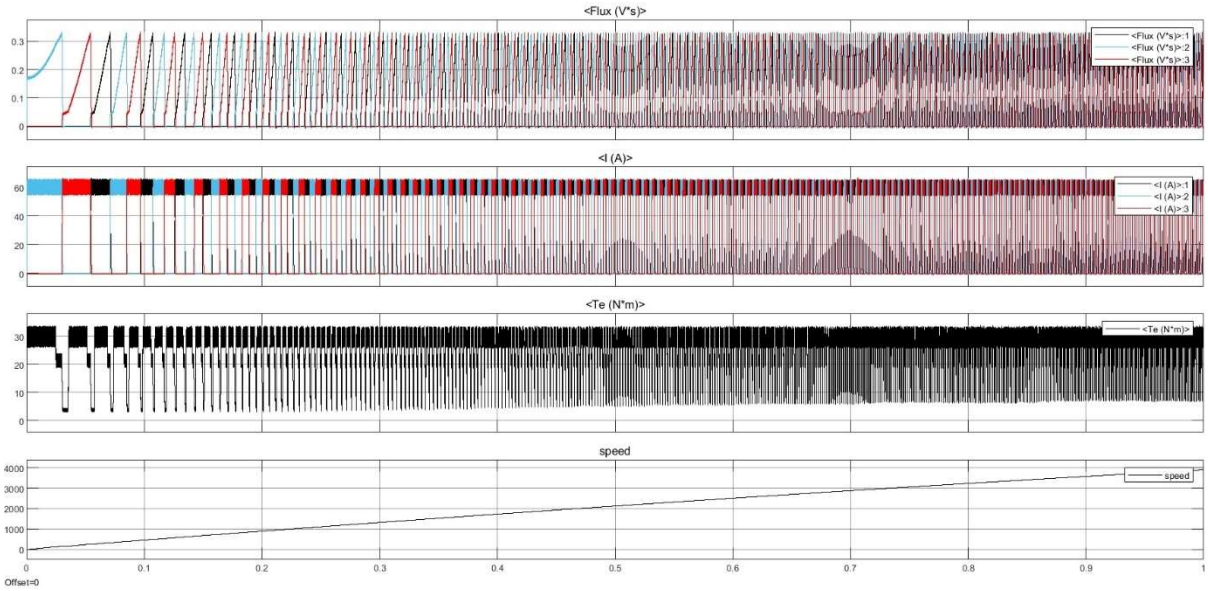

Figure 57 - SRM's outputs - base Simulink model

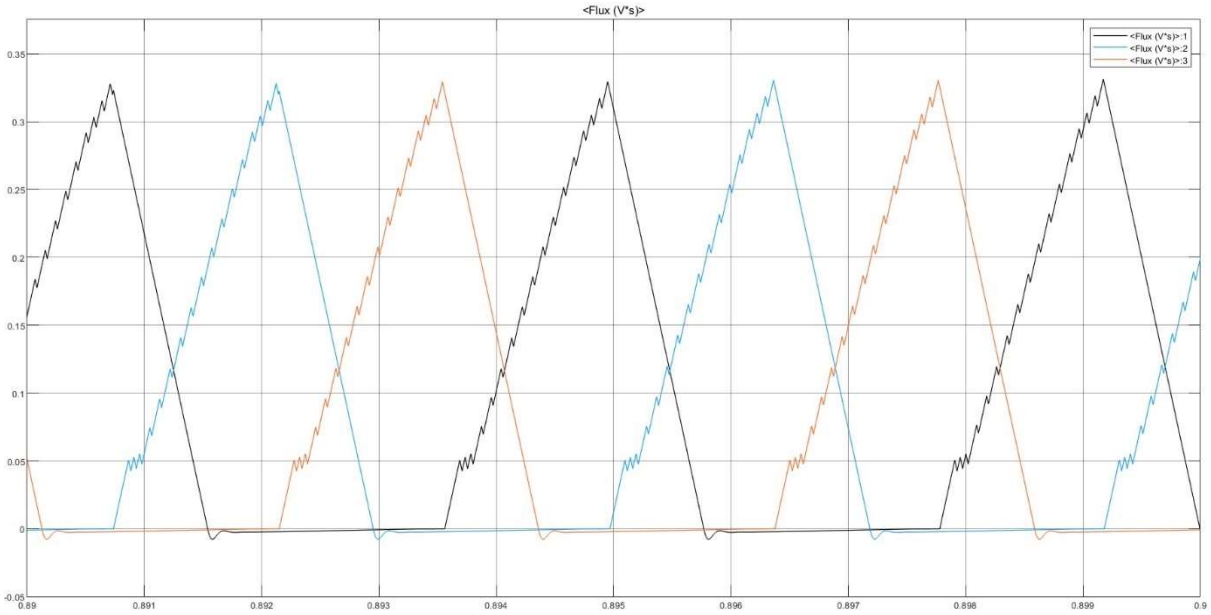

Figure 58 - Flux detail (V*s) - base Simulink model – [0.89 : 0.9]

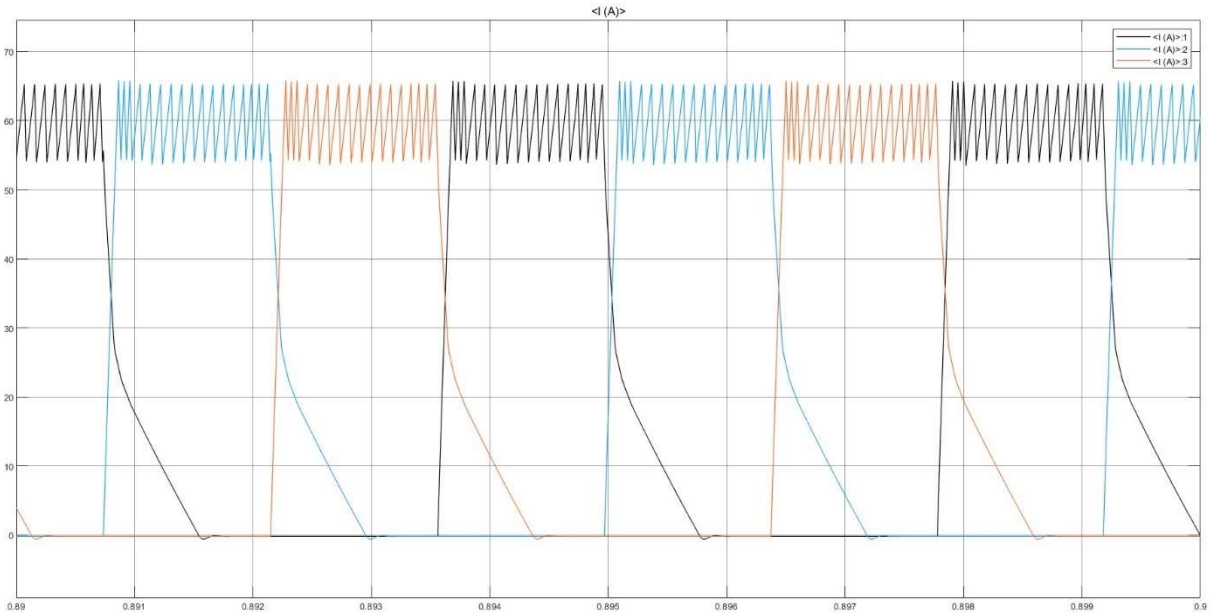

Figure 59 - Current detail (A) - base Simulink model - [0.89 : 0.9]

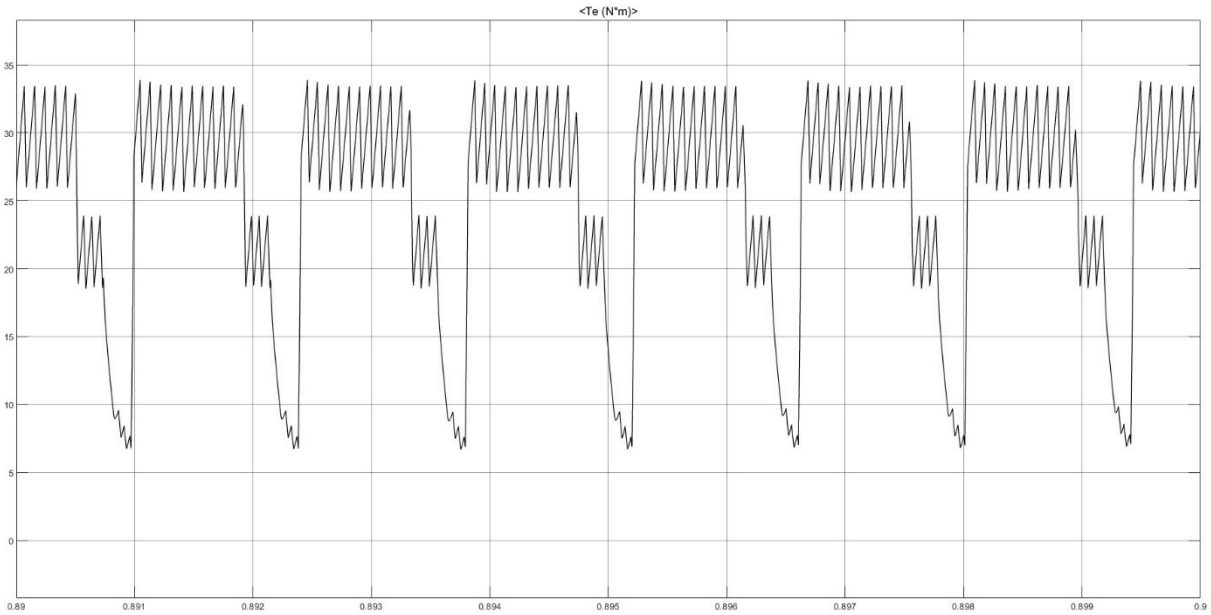

Figure 60 - Torque detail (N*m) - base Simulink model - [0.89 : 0.9]

Seeing the figure above it's evident that the motor set as base model has high torque ripple, to better understand these values, in Table 9 are reported in detail the analysis of the torque ripple. For the table drawing up the data considered are related to the second half part, so from 0.5 seconds up to 1 second, where the system is stabilized.

Table 9 - Torque values - base Simulink model

Variable	**Magnitude**
Torque max [N*m]	33.83
Torque min [N*m]	3.12
Torque average [N*m]	24.60
Torque ripple abs [N*m]	30.71
Torque ripple percentage	124.84%

Ripple percentage is calculated as follows:

$$Torque\ ripple\ [\%] = \frac{Torque\ \max - Torque\ min}{Torque\ average} * 100 \quad (5.1.\ 1)$$

5.2. Proposed model

The proposed model starts from the starting model but with some differences, it differentiates from the base model by the usage of different components and different logic. The first change is the converter, followed by different hysteresis and current logic, and by different management of the excited phases.

In particular, the converter passes from an asymmetric h-bridge to a flying capacitor inverter (explained in the previous chapter). This change permits first to menage in a different way the hysteresis, that passes from a 2-level logic to a 5-level logic, enabling 2 positive thresholds, 1 freewheeling phase and 2 negative thresholds, as reported in next Table 10.

Table 10 - Hysteresis thresholds

Threshold	**Magnitude**
High	± 5
Low	±2
Freewheeling	0

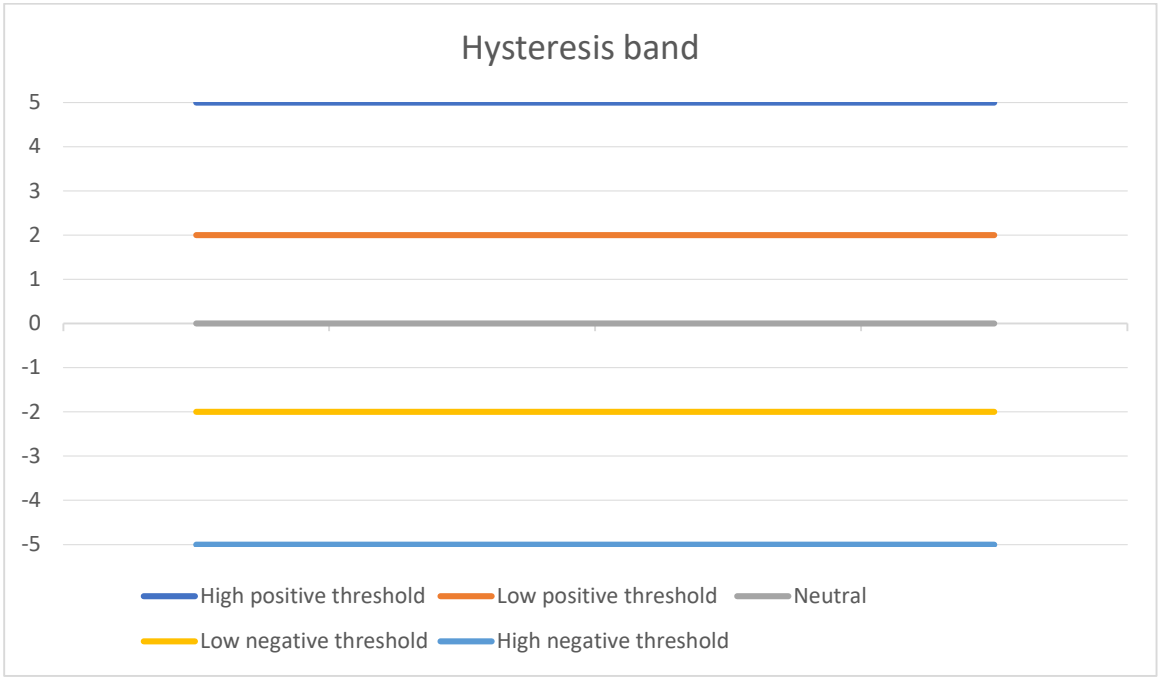

The operation follows the logic according to which the actual current value that comes out from the SRM is compared to the reference current value and their difference is considered as “error”. This error compared to the Table 10, selects the current band of respect, which involves a specific logic to the IGBT of the converter, selecting which one needs to be closed or opened.

To complete the discourse of the hysteresis logic is fundamental to deal with the converter explanation, the next Figure 61 shows one branch of the flying capacitor inverter, the branches are three, one for each phase.

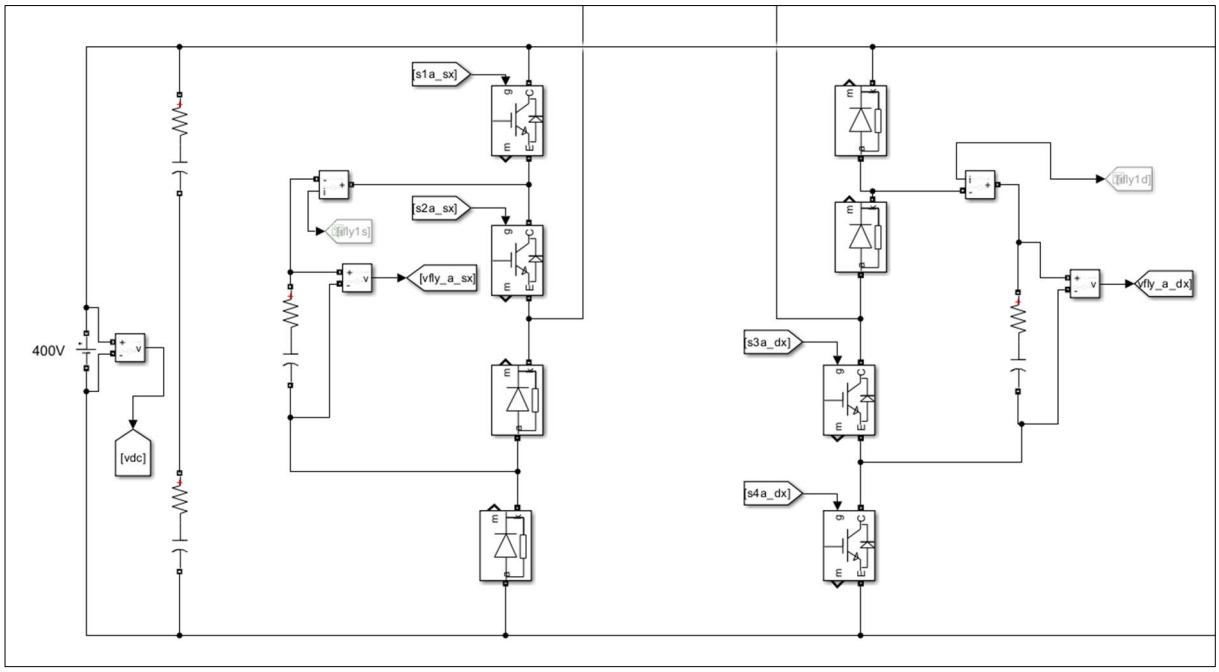

Figure 61 - Single branch of C-fly inverter - proposed Simulink model

The hysteresis logic defines 5 levels, the converter control is based on the closing and the opening of the four IGBT, according to the need for the motor. If the error is up the high threshold, this means that the engine needs the maximum power, so the converter logic provide the direct current flow from the source to the motor, without passing through the flying capacitors, instead if the error is inside the band between the high and the low error, that means that the motor doesn’t need the maximum power, so the current can pass through the capacitors due to have more modulation and have an half voltage up to the heads of engine phases. This logic is joined also with the necessity of maintaining charged the capacitor, all this logic is previously reported in Table 8.

The torque ripple considered in this study is split in two, the ripple that comes during the normal phase excitation. Taking into account the base Simulink model shows in

Figure 60, the first torque ripple to resolve is the one that goas from 26 to 34 Nm and the one, more critical, that occurs between the de-energization of the actual phase and the excitation of the next phase, so the oscillation that goes from 30 to 7 Nm.

The first torque ripple is resolved managing the hysteresis control, which thanks to the c-fly inverter provide more flexibility, due to the fact that the capacitors, once loaded, provide smooth and reduced conducting torque oscillation. To resolve the second torque ripple, the more relevant one, the system needs a more complex logic. That logic enables the combination of a specific current profile with a superposition of two phases.

The first actuation of the logic is to program the desired superposition, in this study the superposition is set to 6 degrees, the superposition happens delaying the switch-off of the current excited phase, which helps to cover the empty torque space between the alternation of phases using all the inductance remnant, so basically the system works with 2 phase excited at the same time for 6 angles degrees, when the actual phase is reaching the turn-off angle, it remains active for other 6 angle degrees, to cover the initial inductive loading of the successive excitation phase (see Figure 13, Figure 14), so the "turn-off" angle become 80.

This superposition method implicates a correct and specific modulation of the current, as reported in Table 11. In the proposed Simulink model all the three currents are handled independently in order to adapt the current respect the inductance in each phase position, in fact when the inductance decrease due to the propriety of the motor's materials, to maintain the same torque, the currents need to increase their values, or also, as happened in this study, the moment when the two phases overlapped, there is a delicate instant when the current can reach high value, due to the addition of the one phase with low inductance.

Table 11 - Current profile modulation - proposed Simulink model

Phase position (θ)	Operative zone	Current value (A)	Note
$\theta < \theta_{on}$	Off	0	The phase is not excited
$\theta_{on} \leq \theta <$ Start ramp	Start	I_{ref}	Fix reference current
Start ramp $\leq \theta < 70$	Ramp	$I_{ref} * k_{ramp}$	Linear current increase until k_{ramp}reaches 1.25
$70 \leq \theta < \theta_{off}$	Boost	$I_{ref} * 1.2 * k_{ramp}$	Linear current increase until reaches $I_{ref} * 1.25$ with a x 1.2 boost
$\theta_{off} \leq \theta < \theta_{off}$ + superposition	Ramp	$I_{ref} * k_{ramp}$	Linear current increase until reaches $I_{ref} * 1.25$
$\theta > \theta_{off}$	Off	0	The phase is not excited

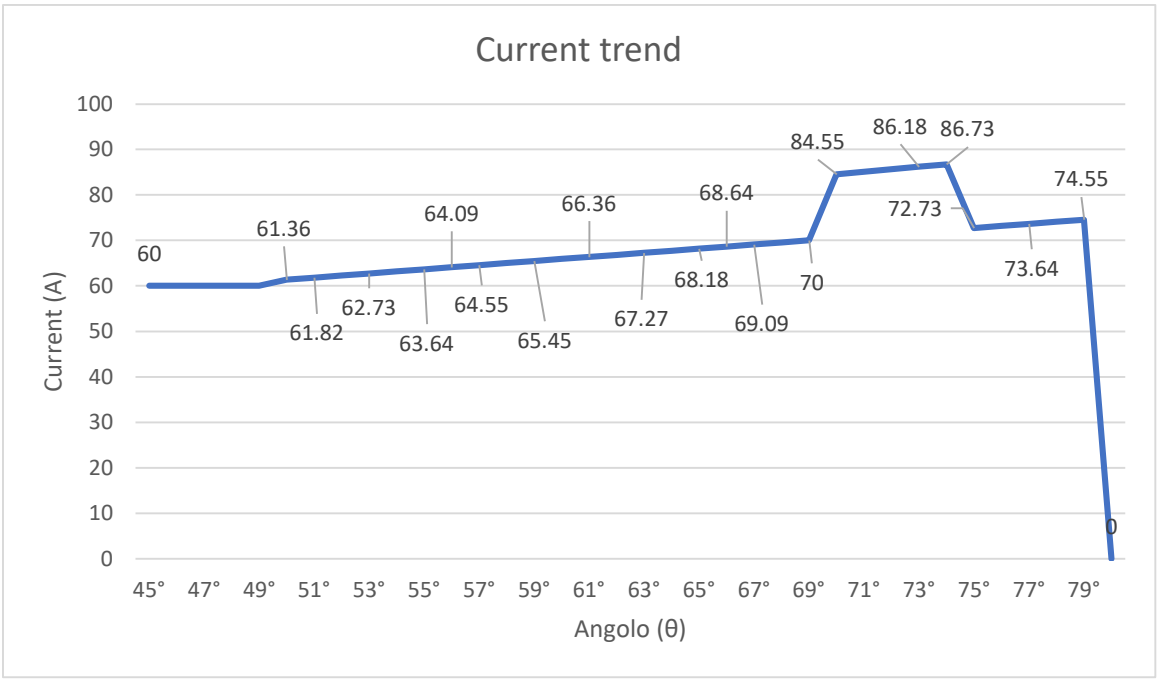

Figure 62 - Current trend referred to Table 11

The boost section unlocks when the motor reach 1000rpm, that's why before that set of velocity the current boost persists for too long destabilizing the system.

Thanks to the modulation of the current together with the superposition effect of two phases, a clear decrease in torque ripple can be highlighted, the torque ripple percentage is decreased by more than two quarter, more than 80 percent less, the torque values of proposed Simulink model are reported in the next Table 12.

Table 12 - Torque values - proposed Simulink model

Variable	**Magnitude**
Torque max [N*m]	37.16
Torque min [N*m]	24.48
Torque average [N*m]	31.69
Torque ripple abs [N*m]	12.68
Torque ripple percentage	40.01 %

To sharpen the proposed mode and take all the advantage from the FCMI, the hysteresis analysis is updated bleating the band of respect, doing this, is possible to reduce further the torque ripple, in fact, it is reduces by other 10%, as explained in the next Table 13, and showed in the next figure, obviously this hysteresis narrowing depends on the performance desired by the engine.

Table 13 - Torque values - proposed Simulink model – hysteresis logic modified

Variable	**Magnitude**
Torque max [N*m]	37.40
Torque min [N*m]	27.23
Torque average [N*m]	33.62
Torque ripple abs [N*m]	10.17
Torque ripple percentage	30.26 %

In the next Figure 63 is shown, as final configuration that provide a torque ripple percentage of 30.26%, the variable of the phases B and C, in particular it demonstrates how the modulation of the current of the respective phases is adopted to modulate the torque:

Where:

- "G" is the gate command for the normal conduction, in this case is from 45° (θ_{on}) to 74° (θ_{off}), related to its phase.
- "G s" is the gate command for the superposition conduction, in this case is from 51° to 80°, related to its phase.
- "I srm" is the output current of the switched reluctance motor, related to its phase.
- "I in" is the input current, that derive from the logic, is the modulated reference current by the logic, related to its phase.
- Theta is the position of each phase
- Torque is the output of the switched reluctance motor.

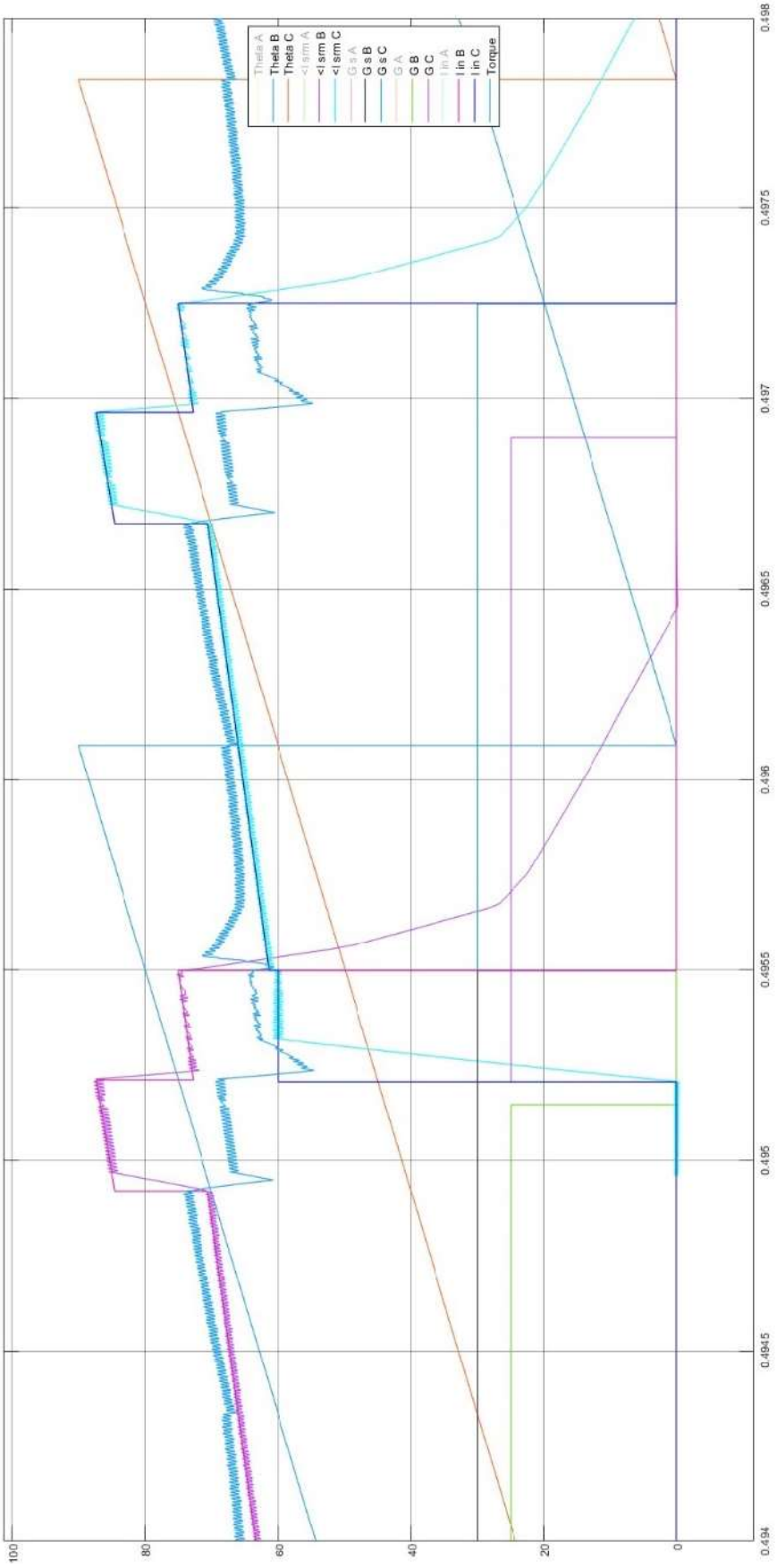
Theta A
Theta B
Theta C
<i sm A
<i sm B
<i sm C
G s A
G s B
G s C
G A
G B
G C
I in A
I in B
I in C
Torque
100
80
60
40
20
0
0.498
0.4975
0.497
0.4965
0.496
0.4955
0.495
0.4945
0.494

Figure 63 - Superposition of phase B and C variables - proposed Simulink model

The previous Figure 63 shows how the current try to compensate the decreasing of the torque during the last part of the normal conduction, between 45° and 74°. In this stretch the current is increased to maintain as much as possible the torque up, trying to keep it at the same level of conduction. The current adapt also itself when the first phase left its place to the next, because also in this case the torque would produce a low peak, indeed in this tract the current assumes a little boost.

The next figures show in detail the behaviour of flux (Figure 64), current (Figure 65) and torque (Figure 66), as output from the SRM MATLAB/Simulink block.

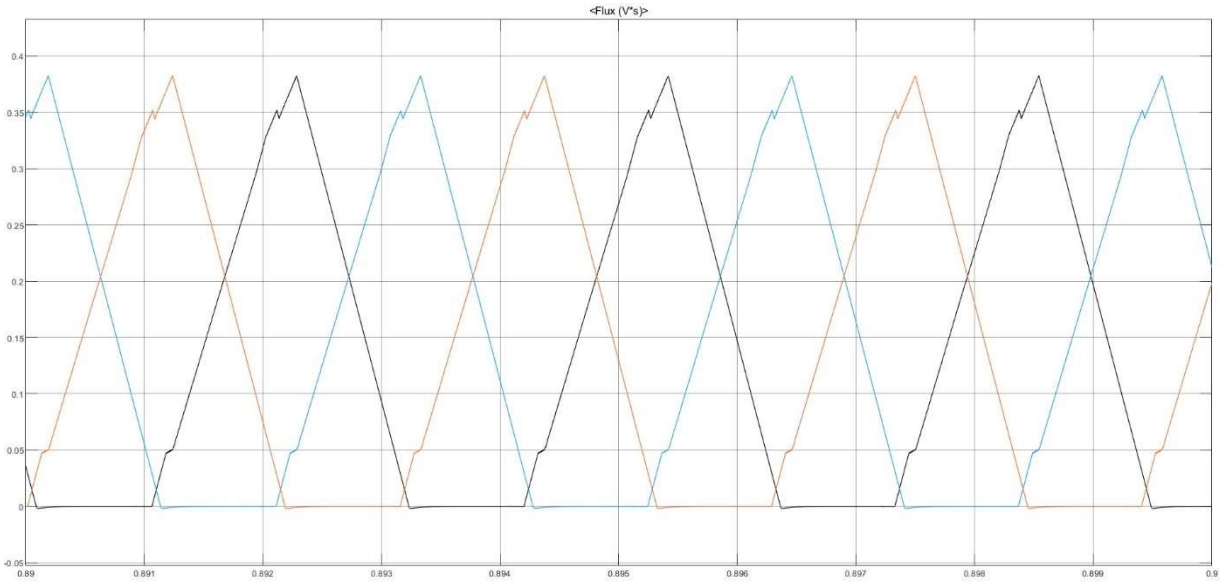

Figure 64 - Flux detail (V*s) - proposed Simulink model – [0.89 : 0.9]

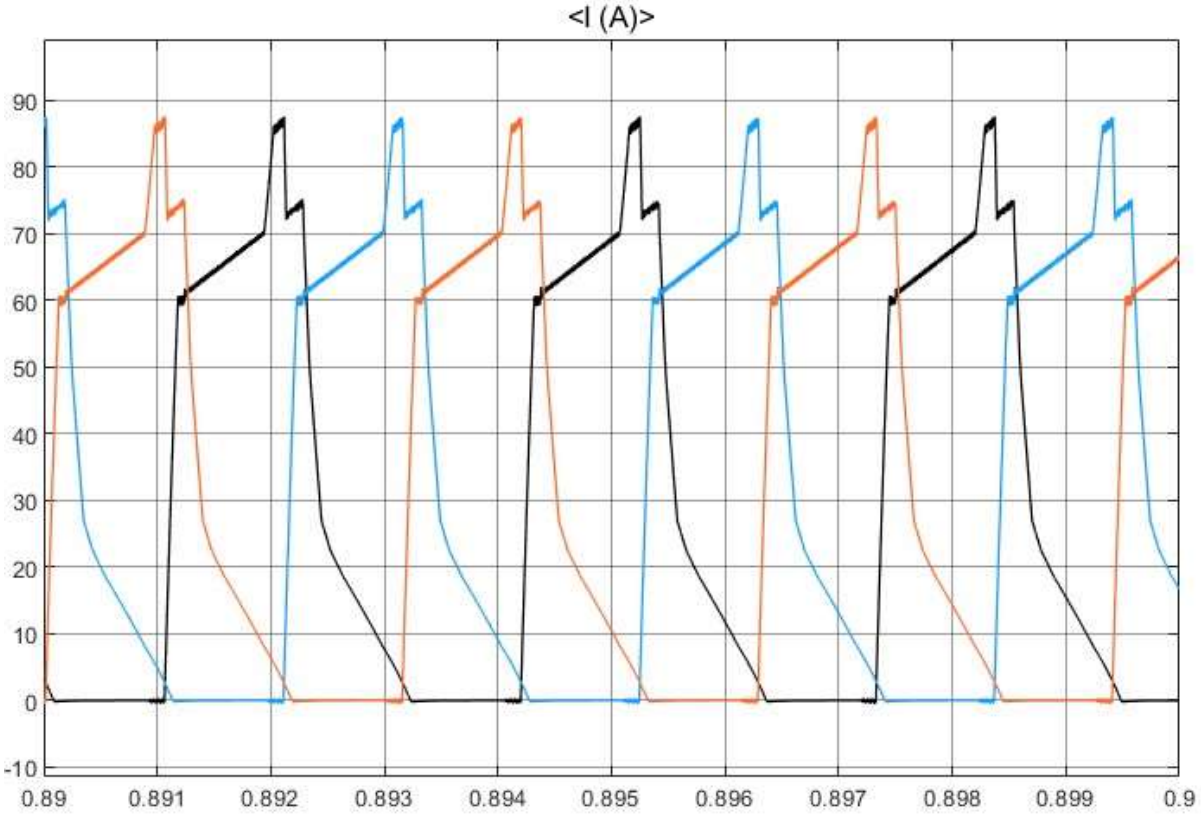

Figure 65 - Current detail (A) - proposed Simulink model - [0.89 : 0.9]

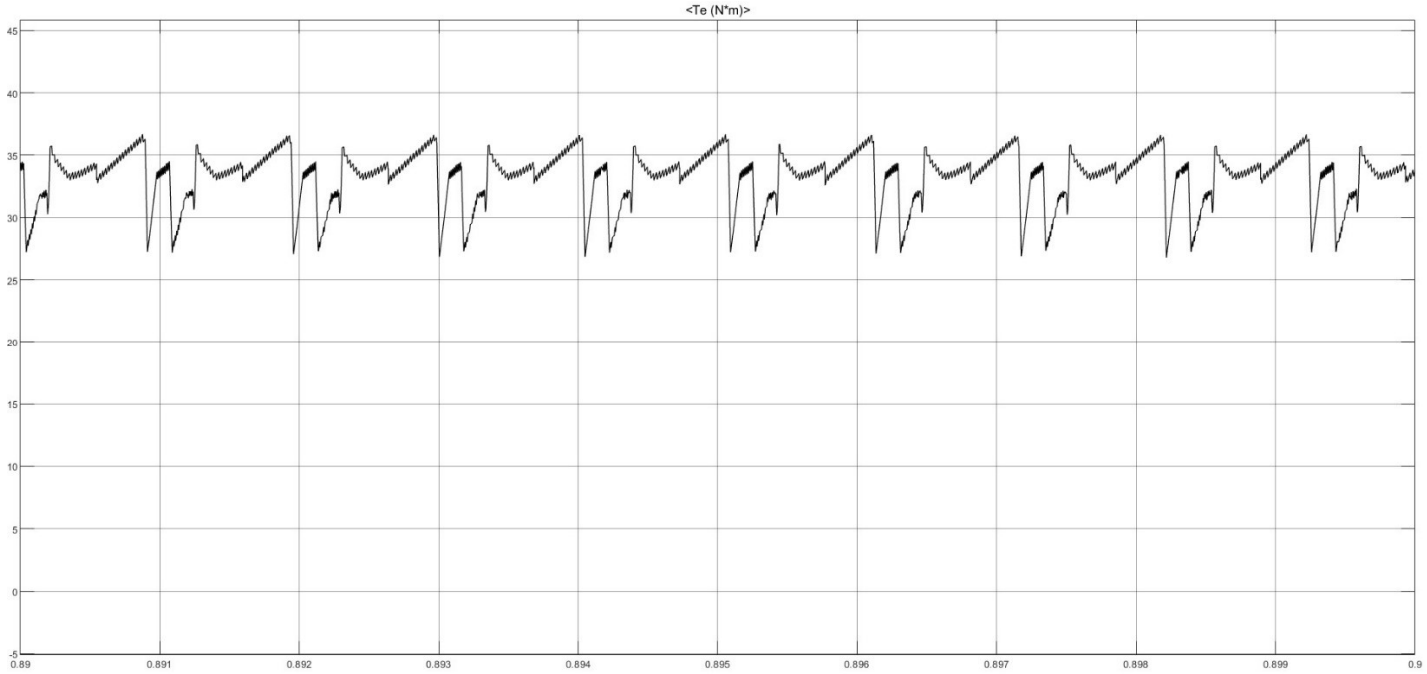

Figure 66 - Torque detail (N*m) - proposed Simulink model - [0.89 : 0.9]

5.3. Thermal analysis

Because the logic used in the proposed model, involves an overcurrent of about 135% for 6 degrees in a quarter of cycle, so in a complete rotor round it means 24° over 360°, is important to deal with the thermal behaviour of the motor.

Matlab Simulink is used to do this analysis, in this case the block used is the "Switched Reluctance Machine". Thanks to this block is possible to expose the thermal ports to model the effects of losses that convert power to heat.

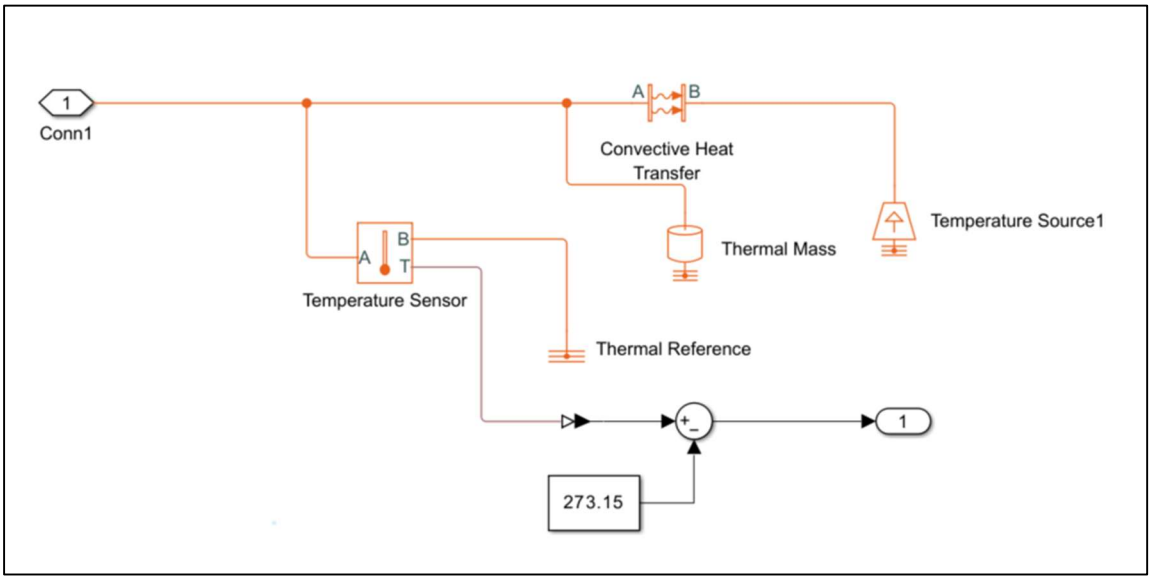

Figure 67 - Thermal system.

Where:

- Convective heat transfer between the component and the surrounding environment is modelled through a convection block, which represents heat exchange as a function of the temperature difference, heat transfer coefficient, and effective surface area.
- The thermal mass block captures the energy storage capability of the system and governs the transient temperature response based on the mass and specific heat capacity of the material.
- The temperature source is used to impose a fixed ambient temperature, acting as a thermal boundary condition for the system.

- The thermal reference defines the absolute temperature baseline required for correct operation of the thermal domain.
- The temperature sensor measures the temperature difference within the thermal network and generates a physical signal proportional to the measured temperature.
- The constant offset of 273.15 is subtracted from the measured temperature to convert the output from Kelvin to degrees Celsius, which is then provided as the final system output for analysis.

Winding resistance is assumed linearly dependent on temperature, and is given by:

$$R = R_0\big(1 + \alpha(T - T_0)\big) \tag{5.3. 1}$$

where:

- R is the resistance at temperature T.
- R_0 is the resistance at the measurement (or reference) temperature T0.
- α is the resistance temperature coefficient. A typical value for copper is 0.00393/K.

Setting the system with a proper parameters to simulate a motor with approximately the same propriety of the model cited above, adding a forced ventilation cooling system, with a default temperature of 25°C, the temperature of the three phases doesn't exceed 26.5 °C, so only 1.5°C more. This result is obtained despite the initial starting current that reach value about 300% the reference value and stabilized its value over the rest of the simulation around 80 A, so about 133% of the reference current.

6 CONCLUSION AND FUTURE DEVELOPMENTS

This thesis has explored the potential of Switched Reluctance Motors (SRMs) as a viable and sustainable alternative for electric vehicle propulsion, specifically addressing their most significant drawback: torque ripple. As highlighted throughout this work, the SRM distinguishes itself through its structural simplicity, robustness, and reliance on widely available materials. These characteristics make it an attractive candidate to replace Permanent Magnet Synchronous Motors (PMSMs), thereby reducing the automotive industry's dependency on rare-earth elements and permanent magnets.

However, the widespread adoption of SRMs has historically been obstructed by the high torque ripple intrinsic to their doubly salient structure and phase commutation. The research presented here addressed this challenge by proposing an advanced drive topology that combines a Flying Capacitor Multilevel Inverter (FCMI) with a five-level hysteresis control and a specific phase-overlapping current profile.

The simulation results obtained with MATLAB Simulink have demonstrated the effectiveness of this proposed architecture. By replacing the conventional asymmetric half-bridge converter with the flying capacitor topology, and by implementing a superposition of phases during commutation, the system achieved an important reduction in torque ripple. The ripple percentage decreased from 124.8% in the base model to 30.26% in the proposed model. Furthermore, the thermal analysis confirmed that despite the increased current demand required for phase overlapping, the motor's temperature remains within safe operational limits.

Looking at the broader context, the evolution of SRM technology is gaining momentum. While early limitations restricted its use, recent years have seen a surge in innovations ranging from design optimizations, like Multi-Stack and Multi-Layer Structure or physical modification such as rotor ribbing to reduce windage loss and non-uniform airgaps, to advanced control strategies like Direct Torque Control (DTC) and sensorless operation. These developments are progressively closing the performance gap with traditional AC motors.

In conclusion, the Switched Reluctance Motor stands as a competitive solution for the next generation of electric vehicles, offering a balance between cost, performance, and sustainability. The results of this thesis confirm that with the adoption of advanced power converters and control logic, the issue of torque ripple can be effectively managed. It remains the duty of future research to further refine these control

strategies, perhaps integrating them with sensorless techniques, to fully unlock the potential of SRMs in the mass market.

Bibliography

[1] J. -W. A. a. G. F. Lukman, "Switched reluctance motor: Research trends and overview," *CES Transactions on Electrical Machines and Systems,* vol. 2, no. 4, pp. 339-347, 2018.

[2] B. &. D. K. &. Y. Foley, "Factors Affecting Electric Vehicle Uptake: Insights from a Descriptive Analysis in Australia," *Urban Science,* 2020.

[3] M. Safari, "Battery electric vehicles: Looking behind to move forward," *Energy Policy,* vol. 115, pp. 54-65, 2018.

[4] Y. J. L. a. K. R. A. Emadi, "Power Electronics and Motor Drives in Electric, Hybrid Electric, and Plug-In Hybrid Electric Vehicles," *Transactions on Industrial Electronics,* vol. 55, no. 6, pp. 237-2245, 2008.

[5] H. H. a. K. R. J. Walters, "Comparative study of hybrid powertrain strategies," *Future Transp. Technol.,* 2001.

[6] M. a. B. M. E. H. a. D. D. Zeraoulia, "Electric Motor Drive Selection Issues for HEV Propulsion Systems: A Comparative Study," *IEEE Transactions on Vehicular Technology,* vol. 55, no. 6, pp. 1756-1764, 2006.

[7] P. P. K. P. Sreeram Krishnamoorthy, "A comprehensive review of different electric motors for electric vehicles application," *International Journal of Power Electronics and Drive Systems (IJPEDS,* vol. 15, no. 1, pp. 74-90, 2024.

[8] C. D. F. 0. -. E. P. (. D. F. [2024-25], "WEBEEP -," 2024-2025. [Online]. Available: https://webeep.polimi.it/course/view.php?id=15544. [Accessed 2025].

[9] Y. Lan, Y. Benomar, K. Deepak, A. Aksoz, M. Baghdadi, E. Bostanci and O. S. Hegazy, "Reluctance Motors and Drive Systems for Electric Vehicle Powertrains: State of the Art Analysis and Future Trends," *Energies 2021,* vol. 8, no. 2079, p. 14, 2021.

[10] O. Argiolas, E. Nazeraj, O. Hegazy, J. De Backer, A. Mohammadi and J. Van Mierlo, "Design optimization of a 12/8 Switched Reluctance Motor for electric and hybrid vehicles.In Proceedings of the 2017 12th International Conference on Ecological Vehicles and Renewable Energies," *EVER 2017,* 2017.

[11] X. D. a. B. Mecrow, "A comparison of conventional and segmental rotor 12/10 switched reluctance motors," *IEEE International Electric Machines & Drives Conference (IEMDC),* pp. 1508-1513, 2019.

[12] B. G. E. A. Payam Vahedi, "Multi-layer switched reluctance motors: Performanceprediction and torque ripple reduction," *International Transactions on Electrical Energy Systems,* 2019.

[13] A. Abdel-Aziz, M. Elgenedy and B. Williams, "Review of Switched Reluctance Motor Converters and Torque Ripple Minimisation Techniques for Electric Vehicle Applications," *Energies,* vol. 17, 2024.

[14] G. J. C. B. M. Deepak, "Power electronic converter topologies for switched reluctance motor towards torque ripple analysis," *Materials Today: Proceedings,* vol. 52, pp. 1657-1665, 2022.

[15] M. A. a. A. A. a. O. M. a. C. H. a. D. M. Gaafar, "Switched Reluctance Motor Converters for Electric Vehicles Applications: Comparative Review," *IEEE Transactions on Transportation Electrification,* vol. 9, no. 3, pp. 3526-3544, 2023.

[16] Microchip, "Microchip," 2025. [Online]. Available: https://ww1.microchip.com/downloads/aemDocuments/documents/MCU16/ProductDocuments/ProductBrief/Switched-Reluctance-Motor-Control-Solution-Product-Brief-DS70005596.pdf.

[17] A. Y. a. A. N. a. N. M. Darani, "A New Shared Flying Capacitor Multilevel Converter for SRM Drives," *2025 IEEE 34th International Symposium on Industrial Electronics (ISIE),* pp. 1-6, 2025.

[18] N. a. H. N. Yamada, "Experimental verification on a switched reluctance motor driven by asymmetric flying capacitor multilevel h-bridge inverter," *2017 IEEE 6th International Conference on Renewable Energy Research and Applications (ICRERA),* pp. 971-976, 2017.

[19] Vincotech, "Vincotech," [Online]. Available: https://www.vincotech.com/fileadmin/user_upload/content_media/documents/pdf/support-documents/technical-

papers/Vincotech_TP_Solar_The_Advantages_and_Operation_of_Flying_Capacitor_Inverter_2020.pdf.

[20] V. K. MANOJ KRISHNA SESHADRI, "Analysis of Multi-level Inverters for Electric Vehicle Application," CHALMERS UNIVERSITY OF TECHNOLOGY, Gothenburg, 2023.

[21] E. K. K. Y. M. A. Serkan Sezen, "Finite element modeling and control of a high-power SRM for hybrid electric vehicle," *elsever,* vol. 62, pp. 49-67, 2015.

[22] V. S. D. P. S. a. P. K. F. Ganesh D, "Neural Network based Direct Torque Controller of SRM for EV Application," *E3S Web Conf.,* vol. 540, no. 02003, p. 11, 2024.

List of Figures

List if Tables

Acknowledgments

First and foremost, I would like to express my deepest gratitude to my supervisor, Prof Giovanni Maria Foglia, for his invaluable guidance, continuous support, and immense knowledge. His mentorship and patience have been instrumental not only in the development of this thesis but also in my overall academic growth.

I am also deeply thankful to my university colleagues and classmates. Thank you for the countless hours spent studying together, the stimulating brainstorming sessions, and the shared struggles. You made this demanding academic journey not only possible but also truly memorable.

I must also extend my gratitude to my employer and my colleagues. Thank you for the flexibility that allowed me to balance my professional responsibilities with my academic pursuits. Navigating work deadlines alongside university exams certainly pushed my anxiety levels to new heights, but it built character. I am truly grateful for the opportunity to grow in both environments.

My most heartfelt thanks go to my parents and brother Luca, and my relatives. Thank you for your unconditional love, endless patience, and unwavering belief in me. Your continuous moral, emotional, and practical support have been my ultimate driving force throughout all these years. I could not have reached this milestone without you.

Thanks to my friends, Salvo and Barbe, thank you for always being there to listen and love me, for the much-needed moments of distraction, and for keeping me grounded during the most stressful times of this project and road ∞.

To everyone who has been a part of this journey, in ways big or small, thank you.